

論文 / 著書情報
Article / Book Information

題目(和文)	
Title(English)	A Study on the Assimilation of Swath Altimetry Data into a Global Hydrodynamic Model
著者(和文)	Menaka Revel
Author(English)	Menaka Revel
出典(和文)	学位:博士(学術), 学位授与機関:東京工業大学, 報告番号:甲第11330号, 授与年月日:2019年9月20日, 学位の種別:課程博士, 審査員:鼎 信次郎,吉村 千洋,藤井 学,福田 大輔,中村 恭志
Citation(English)	Degree:Doctor (Academic), Conferring organization: Tokyo Institute of Technology, Report number:甲第11330号, Conferred date:2019/9/20, Degree Type:Course doctor, Examiner:,,,,,
学位種別(和文)	博士論文
Type(English)	Doctoral Thesis

A Study on the Assimilation of Swath Altimetry Data into a Global Hydrodynamic Model

Nilanka Menaka Tisho Kumar Revel

**A Study on the Assimilation of Swath
Altimetry Data into a Global Hydrodynamic
Model**

Nilanka Menaka Tisho Kumar Revel

A dissertation submitted in partial completion
of the requirements for the degree of

Doctor of Philosophy

Department of Civil and Environmental Engineering
Graduate School of Environment and Society
Tokyo Institute of Technology

July 2019

Acknowledgements

First and foremost, I would like to express my deepest appreciation to my supervisor Prof. Shinjiro Kanae for accepting me and guiding me to success. I consider it is an excellent opportunity to be a student of you. Your, guidance, leadership and valuable advice helped me to improve in academic and also in personal life within the last five years.

I wish to express my gratitude to the committee members: Assoc. Prof. Chihiro Yoshimura, Assoc. Prof. Manabu Fujii, Assoc. Prof. Takashi Nakamura, and Assoc. Prof. Daisuke Fukuda. Their comments and suggestion are valuable for improving our research findings and my thesis.

My special thanks go to my co-supervisor Assoc. Prof. Dai Yamazaki for providing valuable comments and suggestions to improve my research. Furthermore, I would like to appreciate extending his valuable time for research discussion.

My sincere gratitude goes to Mr. Daiki Ikeshima, former Kanae Lab member, who helped me to develop source codes for the data assimilation programme.

I would like to extend my sincere gratitude to all the members in Kanae Lab, where I spend almost 5 years, specially Dr. Sayaka Yoshikawa, Assi. Prof. Rie Seto, Dr. Natuski Yoshida, Dr. Sachindra, Dr. Joy Sanyal, Dr. Orie Sasaki, Mr. Dim Wannet, Mr. Wongnarin Kompor, Miss. Rina Ueda, Miss Natsumi Kitajima, Mr. Kotaro Kikuchi, Miss. Sha Ou, Mr. Lorenzo Valerio Simone, Mr. Keisuke Doi, Mr. Kiyoharu Hasegawa, Mr. Kota Higashiyama, and Mr. Yosuke Akatsuka. My spical thanks goes to Mrs. Yoko Umibe, the Secretary of Kanae Lab. I would like to express my thanks to former Kanae Lab members, Dr. Megumi Watanabe, Mr. Kobayshi, Mr. Tawatari, Mrs. Orimo and others.

I would like to acknowledge the funding received from the Japanese Ministry of Education, Culture, Sports, Science, and Technology (MEXT) to conduct my doctoral research. Furthermore, I would like to thank Student Support Division Medical Centre, and the staff in the training centre of Tokyo Institute of Technology to keep my mind and body in healthy condition.

My deepest appreciation goes to all the members of Sri Lankan Student Association and Sri Lankan community in Japan for helping me to enjoy my life in Japan

with fullest potential by being as members of a single family while taking care of each other's in every challenging situation.

I want to express my gratitude from bottom of my heart to who my lovely wife Dr (MBBS). Hashini Fernando who is always beside me. My special gratitude goes for my mother, father (late) and sister for their unconditional love and affection which always keep me happy and motivated.

Finally, I would like to convey my heartfelt gratitude and appreciation for each and every citizen in Japan, who helped me to add such an unforgettable experience to my life and invaluable ethics and values to my personality.

Abstract

Water resource management has faced challenges in recent decades due to limited in situ observations and the limitations of hydrodynamic modelling. Depletion of in situ gauging stations in recent decades, especially in developing world made it difficult to assess the water cycle in global/continental-scale. On the other hand, limitations of hydrodynamic modelling such as: input runoff forcing errors, model parameter error, and simplified model physics prevent accurate estimation components of water cycle.

Recent advances in satellite technology have enabled estimation hydrodynamic characteristics from remote sensing data. The upcoming Surface Water and Ocean Topography (SWOT) mission will observe the surface waters in global/continental-scale and will provide maps of simultaneous mapping of inundation area and water surface elevation (WSE) of inland waters (i.e., river, lakes, wetlands, and reservoirs). Chapter 2 discuss the SWOT project objectives in the context of land hydrology and the characteristic of the payloads in the SWOT satellite. The 2-dimensional dynamic WSE maps by SWOT can be used to measure the storage and extent changes of terrestrial waters and also to estimate river discharge.

In chapter 3, the overall methods and model impletions were discussed. We introduced the observation system simulation experiment (OSSE) which is a methodology design to assess the potential of a new type of measurements before it is built or deployed. The Local Ensemble Transformation Kalman Filter (LETKF) which is the algorithm used to perform the data assimilation in this study is described in this chapter. In addition, Catchment-based Macro-scale Floodplain (CaMa-Flood) hydrodynamic model is being introduced which is the core of our assimilation setup. CaMa-Flood is a computationally efficient global river routing model which specially designed for large scale river modelling

Data assimilation methods were increasingly used to correct hydrodynamic model forecasts with the use of satellite altimetry data in local scale rivers (river length ≥ 1500 km). However, global scale data assimilation schemes demand for efficient filtering techniques to improve the calculation capabilities. Therefore, we developed a computationally efficient filtering technique to assimilate swath altimetry data into a global hydrodynamic model which is presented in the chapter 4. We developed a

physically based empirical local patches for hydrologic data assimilation considering the autocorrelation of the WSE using CaMa-Flood modelled WSE data from 1980-2000. Firstly, we transformed the CaMa-Flood modelled WSE into a distribution close to standard normal distribution. The transformation involves removing linear trends, removing the seasonality, and standardizing. Then we perform semi-variogram analysis to find the auto-correlation parameters (i.e. sill, range) using Gaussian semi-variogram model. Using the auto-correlation parameters, we converted the experimental semi variances into a spatial dependency weightage. We found that those spatial dependency weightages follow the hydrodynamics of the river. Then a threshold was defined (i.e. 0.6) to the spatial dependency weightage to find the area of the empirical local patch. The localization function which is used force a large error to the distance observation also derived from the fitted correlation parameters (i.e. sill, range). The developed physically based empirical localization methods were tested using LETKF based algorithm in a continental-scale river (Amazon basin). Using the physically based empirical localization, we were able to estimate the discharge well (Assimilation Index > 0.8). Furthermore, comparing empirical local patch data assimilation with other conventional fixed patch localization methods revealed that empirical local patches perform better than conventional methods in hydrologic data assimilation.

Chapter 5 investigate the potential of estimating global river discharge when the realistic input runoff forcing is not available. Here, we use the LETKF based empirical localization parameters (developed in Chapter 4) to assimilate the WSE. Three distinct runoff error scenarios namely biased, blind and different, were examined. In the biased runoff experiment the input runoff -25% bias was added. Different year's runoff was used in the blind runoff experiment. Whereas runoff data from a different Land Surface Model (LSM) was used in the different runoff experiment. The results from the three experiments suggest that the magnitude of peaks and troughs as well as peak discharge timing can be well estimated incorporating satellite observations. In addition, realistic celebration of model parameters (i.e. Manning's coefficient) is necessary to receive full advantage of the data assimilation.

The potential of estimating river bathymetry using satellites observations were examined in the Chapter 6. Here, we use LETKF algorithm via state-parameter estimation to assimilate WSE and river bathymetry simultaneously. We compare two experimental

settings for the assimilation scheme: Zero and Empirical patch-based assimilations. In the Zero patch experiment, a single pixel was used for assimilation, only when direct observation is available. In contrast, all observations inside the empirical local patch is used in the Empirical patch experiment. The root mean square error (RMSE) of global river bathymetry was reduced by 68% and 15% respectively in Zero patch and Empirical patch experiments. However, there were some large error in the mild slop reaches (Amazon downstream, Congo midstream, Mississippi downstream) when using zero local patch but those errors were reduced using empirical local patches.

The last chapter makes the conclusions and discusses the recommendations for future studies. In this study, we developed an empirical localization method for hydrologic data assimilation. We examine the potential of our data assimilation technique using synthetic SWOT observations for continental-scale river and found that empirical localization technique can estimate the discharge with large degree of accuracy and with less computational cost. Global application of the empirical localization methods proves to be efficient at estimating characteristics of river hydrodynamic. River bathymetry was estimate reasonably well using empirical local patch data assimilation. To further improve this research developing methodologies to estimating other hydraulic/hydrodynamic parameters (i.e. Manning's coefficient) will be important. In addition, developing hybrid localization methods combining conventional and empirical localization methods will beneficial for upstream river reaches.

Publication Lists

Peer Reviewed Papers

1. **Revel, M.**, D. Ikeshima, D. Yamazaki, and S. Kanae (2019), A Physically Based Empirical Localization Method for Assimilating Synthetic SWOT Observations of a Continental-Scale River: A Case Study in the Congo Basin, *Water*, 11(4), 829, doi:10.3390/w11040829.
2. **Revel, M.**, D. Yamazaki, and S. Kanae (2018a), Estimating Global River Bathymetry by Assimilating Synthetic SWOT Measurements, *J. Japan Soc. Civ. Eng. Ser. B1 (Hydraulic Eng.*, 74(4), I_307-I_312, doi:10.2208/jscejhe.74. I_307.
3. **Revel, M.**, D. Yamazaki, and S. Kanae (2018b), Model Based Observation Localization Weighting Function for Amazon Mainstream, *J. Japan Soc. Civ. Eng. Ser. B1 (Hydraulic Eng.*, 74(5), I_157-I_162.

Presentations on Conferences/Symposium

1. **Revel, M.**, Yamazaki, D., and Kanae, S. (2018, December). Assimilation of Synthetic SWOT Observations to Improve Global River Bathymetry Using Local Ensemble Transform Kalman Filter, AGU Fall Meeting, Washington D.C. (Poster presentation)

Table of Contents

Acknowledgements	iii
Abstract.....	v
Publication Lists	viii
Table of Contents	ix
List of Tables	xiii
List of Figures.....	xiv
Chapter 1 Introduction	1
1.1 General Introduction	1
1.2 Hydrologic Data Assimilation	2
1.3 Research objectives.....	4
1.4 Outline of Dissertation.....	4
Chapter 2 The Surface Water and Ocean Topography Mission and Related Data Assimilation Studies	6
2.1 Surface Water and Ocean Topography Mission	6
2.1.1 Introduction.....	6
2.1.2 Objectives of SWOT.....	8
2.1.3 Characteristics of the SWOT satellite.....	9
2.1.4 SWOT Spatiotemporal Coverage	13
2.2 Data Assimilation Studies using SWOT Observations.....	14
2.3 Conclusion	18
Chapter 3 Experimental Methods, Data Assimilation, Hydrodynamic Model, and Synthetic SWOT Observations.....	19
3.1 Introduction.....	19
3.2 Observing System Simulation Experiment.....	20
3.3 Data Assimilation Strategy	22
3.3.1 Introduction.....	22
3.3.2 Kalman filter	22
3.3.3 Local Ensemble Transform Kalman Filter (LETKF)	24

3.3.4	Stepwise computation of LETKF	26
3.3.5	Localization techniques	27
3.3.6	Number of Ensembles.....	27
3.4	Hydrodynamic model description and implementation.....	27
3.4.1	introduction.....	27
3.4.2	Channel Cross-section Parameters.....	28
3.4.3	Input runoff forcing	29
3.4.4	Manning’s coefficient	29
3.5	Synthetic SWOT observations.....	30
3.6	Evaluation methods.....	31
3.7	Conclusion	32
Chapter 4	Development of a Physically Based Empirical Localization Method for Hydrologic Data Assimilation	33
4.1	Introduction.....	33
4.2	Methodology	35
4.2.1	Data transformation	35
4.2.2	Semi-variogram analysis.....	36
4.2.3	Empirical determination of the local patch.....	37
4.2.4	Deriving observation localization weights.....	38
4.2.5	Experimental conditions for assess empirical local patch	39
4.3	Experimental Settings	42
4.3.1	Empirical local patch experiment	42
4.3.2	Conventional local patch experiments.....	42
4.4	Results.....	44
4.4.1	Validating CaMa-Flood Discharge	44
4.4.2	Empirical localization parameters.....	44
4.4.3	Empirical Local Patch Experiment	53
4.4.4	Comparison among OSSEs.....	55
4.4.5	Very large local patch assimilation.....	57

4.4.6	Assimilation efficiency	59
4.5	Conclusion	61
Chapter 5	Estimating Global River Discharge using Satellite Observations with Runoff Forcing Uncertainty	63
5.1	Introduction.....	63
5.2	Methodology.....	65
5.2.1	Framework of the virtual assimilation experiment	65
5.2.2	Hydrodynamic model description and implementation.....	67
5.2.3	Data assimilation strategy	69
5.2.4	Experimental Settings	69
5.2.5	Evaluation method	72
5.3	Results.....	74
5.3.1	Biased runoff experiment.....	74
5.3.2	Blind runoff experiment.....	80
5.3.3	Different runoff experiment.....	88
5.4	Conclusion	94
Chapter 6	Estimating Global River Bathymetry using Satellite Observations	96
6.1	Introduction.....	96
6.2	Methodology.....	98
6.2.1	Observing system simulation experiment.....	98
6.2.2	Corrupted River Bathymetry.....	100
6.2.3	Data assimilation strategy	100
6.3	Experimental settings.....	101
6.3.1	Zero patch experiment	101
6.3.2	Empirical patch experiment	102
6.3.3	Evaluation method	103
6.4	Result	103
6.4.1	Zero patch experiment	103

6.4.2	Empirical patch experiment	109
6.5	Conclusion	113
Chapter 7	Conclusions and Recommendations	116
7.1	Conclusions.....	116
7.1.1	A physically based empirical localization method	117
7.1.2	Estimating river discharge without realistic input runoff forcing..	117
7.1.3	Estimating river bathymetry in continental-scale rivers	118
7.2	Future perspectives	119
7.3	Recommendations.....	119
References	120

List of Tables

Table 2.1 : SWOT mission science requirements and goals (Rodriguez et al. 2018)	9
Table 2.2 : SWOT mission characteristics	12
Table 2.3 : Published SWOT-related studies using data assimilation (DA) to correct different variables (d means water depth, H water elevation, w width, S water surface slope, Q discharge, Z bathymetric elevation, A_i inundation area, S_z bathymetric slope, n Manning coefficient	16
Table 3.1: Description of the terms of LETKF. N is the system dimensions (river pixels inside the local patch), m is the ensemble size and p is the number of observations	25
Table 4.1 : Results of the statistical tests for normal distribution for Obidos, Amazon River	46
Table 4.2 : Mean AIC values for different semi-variogram models	48
Table 5.1: Summary of the Experimental Settings.....	70

List of Figures

Figure 2.1: Time–space diagram of continental water surface processes and SWOT observation window. Adopted from Biancamaria et al. (2016).....	8
Figure 2.2 : Conceptual view of the future SWOT mission with its principal payloads: the Ka-band radar interferometer (KaRIn, with the observed swaths shown by the yellow polygons) and a Ku-band nadir altimeter (yellow line). Adopted from Biancamaria et al. 2016.	10
Figure 2.3 : Acquisition geometry of KaRIn on SWOT. Adapted from Fjørtoft et al. 2014	11
Figure 2.4 : SWOT nominal mission timeline. Adopted from Chen et al. 2018.....	14
Figure 2.5 : Number of SWOT revisits per orbit repeat period.....	15
Figure 3.1 : General framework of the observing system simulation experiment (OSSE)	21
Figure 3.2 : Schematic diagram showing the process of data assimilation	22
Figure 3.3 : (a) Schematic illustration of the sub-grid parameters for the river channel and floodplains. (b) Unit-catchment topography. The height above the nearest river channel is shown by the background colour. (c) Floodplain elevation profile.	29
Figure 3.4 : Generation of synthetic Surface Water and Ocean Topography (SWOT) observations. (1) True surface elevation (left), (2) SWOT coverage mask (upper middle: 2), and (3) observational error modelled using a Gaussian distribution (lower middle: 3). Synthetic SWOT observations are presented in the rightmost panel	30
Figure 4.1 : Example of Semi-variogram	37
Figure 4.2 : Schematic diagram of the delineation of the empirical local patch for the target pixel indicated by a red star. (a) Spatial dependency weights and (b) local patch. River pixels inside the local patch are shown in blue, while other river pixels are shown in grey.	38
Figure 4.3: General framework of the observing system simulation experiment (OSSE)	40

Figure 4.4 : Schematic diagram of the delineation of the conventional 1×1 fixed local patch for the target pixel indicated by a red star (l, number of pixels). River pixels inside the local patch are shown in blue, while other river pixels are shown in grey.....	43
Figure 4.5 : Hydrographs for the Amazon, Congo, Mississippi, Lena, Ob, Brahmaputra, Mekong, and Yenisei. GRDC observation data is presented in black and CaMa-Flood simulated discharge is presented in blue. Nash-Sheffield coefficient is shown in upper left corner.	45
Figure 4.6: Timeseries of a) modelled WSE (blue) and trend line (green), b) trend removed WSE (grey) and seasonality curved fitted by Fourier representation (red), and c) standardized data of trend and seasonality removed WSE (black) for Obidos GRDC location of Amazon River	47
Figure 4.7 : Histogram of standardized WSE data of Obidos GRDC location of Amazon River. Red dashed line indicates the normal distribution with 0.0 mean and 1.0 standard deviation. Mean and standard deviation shows in upper	48
Figure 4.8 : Fitted semi-variogram (blue line) and Experimental semi-variogram (balck circle) of a) upstream and b) downstream of Obidos GRDC location of Amazon River. Semi-variogram was fitted using the weighted least-squares method. Sill and range are shown in the lower right corner.....	49
Figure 4.9: Variation of spatial dependency as a weighting factor (red vertical lines) along each river stem, with target pixels. The upstream area has the largest correlated length. The horizontal axis shows the distance from the target pixel, with negative values being upstream and positive downstream. A bathymetric profile is shown in black. The average water surface elevation (WSE) is indicated in blue. The average discharge is shown in indigo. Average values are calculated for 1980–2000.....	50
Figure 4.10: Local patches for target pixels (red circles) in the Amazon River (blue area), with locations. Red circles indicate the target pixels. Grey denotes major tributaries of the Congo River.	51
Figure 4.11 : Number of SWOT observations in the derived local patch (light blue). Red stars indicate days for which direct SWOT observations are available.....	52

Figure 4.12 : (a) Size of the empirical local patch for the Congo basin (as area, km²). (b) Box plot of the empirical local patch sizes (number of pixels) for large (watershed area $\geq 10^5$ km²), medium (10^5 km² > watershed area ≥ 5000 km²), and small (watershed area < 5000 km²) river pixels..... 52

Figure 4.13: Hydrograph of the Kinshasa for year 2008. True, corrupted, and assimilated discharge values are indicated by black, blue, and red lines, respectively. The thin blue and red lines show the ensembles of corrupted and assimilated discharge, respectively. The assimilation index (AI) is shown in green, and the light green line indicates the bias of corrupted discharge relative to true discharge. Green dots represent the times of synthetic SWOT observations. 54

Figure 4.14 : Annual mean AI of Amazon basin. Pixels > 100 m³/s presented for visualization purposes..... 54

Figure 4.15 : Hydrograph at Obidos for the year 2008 in the a) Empirical, b) Zero, c) Fixed-Small, and d) Fixed-Large local patch experiments. True, corrupted, and assimilated discharge values are indicated by black, blue, and red lines, respectively. The thin blue and red lines show the ensembles of corrupted and assimilated discharge, respectively. The AI is shown in green, and the light green line indicates the bias of corrupted discharge relative to true discharge. Green dots represent the times of synthetic SWOT observations. The mean AI and ensemble spread (EnSpr) of the assimilated simulation are shown in the lower-right corner of each hydrograph. 56

Figure 4.16 : Local patch for Obidos used in the a) Empirical, b) Fixed-Small, and c) Fixed-Large local patch experiments (blue). Background colour indicates the number of SWOT observations per cycle. The Amazon River network is shown in black. Red circle indicates the target pixel. 57

Figure 4.17 : Number of SWOT observations in the a) Empirical, b) Fixed-Small, and c) Fixed-Large local patches (light blue) for Obidos. Red stars indicate days for which direct SWOT observations are available..... 57

Figure 4.18 : Difference in the annual mean AI between the Empirical and a) Zero, b) Fixed-Small, and c) Fixed-Large local patch experiments. Pixels with annual mean discharge > 100 m³/s are shown for visualization purposes. 58

Figure 4.19 : a) Local patch with the number of SWOT observations (colours) and b) time series of WSE of Obidos. The Amazon River network is shown in black. Red circle indicates the target pixel.	59
Figure 4.20 : Time series of normalized root mean square error (NRMSE) of assimilated discharge in the zero (magenta), fixed-small (red), fixed-large (violet), and empirical (cyan) local patch OSSEs. Blue line indicates the NRMSE of the corrupted simulation. The fixed-small and fixed-large patches were 11×11 and 21×21 pixels, respectively. The y-axis has been stretched to enhance the visibility of low NRMSE values	60
Figure 5.1: General framework of the observing system simulation experiment (OSSE)	66
Figure 5.2: Representation of comparison of hydrograph for true (black) and corrupted (blue) for biased runoff experiment.	71
Figure 5.3 : Representation of comparison of hydrograph for true (black) and corrupted (blue) for blind runoff experiment.	72
Figure 5.4 : Representation of comparison of hydrograph for true (black) and corrupted (blue) for different runoff experiment.	73
Figure 5.5: Hydrograph of the GRDC locations a) Obidos, b) Kinshasa, c) Salekhard, and d) Stolb for year 2008 in the Amazon, Congo, Ob, and Lena Rivers, respectively for biased runoff experiment. True, corrupted, and assimilated discharge values are indicated by black, blue, and red lines, respectively. The thin blue and red lines show the ensembles of corrupted and assimilated discharge, respectively. The assimilation index (AI) is shown in green, and the light green line indicates the bias of corrupted discharge relative to true discharge. Green dots represent the times of synthetic SWOT observations. The mean AI and percent bias (pBias) of the assimilated simulation are shown in the left corner of each hydrograph.....	75
Figure 5.6: Basin average annual mean AI with the catchment area of the basin for 20 largest basins in the world for biased runoff experiment.	77
Figure 5.7 : Global annual mean AI for biased runoff experiment. Pixels $> 500 \text{ m}^3/\text{s}$ presented for visualization purposes.....	77

- Figure 5.8 : Nash-Sutcliffe (NS) coefficient for model efficiency with a) assimilated discharge, b) corrupted discharge, and c) the difference between assimilated and corrupted discharge for biased runoff experiment. Discharge values > 500 m³/s are presented for visualization purposes. 79
- Figure 5.9 : Hydrograph of the GRDC locations a) Obidos, b) Kinshasa, c) Salekhard, and d) Stolb for year 2008 in the Amazon, Congo, Ob, and Lena Rivers, respectively for blind runoff experiment. True, corrupted, and assimilated discharge values are indicated by black, blue, and red lines, respectively. The thin blue and red lines show the ensembles of corrupted and assimilated discharge, respectively. The assimilation index (AI) is shown in green, and the light green line indicates the bias of corrupted discharge relative to true discharge. Green dots represent the times of synthetic SWOT observations. The mean AI and percent bias (pBias) of the assimilated simulation are shown in the left corner of each hydrograph. 81
- Figure 5.10 : Global annual mean AI for blind runoff experiment. Pixels > 500 m³/s presented for visualization purposes. 83
- Figure 5.11: Hydrograph of the GRDC locations a) Obidos, b) Kinshasa, c) Salekhard, and d) Stolb for year 2008 in the Amazon, Congo, Ob, and Lena Rivers, respectively for blind runoff experiment without Manning’s coefficient error. True, corrupted, and assimilated discharge values are indicated by black, blue, and red lines, respectively. The thin blue and red lines show the ensembles of corrupted and assimilated discharge, respectively. The assimilation index (AI) is shown in green, and the light green line indicates the bias of corrupted discharge relative to true discharge. Green dots represent the times of synthetic SWOT observations. The mean AI and percent bias (pBias) of the assimilated simulation are shown in the left corner of each hydrograph. 85
- Figure 5.12 : Nash-Sutcliffe (NS) coefficient for model efficiency with a) assimilated discharge, b) corrupted discharge, and c) the difference between assimilated and corrupted discharge. Discharge values > 500 m³/s are presented for visualization purposes. 87
- Figure 5.13 : Hydrograph of the GRDC locations a) Obidos, b) Kinshasa, c) Salekhard, and d) Stolb for year 2008 in the Amazon, Congo, Ob, and Lena Rivers,

respectively. True, corrupted, and assimilated discharge values are indicated by black, blue, and red lines, respectively for different runoff experiment. The thin blue and red lines show the ensembles of corrupted and assimilated discharge, respectively. The assimilation index (AI) is shown in green, and the light green line indicates the bias of corrupted discharge relative to true discharge. Green dots represent the times of synthetic SWOT observations. The mean AI and percent bias (pBias) of the assimilated simulation are shown in the left corner of each hydrograph..... 89

Figure 5.14 : Global annual mean AI for different runoff experiment. Pixels > 500 m³/s presented for visualization purposes..... 91

Figure 5.15 : Nash-Sutcliffe (NS) coefficient for model efficiency with a) assimilated discharge, b) corrupted discharge, and c) the difference between assimilated and corrupted discharge. Discharge values > 500 m³/s are presented for visualization purposes..... 93

Figure 6.1: General framework of the observing system simulation experiment (OSSE) for river bathymetry assimilation..... 99

Figure 6.2 : Schematic diagram of assimilation of both WSE and river bathymetry in Zero patch experiment..... 102

Figure 6.3 : Schematic diagram of assimilation of both WSE and river bathymetry in Empirical patch experiment..... 102

Figure 6.4: Assimilated bathymetry for Zero patch experiment of main-stream of a) Ob River b) Congo River. River bathymetry of true, corrupted, and assimilated simulation are shown in black, red, and blue lines. RMSE is presented in grey dotted lines. The mean RMSE of assimilated bathymetry of the river reach is shown in the left lower corner. 104

Figure 6.5 : Hydrographs of 1-year assimilation (January to December) for Zero patch experiment a), d) upstream, b), e) mid-stream, and c), f) down-stream of Ob River (a-c)) and Congo River (d-f)). River discharges of true, corrupted, and assimilated simulation are shown in black, red, and blue lines. The AI is presented in green lines with green dots indicating the times of synthetic SWOT observations. The mean AI and percent bias (pBIAS) of the assimilated simulation are shown in the left upper corner of the hydrographs. Horizontal

axis shows months from January to December by J, F, M, A, M, J, J, A, S, O, N, D.....	105
Figure 6.6 : Global map of root mean square error (RMSE) for a) before the assimilation and b) after 1-year assimilation for Zero patch experiment.....	107
Figure 6.7 : Global map of AI of a) river discharge and b) river bathymetry for Zero patch experiment. Pixels with annual mean discharges > 500 m ³ /s are shown for visualization purposes.....	108
Figure 6.8 : Assimilated bathymetry for Empirical patch experiment of main-stream of a) Ob River b) Congo River. River bathymetry of true, corrupted, and assimilated simulation are shown in black, red, and blue lines. RMSE is presented in grey dotted lines. The mean RMSE of assimilated bathymetry of the river reach is shown in the left lower corner.	110
Figure 6.9 : Hydrographs of 1-year assimilation (January to December) for Empirical patch experiment a), d) upstream, b), e) mid-stream, and c), f) down-stream of Ob River (a-c)) and Congo River (d-f)). River discharges of true, corrupted, and assimilated simulation are shown in black, red, and blue lines. The AI is presented in green lines with green dots indicating the times of synthetic SWOT observations. The mean AI and percent bias (pBIAS) of the assimilated simulation are shown in the left upper corner of the hydrographs. Horizontal axis shows months from January to December by J, F, M, A, M, J, J, A, S, O, N, D.....	111
Figure 6.10 : Global map of root mean square error (RMSE) for a) before the assimilation and b) after 1-year assimilation for Empirical patch experiment	113
Figure 6.11 : Global map of AI of a) river discharge and b) river bathymetry for Empirical patch experiment. Pixels with annual mean discharges > 500 m ³ /s are shown for visualization purposes	114

Chapter 1

Introduction

1.1 General Introduction

In the past 20 years, flooding has been the most common natural disaster by far, accounting for 43% of all recorded events according to a joint report with the UN Office for Disaster Risk Reduction (UNISDR) by the Centre for Research on the Epidemiology of Disasters (CRED). Furthermore 2.3 billion people were affected by floods and 1.1 billion people were affected by droughts for 1995 to 2015 (The UN Office for Disaster Risk and Centre for Research on the Epidemiology of Disasters 2015). Therefore, managing available water resources is important to the society.

Continental-scale water cycle assessment is crucial to understand and quantify terrestrial water changes. Continental-scale hydrological modelling is used to derive indicators which are important to policy makers (Döll et al. 2016). Complex hydrological modelling which operate at cutting edge-technology can perform in local-scales to derive accurate forecasts. However, the validation of the results of those models is limited in continental-scale due to lack of observation data. In addition, the assembling such models to develop large scale predictions is became difficult due to the high computing efficiency,

large calculation time, and lack of resources. Therefore, assessing the water cycle in large-scale using global hydrologic models is considerably efficient.

Water resource management is connected with the assessment of components of the water cycle. Even though river discharge is a key variable for water cycle assessments (Oki and Kanae 2006), number of accessible in-situ stream gaging station are not adequate for detailed assessments. Recent advances in satellite technology makes it possible to estimate river discharge via satellite remote sensing data, complementing data measured by existing in situ gage networks (Yoon et al. 2012). However, river discharge cannot be directly measured from space, thus some of previous researchers (e.g. Alsdorf et al. 2007b; Bjerklie et al. 2005; Brakenridge et al. 2005; Kouraev et al. 2004; LeFavour and Alsdorf 2005) have used directly observable hydraulic data (such as channel width, water surface elevation (WSE), slope, and cross-sectional area) to estimate the river discharge.

The next-generation satellite altimetry mission, Surface Water and Ocean Topography (SWOT) satellite mission will be slated to launch in 2021 (Biancamaria et al. 2016). The satellite mission intent to provide simultaneous mapping of inundation area and inland WSE (i.e., river, lakes, wetlands, and reservoirs), both temporally and spatially, using a Ka-band radar interferometer (Alsdorf et al. 2007b; Durand et al. 2010). With the channel centreline and width (above 50m; Biancamaria et al. 2016) which can be extracted from the dynamic water mask from SWOT (Smith and Pavelsky 2008), can be used to measure the water storage change in terrestrial water bodies and characterize river discharge (Lee et al. 2010). Even though it is possible to indirectly estimate WSE by the spatial intersection of a water mask and a digital terrain model, those shoreline methods were not eligible to characterize WSE for complex floodplain geomorphologies, such as those of the Amazon (Alsdorf et al. 2007a).

1.2 Hydrologic Data Assimilation

Data assimilation methods can be used to extract the information which is not directly observable from the space borne measurements (Reichle 2008). Recently data assimilation techniques have been used to reduce the uncertainty of hydraulic models, in order to support the flood monitoring (e.g. Giustarini et al. 2011; Matgen et al. 2010; Neal et al. 2009) but these methods only apply for high flow conditions at local scales with

high resolution digital elevation models. Andreadis et al. (2007) concluded that the Ensemble Kalman Filter (EnKF) can reduce the discharge error by 16.9% in 50km each of the Ohio River; river bathymetry was assumed to be known. Durand et al. (2008) have used an ensemble data assimilation method for estimating bathymetric depths and slopes from WSE measurements and the LISFLOOD-FP model over a 240-km reach of the Amazon River floodplain. The methodology was able to retrieve the bathymetric depth and slope to within 56 cm and 0.30 cm/km, respectively, by exploiting the flooding extent over the Amazon River floodplain. However, their results were limited by the assumption of simplified bathymetry; spatial variations in bathymetry at scales finer than 50 km were not modelled. In Biancamaria et al. (2011), virtual observations of the SWOT observations were assimilated using a Local Ensemble Kalman Smoother (LEnKS) of the Ob River. Yoon et al. (2012) had presented a methodology which has a potential of estimating the bed elevation and water depths from SWOT observations using the Local Ensemble Batch Smoother (LEnBS) assimilation framework for the Ohio River. In this study the bathymetry showed a 0.52 m reach-average root mean square error (RMSE), which is improved by 67.8% and the instantaneous river discharge estimate over the experimental period had a 10.5% normalized RMSE, which is improved by 71.2%; they only considered two critical uncertainties: precipitation forcing that propagates to boundary inflows and river bathymetry errors. Pedinotti et al. (2014) proposed Extend Kalman Filter (EKF) based assimilation scheme to assimilate the Manning coefficient in Niger River basin. The method leads to a global reduction of 40 % of the Manning coefficient error over the river and error of the water levels has been reduced by 30 %; the finite difference scheme which is used to relate the Manning coefficient to WSE may not be consistent with the physical mechanism. Ikeshima et al. (2017) proposed the first global framework for correcting the discharge from corrupted runoffs using a Local Ensemble Transform Kalman Filter (LETKF; Hunt et al. 2007) which is computationally effective for global scale studies. They suggested that river hydrodynamic characteristics (such as annual mean flow or flood peak timing) can be reasonably estimated by assimilating simulated SWOT measurements even when realistic forcing data are not available. However, they disregard the uncertainties in hydrodynamic model and topography parameters (e.g., elevation and channel bathymetry).

1.3 Research objectives

The main purpose of this study is to use simulated SWOT observations to improve the model predictions of a global hydrodynamic model. In order to fulfil the main objective, we derive several sub-objectives listed as follows:

1. Develop a computationally efficient hydrologic data assimilation technique which can be utilize in the global/continental-scale
2. Estimate the actual discharge when there is uncertainty in the input forcing to the hydrodynamic model in global/continental-scale.
3. Estimate the correct model parameters (i.e. river bathymetry) using data assimilation techniques

1.4 Outline of Dissertation

Chapter 2 presents a detailed description of Surface Water and Ocean Topography (SWOT) mission which is saluted to be launched in 2020. SWOT mission objectives and orbit characteristic are introduced in respect to terrestrial hydrology. In addition, there are description about the previous studies related to SWOT data assimilation and discuss the knowledge gap in them.

Chapter 3 introduces the detailed descriptions of methodologies used in this study and the implication of the global hydrodynamic model, Catchment-based Macro-scale Floodplain (CaMa-Flood: Yamazaki et al. 2011). Here we introduce the observing system simulation experiments (OSSE), which is a methodology designed to assess the potential of a new type of measurements before it is built or deployed. A description about Local Ensemble Transformation Kalman Filter which is computational efficient version of Ensemble Kalman Filter, is presented. Furthermore, the method for generating synthetic SWOT observations is discussed.

In Chapter 4 we explain the development of the physically based empirical localization parameters for hydrologic data assimilation which was derived considering the auto-correlation of simulated water surface elevation spatially. We test the developed localization method using a -25% biased runoff experiment in the Amazon Basin.

Chapter 5 is dedicated to extensive testing of different scenarios of runoff errors and estimating river discharge. Here we test three different scenarios namely; biased,

blind and different runoff experiments. We use the computationally efficient data assimilation techniques developed in the chapter 4, the physically based empirical localization to perform the experiments.

A description of global river bathymetry assimilation is presented in the Chapter 6. Here we assimilated river bathymetry using single pixel assimilation and empirical local patch assimilation (developed in chapter 4)

Chapter 7 summarizes entire research and present the conclusions. It also introduces some future directions to this research.

Chapter 2

The Surface Water and Ocean

Topography Mission and Related Data

Assimilation Studies

2.1 Surface Water and Ocean Topography Mission

2.1.1 Introduction

Access to fresh water is a basic need of the society. Observing temporal and spatial variations in water stored in rivers, lakes, reservoirs, floodplains, and wetlands are the most important in that context. In the past few decades, the necessity of the data on spatiotemporal dynamics of surface water became more critical with decreasing in situ gauging network and increasing demand in observations and modelling of global water cycle (Alsdorf et al. 2003). Alsdorf (2003) propose a method to develop a “topographic imager” satellite mission with capacity to observe main channels, floodplains and lakes, ability to sample flood waves and river dynamic at basin scale, and capability to measure height changes that characterize variations in river discharge and lake water storage.

Spatial and temporal dynamics of surface water is poorly known due to the heterogeneity of in situ gauges (United States of America/Europe is well observed while Asia/Africa poorly observed), unavailability of in situ observation data in international level, and inadequate satellite observations to observe global spatiotemporal dynamics of continental water surface (Alsdorf et al. 2007b).

In order to improve the observability of the surface water (Alsdorf et al. 2007b) proposed a new satellite mission based on synthetic aperture radar (SAR) interferometry, called Water and Terrestrial Elevation Recovery (WATER). The concept of WATER is built on the legacy of Shuttle Radar Topography Mission (SRTM) and the Wide Swath Ocean Altimeter (WSOA). SRTM employed two synthetic aperture radar interferometers namely C- and X-bands on the NASA Space Shuttle Endeavour (Farr et al. 2007). SRTM provided digital elevation model (DEM) at 90 m spatial resolution between 60°S and 60°N. But it provided poor measurements of surface water between 30° and 60° because of its oblique look angles. Construction of an SRTM-like system on a satellite platform would be inconvenient because the two interferometric antennas were separated by a 60 m mast (Biancamaria et al. 2016). A similar concept to WSOA, Jason-2 satellite mission was launched as an additional payload to the altimetry with the aim of measuring ocean topography. The distance between the two Ku-band antennas was set to 6.4 m to facilitate inclusion on a satellite platform (resulting in kilometeric pixel resolution), and a near-nadir look angle was chosen to better observe the ocean surface (Fu et al. 2012). WSOA was definitely withdrawn in 2004 and never flown. To adapt this concept to the needs of continental water surface observation, Alsdorf et al. (2007) proposed to use Ka-band instead of Ku-band, allowing better spatial resolution. In 2007, the National Research Council recommended to NASA this new satellite mission, under the name Surface Water and Ocean Topography (SWOT), to measure both the ocean and land water surface topography. SWOT has been collaboratively developed by NASA, the Centre National d'Etudes Spatiales (CNES, the French space agency), the Canadian Space Agency (CSA/ASC) and the United Kingdom Space Agency (UKSA). Currently, SWOT is planned for launch in late 2020. It will observe the whole continental waters, estuaries, and ocean continuum.

2.1.2 Objectives of SWOT

Figure 2.1 shows the SWOT observation window with respect to the main spatiotemporal physical processes related to the land hydrology. SWOT is intending to observe a large fraction of rivers and lakes globally and will provide robust observations of their seasonal cycles. However, it will not assess climate variability (and especially climate change) and will not be able to monitor flash floods (temporal scale below 24 hrs).

The primary hydrologic objective of the SWOT mission is to characterize the spatial and temporal variations in surface waters globally. According to Rodriguez 2018, the following hydrologic science questions will be addressed by the SWOT mission:

1. What are the temporal and spatial scales of the hydrologic processes controlling surface water storage and transport across the world's continents?
2. What are the spatially distributed impacts of humans on surface water, for example through water impoundment behind dams, withdrawals and releases to rivers and lakes, transboundary water sharing agreements, diversions, levees, and other structures?
3. What are the regional- to global-scale sensitivities of surface water storages and transport to climate, antecedent floodplain conditions, land cover, extreme droughts, and the cryosphere?
4. Can regional and global extents of floodable land be quantified through combining remotely sensed river surface heights, widths, slopes, and inundation edge with coordinated flood

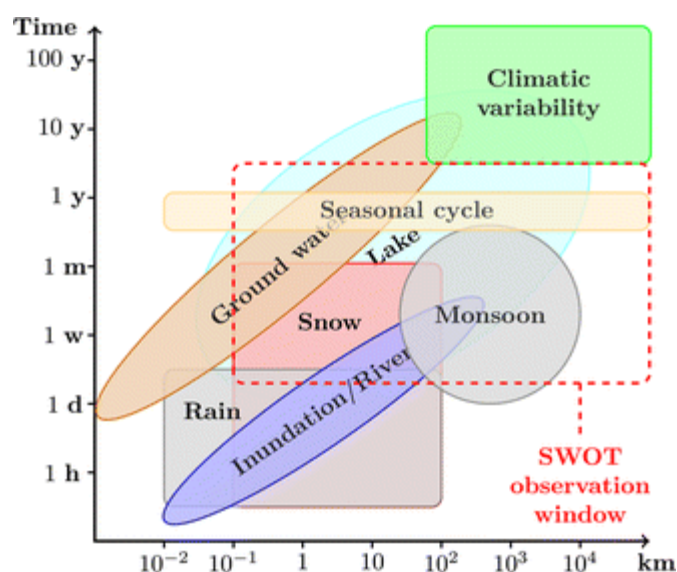


Figure 2.1: Time–space diagram of continental water surface processes and SWOT observation window. Adopted from Biancamaria et al. (2016)

modelling?

5. What are the hydraulic geometries and three-dimensional spatial structures of rivers globally, knowledge of which will improve our understanding of water flow?

In order to answer above scientific question regarding land hydrology the SWOT Science Requirements, have been derived to design the SWOT mission (summed up in Table 2.1 according to Rodriguez 2018).

2.1.3 Characteristics of the SWOT satellite

Table 2.2 presents the characteristics of SWOT satellite which are designed to meet the SWOT science requirements (as in Table 2.1). A Ka-band radar interferometer (KaRIn) has been designed as the mission main payload. KaRIn will be a SAR interferometer in Ka-band (35.75 GHz frequency / 8.6 mm wavelength), with near-nadir incidence angles between 0.6° and 3.9° (Fjørtoft et al. 2014). Figure 2 shows a conceptual view of the KaRIn operating system and ground coverage. It will provide images of water elevations within two swaths, one on each side of the satellite. These two swaths (each 50 km wide) will be separated by a 20 km gap at the satellite nadir (Figure 2.2). KaRIn will operate in bistatic mode: one antenna emits the electromagnetic signal toward the closest swath and the two antennas (10 m apart) receive the backscattered signal in their respective directions. Interferometry effectively involves a triangulation: each point in the swath will be observed from two different positions (the antennas positions), which will

Table 2.1 : SWOT mission science requirements and goals (Rodriguez et al. 2018)

Observed areas	water bodies $> (250 \text{ m})^2$ (goal: $(100 \text{ m})^2$) river reaches $> 100 \text{ m}$ (goal: 50 m) (width) \times 10 km (long)
Height accuracy	$< 10 \text{ cm}$ when averaging over water area $> 1 \text{ km}^2$ $< 25 \text{ cm}$ when averaging over $(250 \text{ m})^2 < \text{water area} < 1 \text{ km}^2$
Slope accuracy	1.7 cm/km for river reaches when averaging over water area $> 1 \text{ km}^2$
Relative errors on water areas	$< 15 \%$ for evaluated water body and river reaches $< 25 \%$ of total characterized water body and river reaches
Mission lifetime	3 months of fast sampling calibration orbit 3 years of nominal orbit
Rain/layover/frozen water flag	68 % or more of the contaminated data should be correctly flagged
Data collection	$> 90 \%$ of all ocean/continents within the orbit during 90 % of operational time

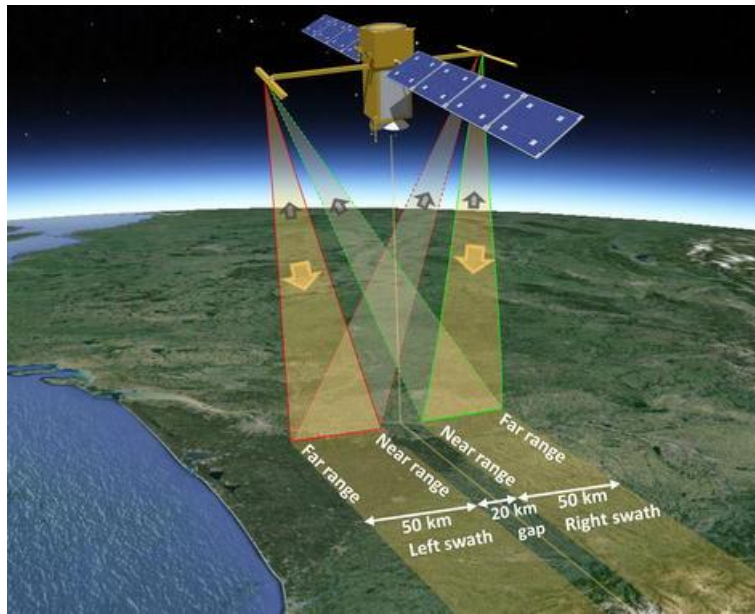


Figure 2.2 : Conceptual view of the future SWOT mission with its principal payloads: the Ka-band radar interferometer (KaRIn, with the observed swaths shown by the yellow polygons) and a Ku-band nadir altimeter (yellow line). Adopted from Biancamaria et al. 2016.

allow precise estimation of the location of each point. More precisely, the phase difference between the backscattered signals received by the two antennas (which called interferogram) will be used to invert water elevations. Table 2.2 summarizes the main characteristics of the KaRIn instrument.

KaRIn will provide images of water surface elevation with pixel sizes ~ 6 m in the azimuth direction (direction of the satellite orbit) and from 60 m to 10 m in the range direction (perpendicular to the azimuth), as indicated in Figure 2.3 (Fu et al. 2012; Fjørtoft et al. 2014; Biancamaria et al. 2010). However, these images are obtained in “radar projection” and not in a geolocated projection. Indeed, the radar instrument measures the distance between the observed point and the antenna. Therefore, in radar images, two consecutive pixels in the range direction corresponds to points on the ground that have a similar distance from the satellite. For that reason, when pixels are geolocated, they are more scattered, they do not correspond to a regular grid, and their shape becomes distorted. For example, a hill, which is a few kilometres away from a river, could have a distance to the satellite similar to that of the centre of the river and therefore could be located close to the river centre in a SAR image. However, in this example, the river banks will have a different distance from the satellite and could be several pixels distant from the river

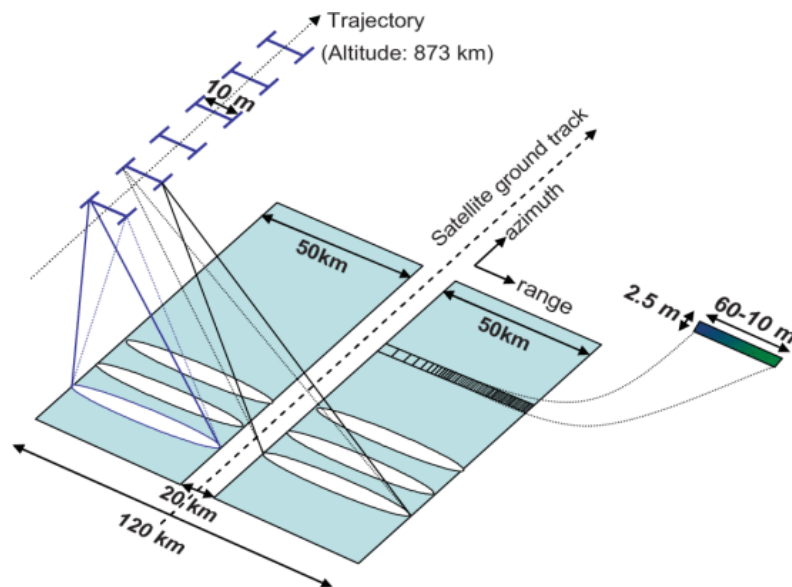


Figure 2.3 : Acquisition geometry of KaRIn on SWOT. Adapted from Fjørtoft et al. 2014

centre pixel. Therefore, the top of the hill will be closer to the river centre than the river banks. This effect, hereafter referred to as “layover,” occurs when surrounding topography or vegetation is at the same distance from the satellite as the water surface (land over water layover). Furthermore, pixels with large vertical errors will also have high geolocation error (vertical and horizontal accuracies are functions of the phase interferogram accuracy). For that reason, the most basic geolocated SWOT products will likely be delivered as point cloud products that can more accurately consider these geolocation inversion effects (Rodriguez et al. 2018). Even though KaRIn instrument measure water surface in 10 m to 60 m \times 6 m intrinsic pixel the end product of SWOT will averaging over many such pixels.

Very few satellite missions have used Ka-band, which is therefore not as well understood as lower frequency bands. For example, most current nadir altimeters use Ku- or C-bands, whereas SAR imaging missions are in L-, C- or X-bands. Additionally, these current sensors have lower (nadir altimeters) or higher (SAR imagery missions) observation incidence angles than SWOT. However, using Ka-band instead of higher wavelength bands has several advantages: first, it allows a finer spatial resolution (which is dependent on the electromagnetic wavelength) from the SAR processing and, second, it facilitates a shorter baseline (distance between the two antennas) for a given targeted instrumental vertical accuracy, for the interferometry processing (a shorter baseline corresponds to a shorter mast between the two antennas, which is easier to construct). Shorter wavelengths

also result in less penetration into soil, snow and vegetation (Fjørtoft et al. 2014), which should allow better estimation of wetland and saturated soil surface elevation and snow volume variations, if interferograms can be computed.

A drawback of Ka-band is its sensitivity to rain rates above about 3 mm/h (Rodriguez et al. 2018). The only altimetry satellite mission in Ka-band preceding SWOT is the Satellite with Argos and ALtiKa (SARAL) mission with the AltiKa nadir altimeter, launched in February 2013. Measurements obtained from this new instrument will help

Table 2.2 : SWOT mission characteristics

Orbit	
Altitude	890.5 km
Inclination	77.6°
Repeat period	20.86 days
KaRIn (core payload)	
One swath extent	50 km
Distance between swaths outer edges	120 km
Distance between swaths inner edges	20 km
Radar frequency	35.75GHz
Wave length	8.6 mm
Distance between the two antennas	10 m
Instrument azimuth pixel size	6–7 m
Instrument range pixel size	From 60 m (0.6°) to 10 m (3.9°)
Additional science payload	
Nadir altimeter	Similar to the dual-frequency (Ku/C) Poseidon-3 nadir altimeter on Jason-2
Precise orbit determination system	Laser retroreflector DORIS receiver GPS receiver
Radiometer (usable only over oceans)	Three-frequency (18, 23 and 34 GHz) radiometer, similar to advanced microwave radiometer on Jason-2

to better understand backscattering in Ka-band over different surfaces (water, bare soil, vegetation, snow, etc.). Furthermore, airborne and field campaigns have been organized by the Jet Propulsion Laboratory (JPL) (Moller and Esteban-Fernandez 2014) and CNES (Fjørtoft et al. 2014) to better understand Ka-band backscattering at SWOT-like incidence angles. These campaigns have confirmed the decrease in the backscatter coefficient with the incidence angle and a water/land backscatter coefficient contrast of around 10 dB, except when the water surface is very flat (low wind speed and hence extremely low surface roughness).

In addition to KaRIn, SWOT will carry additional scientific payload (Table 2.2), including a dual-frequency (Ku- and C-bands) nadir altimeter, similar to the Poseidon-3 instrument on-board Jason-2 (Desjonquères et al. 2010). It will provide water elevation measurements in the middle of the 20km gap between the two KaRIn swaths. A radiometer will also facilitate, over the oceans, corrections to path delay due to wet tropospheric effects. However, it will not be used over land because land emissivity dominates the radiometric signal (Fu et al. 2012). Wet troposphere corrections over land will be computed using an atmospheric model, one effect of which will be that the residual tropospheric error will likely be larger over land than over the ocean and should be on the order of 4 cm (Fu et al. 2012).

2.1.4 SWOT Spatiotemporal Coverage

SWOT mission is planned to observe the earth 3 months and 3 years (Figure 2.4 presents the nominal timeline for SWOT mission :adopted from Chen et al. 2018). First 3 months will be an initial calibration phase for the SWOT mission with a fast sampling orbit (1-day repeat period), but reduced spatial coverage relative to the subsequent orbit. The objective of fast sampling phase is to observe specific ocean/land hydrology targets and calibrate radar system parameters. In first 85 days, checkout and commissioning will be done, where the first rough set of instrument calibration parameters will be derived. The calibration phase is will be 90 days, where the calibration parameters are refined and validation over selected sites. 3 months of calibration is expected to be sufficient to obtain a fully calibrated system for the nominal phase (Rodriguez et al. 2018). Primary validation activities to continue approximately 1.5 years after launch, with low-level extended-validation activities occurring for the remainder of the mission. The nominal phase of the

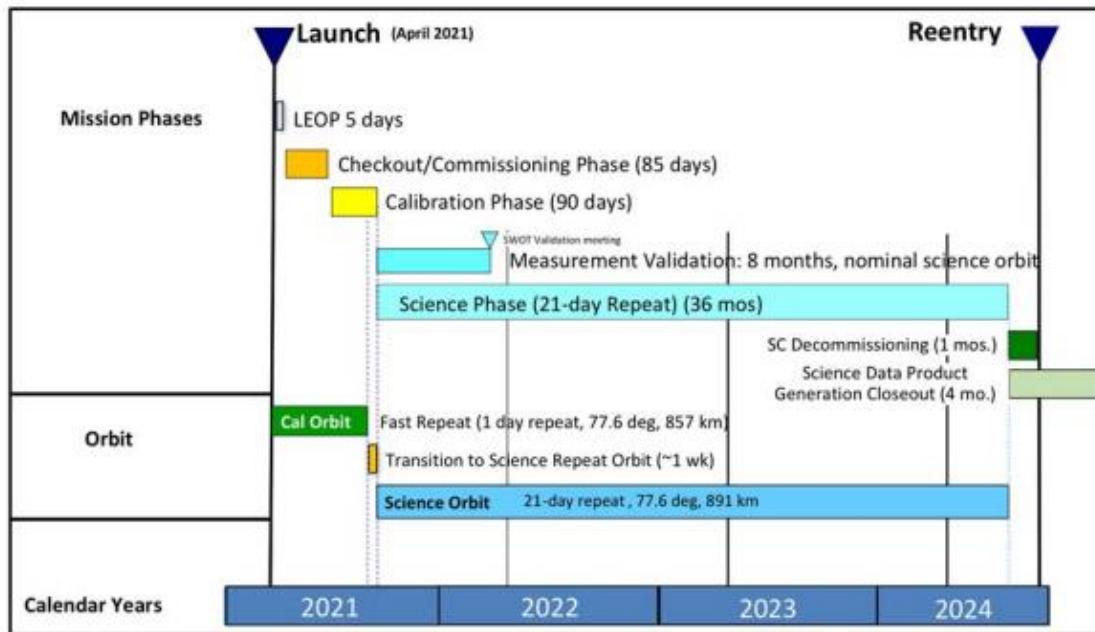


Figure 2.4 : SWOT nominal mission timeline. Adopted from Chen et al. 2018

mission (also termed as “science phase”) will have a non-Sun synchronous, 890.5 km altitude, 20.86-day repeat period and 77.6° inclination orbit (Table 2.2) and will last at least 3 years. The remainder of this section is applicable only to this nominal orbit.

SWOT spatial coverage depend on orbit characteristics, instrument swath width (2×50 km), nadir gap width (20 km) and a function of latitude. Figure 2.5 shows a map of number of SWOT revisits per orbit repeat period (~ 21 days) over the continents between 78°S and 78°N . Tropical regions will be observed less frequently than higher latitudes; the number of observations per repeat cycle ranges from maximum of two at the equator to more than ten above 70°N/S . But 3.55% of the whole land area (which is in tropical locations) may not be never be observed by SWOT which is due to the 20-km nadir gap between the two swaths and the orbit intertrack distance (Biancamaria et al. 2016).

2.2 Data Assimilation Studies using SWOT Observations

A strategy for estimation of discharge and other water surface variables can be done using statistical methods. Data assimilation (DA) methods were used to, correct hydraulic/hydrologic model parameters or state vectors using SWOT data to (Andreadis et al. 2007; Durand et al. 2008; Biancamaria et al. 2011; Yoon et al. 2012; Andreadis and

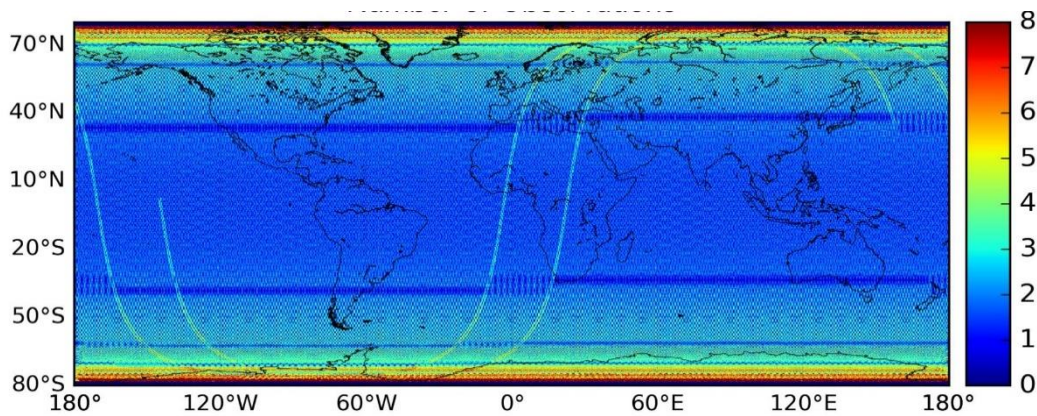


Figure 2.5 : Number of SWOT revisits per orbit repeat period

Schumann 2014; Pedinotti et al. 2014). Table 2.3 summarizes all these studies. All of the six studies summarized were designed in the context of observing system simulation experiments (OSSE), a methodology designed to assess the potential of a new type of measurements before it is built or deployed.

Andreadis et al. (2007), performed a set of identical twin data assimilation experiments with synthetically generated observations in 50km reach of the Ohio River ingested into a LISFLOOD-FP model simulation, using an EnKF. They found that: (1) The EnKF was able to successfully recover water depth and discharge from a corrupted LISFLOOD-FP simulation by assimilating synthetic satellite observations. (2) Filter simulations showed little sensitivity to assumed observation errors (0 and 25 cm standard deviation) with RMSEs being 22.4 and 26.9 cm (water depth), and 82.1 and 98.7 m³/s (discharge) respectively. (3) System performance degraded substantially as the assimilation frequency became longer. The proposed 8-day satellite overpass, gave the best overall results relative to 16-day and 32-day observation frequencies (10.0% versus 12.1% and 16.9% discharge relative error).

Biancamaria et al. (2011) used synthetic SWOT measurements to correct river hydrodynamics model forecasts Ob (1120km reach) River. They showed that the assimilation scheme at the nominal orbit of the mission reduced the spatial and temporal RMSE of the water depth by 59% and 66%, respectively. These studies either neglected bathymetry error, or treated bathymetry in a simplified way, which does not represent realistic spatial variations of bathymetry.

Table 2.3 : Published SWOT-related studies using data assimilation (DA) to correct different variables (d means water depth, H water elevation, w width, S water surface slope, Q discharge, Z bathymetric elevation, A_i inundation area, S_z bathymetric slope, n Manning coefficient)

Reference	DA schemes	Model(s) + error	SWOT obs used + error	Corrected var./Param.	Study domain
Andreadis et al. (2007)	EnKF	Hydrodynamic model + inflows errors	d (140km swath, 8-day/16-d/32-d orbit) + white noise	d	Ohio River (50km reach)
Durand et al. (2008)	EnKF	Hydrodynamic model + S_z and n errors	H (140km swath, 16-day orbit) + white noise	Z, S_z	Amazon River (240km reach)
Biancamaria et al. (2011)	LEnKS	Hydrodynamic model + precip errors	d (140km swath, 22-day orbit) + white noise	d	Ob River (1120km)
Yoon et al. (2012)	LEnBS	Hydrodynamic model + precip errors/ z	H, S, w (140km swath, 22-day orbit) + white noise	Z, d	Ohio basin river system
Andreadis and Schumann (2014)	LETKF	Hydrodynamic model + sampling historical	H, w, A_i (multi-sat missions) + white noise	Initial condition to forecast model	Ohio River (500km reach)
Pedinotti et al. (2014)	EKF	Hydrologic model ($0.5^\circ \times 0.5^\circ$ pixels) + n	d (140km swath, 22-d orbit) + white noise	n	Whole Niger basin

EnKF: ensemble Kalman filter, LEnKS: local ensemble Kalman smoother, LEnBS: local ensemble batch smoother, LETKF: local ensemble transform Kalman filter, EKF extended Kalman filter

Andreadis and Schumann (2014) proposed a methodology to correct initial conditions to improve flood forecasting using a hydrodynamic model, by using satellite water elevation and water area (from nadir altimetry, LiDAR, SAR imagery and SWOT) in 500km of the Ohio River. They showed that water elevation and flood extent forecasts with lead times up to ten days can be improved using satellite observations. However, for some flood events, model errors exceeded errors due to initial conditions after a few days, and the benefits of the assimilation dissipated.

Some studies have demonstrated the capability of correcting hydraulic/hydrologic model parameters using synthetic SWOT observations. Durand et al. (2008) have used an ensemble data assimilation method for estimating bathymetric depths and slopes from WSE measurements and the LISFLOOD-FP model over a 240km reach of the Amazon River floodplain. The methodology was able to retrieve the bathymetric depth and slope to within 56 cm and 0.30 cm/km, respectively, by exploiting the flooding extent over the Amazon River floodplain.

Yoon et al. (2012) had presented a methodology which has a potential of estimating the bed elevation and water depths from SWOT observations using the LEnBS assimilation framework for the Ohio River. In this study the bathymetry showed a 0.52 m reach-average root mean square error (RMSE), which is improved by 67.8% and the instantaneous river discharge estimate over the experimental period had a 10.5% normalized RMSE, which is improved by 71.2%; they only considered two critical uncertainties: precipitation forcing that propagates to boundary inflows and river bathymetry errors.

Pedinotti et al. (2014) proposed Extend Kalman Filter (EKF) based assimilation scheme to assimilate the Manning coefficient in Niger River basin. The method leads to a global reduction of 40 % of the Manning coefficient error over the river and error of the water levels has been reduced by 30 %; the finite difference scheme which is used to relate the Manning coefficient into WSE may not be consistent with the physical mechanism.

Those studies demonstrated the potential for using SWOT observations to improve river hydrodynamic simulations and estimate river discharge continuously in space and time. However, the above studies focused only on a local-scale (river length \leq 1500 km) rivers/part of a large river and/or used high cost data assimilation algorithms in

their respective studies, which made extension to global scale difficult. Also, a global hydrodynamic model which has the potential to describe the water surface elevation with a reasonable rate is needed to incorporate with SWOT observed WSE. In addition, global scale assimilation is awaiting because where and how SWOT observations are beneficial is not known.

2.3 Conclusion

In this chapter, we introduced the characteristics of upcoming SWOT mission and presented some SWOT related DA studies. SWOT will provide fundamental information about rivers, lakes and wetlands in continental scale and can be used to understand land hydrology (Biancamaria et al. 2016). Maps of surface water elevation and their temporal evolution will provide by the SWOT mission which can be used for estimating surface water storage and fluxes at global-scale for rivers. SWOT will allow us to can gain knowledge on understanding transboundary river basins; data about river discharge, reservoir storage, and reservoir releases.

Previous studied suggests that the data assimilation techniques are not yet mature enough for global-scale studies (Biancamaria et al. 2016). Therefore it needed to develop efficient data assimilation techniques to be performed in global scale (such as LETKF based techniques: Ikeshima et al. 2017). With the advancement of global scale hydrodynamic models which have capacity to apply in continental and/or global scale (Yamazaki et al. 2011).

Chapter 3

Experimental Methods, Data

Assimilation, Hydrodynamic Model, and

Synthetic SWOT Observations

3.1 Introduction

In this chapter we intend to provide information about our overall experimental methodology which is observing system simulation experiment (OSSE), data assimilation strategy, description about the hydrodynamic modelling involved in this study, and generating synthetic SWOT observations.

OSSE is type of experiment used for assess the importance of a planned measurement system before it is deployed. We use this method of experiments in our study to examine the potential our novel approaches towards the SWOT data assimilation. The OSSE is widely used method to test such systems across several disciplines (e.g. Miyoshi and Yamane 2007; Andreadis et al. 2007).

A variation on Ensemble Kalman Filter (EnKF: Evensen 1994), named as Local Ensemble Transformation Kalman Filter (LETKF: Hunt et al. 2007). LETKF is a computationally efficient method for data assimilation in global scale. The LETKF technique is rather a simple and allows for flow-dependent background-error covariances. Large scale data assimilation which demands for efficient and simple filtering technique can be well served by using LETKF.

Catchment-based Macro-scale Floodplain (CaMa-Flood: (Yamazaki et al. 2011) global river model is purposefully developed for global applications. CaMa-Flood presents good opportunity to model global rivers in considerably low computational cost rather than 2-dimensional hydrodynamic models whose extended from regional-scale to global-scale.

3.2 Observing System Simulation Experiment

Observing system simulation experiments (OSSE) is the main experimental methodology in our study which is designed to assess the potential of a new type of measurements before it is built or deployed. We used an OSSE (Andreadis et al. 2007; Yoon et al. 2012) to assess the potential of assimilation at the continental scale. The OSSE consisted of three separate simulations: ‘true simulation’, ‘corrupted simulation’, and ‘assimilated simulation’ (Ikeshima et al. 2017) as in Figure 3.1. The CaMa-Flood hydrodynamic model (Yamazaki et al. 2011) was used to generate the true, corrupted, and assimilated simulation estimates for the data assimilation framework in this study.

To create synthetic SWOT observations, we performed the true simulation to generate the true virtual water state, which was continuous in space and time. In the true simulation, the river hydrodynamic model was forced by true (assumed to be true) input runoff forcing (or non-corrupted runoff) and true (best preformed) model parameters, and the true water state (river discharge, WSE, and water storage) was generated. Then, synthetic SWOT observations were generated by applying a SWOT coverage mask delineated from orbit data (CNES 2015) to the true WSEs, followed by the addition of noise. Therefore, we assumed that only a portion of the true water state (i.e., WSEs in the SWOT observation area, with some observation errors) was known when data assimilation was performed.

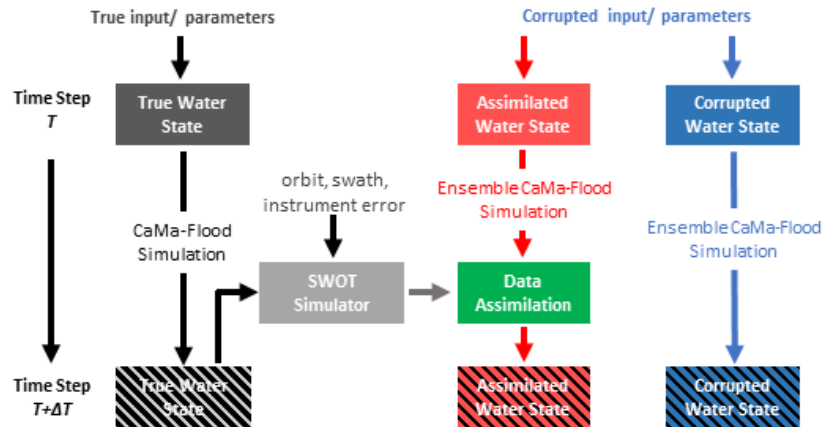


Figure 3.1 : General framework of the observing system simulation experiment (OSSE)

A ‘corrupted simulation’ was performed to compare the corrupted state of the model with the assimilated and true simulations. The corrupted simulation used in this study was executed with corrupted model settings (i.e., corrupted input runoff forcing, corrupted Manning’s coefficient) representing both forcing and parameter/formulation errors. All other parameters (i.e., river channel depth, river width, elevation) in the corrupted simulation were identical to those in the true simulation. Furthermore, noise was added to the corrupted settings (runoff and Manning’s coefficient) to generate the ensemble states required for the assimilation procedure. A data assimilation procedure was not implemented in the corrupted simulation.

We executed the ‘assimilated simulation’ to test the potential for using SWOT observations to estimate discharge. We used the same model settings as for the corrupted simulation, but with assimilation of synthetic SWOT observations. At the end of each day, the synthetic SWOT observations were assimilated into the water state forecast, and the initial conditions of the simulation for the following day were updated to reflect the assimilated water state

3.3 Data Assimilation Strategy

3.3.1 Introduction

Information from the observations can be incorporated to the model forecast and can correct the initial condition for the next time step and the model parameters. Both the information from satellite and the model has an uncertainty. Data Assimilation is useful method to get the best estimate from a model and observations. In this study, our focus is to obtain an accurate estimation with the available information. Considering the model errors and the observation errors with a Bayesian approach as shown in the schematic diagram (see Figure 3.2). As in eq 3.1 Bayesian methods provide the probability to occur some event when there is some knowledge about it.

$$p(x|y_0) = \frac{p(y_0|x)p(x)}{p(y_0)} \quad \text{eq 3.1}$$

where $p(x)$ is the probability density function (PDF) of model state before the observation is known (prior) and $p(y_0)$ is the PDF of the observations and $p(x/y_0)$ is the probability density function of model state if the observation occurs (Likelihood).

3.3.2 Kalman filter

A Kalman filter (KF) is one of the classical data assimilation method among various assimilation schemes which is designed for linear forecasting models. However, it is problematic to be used in a nonlinear forecasting models such as hydrodynamic because the error covariance of the nonlinear models cannot be estimated beforehand

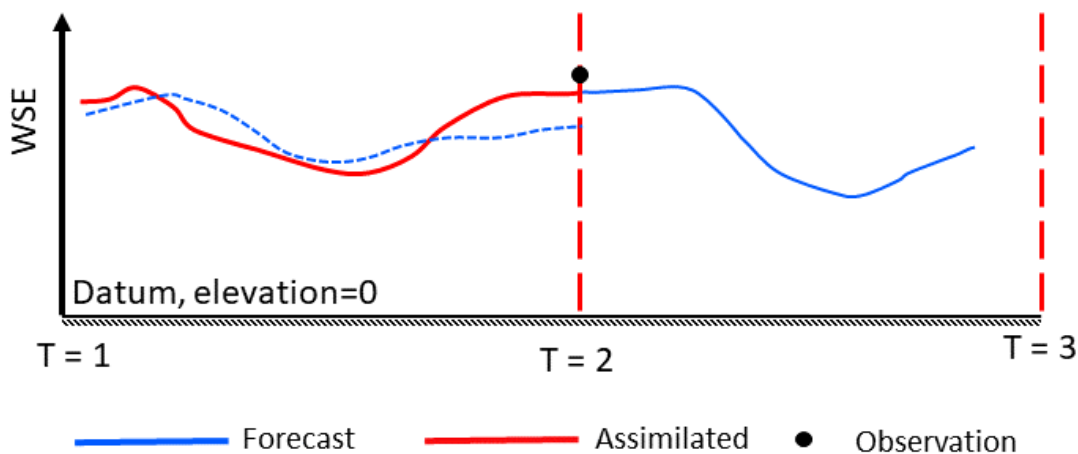


Figure 3.2 : Schematic diagram showing the process of data assimilation

unlikely in linear models on the other hand computational cost is significantly high due to the calculation of the time evolution of the error covariance (Tippett et al. 2003).

A stochastic approach is to use in case of nonlinear models have been proposed namely as Ensemble Kalman Filter (EnKF: Evensen 1994) by using ensembles to forecast error covariance and model estimate error covariance. This EnKF was successfully applied to a perfect model experiment using a low-resolution atmosphere model by Houtekamer et al. (1998). However stochastic approach requires to add and perturbation to observation to update ensemble members who can add a bias to the estimate of analysis error covariance (Whitaker and Hamill 2002).

On the other hand, perturbed observations are not necessary for creating the ensembles when using Deterministic methods, such as the Ensemble Square Root Filter (EnSRF: Tippett et al. (2003). To increase the efficiency Bishop et al. (2002) introduced a deterministic method, Ensemble Transform Kalman Filter (ETKF) which finds a transformation matrix which makes covariance calculation more efficient. Below we provide a basic explanation to the Ensemble Kalman Filter (EnKF) method used in this study Following the notation in Whitaker and Hamill (2002), the EnKF update equations are

$$x^a = x^b + K(y^o - H\bar{x}^b), \quad \text{eq 3.2}$$

$$P^a = (I - KH)P^b, \quad \text{eq 3.3}$$

where x^a is the posterior state estimator (or assimilator); x^b is the prior state estimator (or forecast); y^o is the observation vector; H is the observation operator, which is linearly related to the observation and the state; m is the number of ensembles; P^b is background error covariance matrix; P^a is analysis error covariance matrix;

$$K = P^b H^T (H P^b H^T + R)^{-1} \quad \text{eq 3.4}$$

where K is the Kalman gain matrix; R is the observation error covariance, determined from the uncertainty of the measurements

3.3.3 Local Ensemble Transform Kalman Filter (LETKF)

A data assimilation scheme is typically used to estimate time-varying model state variables, e.g., hydraulic model states such as discharge or water depth. In this study, we utilized LETKF (Hunt et al. 2007; Miyoshi et al. 2007), which is a variation of the Ensemble Kalman Filter (EnKF) (Evensen 2009), an advanced Kalman Filter (KF) (Kalman 1960), to assimilate WSE from SWOT observations. The computational cost of using an EnKF at the global scale can be reduced with LETKF, which enables global-scale data assimilation.

The LETKF algorithm is preferred in this study because its computational efficiency, and ability to use flow dependent covariance (adaptive localization parameters according to hydrodynamics of river). As LETKF does not require any background error covariance model, which one the major simplification form other numerous filtering methods. LETKF algorithm is fast primarily because it operates in low-dimensional ensemble space. Complementing the low-dimensionality LETKF can be computed mutually independent of each grid point which enables parallelization. In addition, as LETKF can treat each grid point separately, adaptive local patches and localization weights can be used easily.

Our implementation of the data assimilation strategy involves: (1) propagation of the model state variables through time with the CaMa-Flood model, and (2) updating the state variables based on SWOT observations using LETKF. The LETKF analysis equation for the update step is:

$$X^a = X^f + E^f \left[VD^{-1}V^T(HE^f)^T(R/w)^{-1}(Y^o - HX^f) + \sqrt{(m-1)}VD^{-1/2}V^T \right], \quad \text{eq 3.5}$$

where X^a is the posterior state estimator (or assimilator); X^f is the prior state estimator (or forecast); Y^o is the observation vector (here, WSE); H is the observation operator, which is linearly related to the observation and the state; m is the number of ensembles; E^f is the prior state error covariance, which is obtained directly from the ensembles; R is the observation error covariance, determined from the uncertainty of the measurements; w is the weighting term for the observation localization (Miyoshi et al. 2007); and VDV^T is given by:

$$VDV^T = (m - 1)I + (HE^f)^T R^{-1} HE^f, \quad \text{eq 3.6}$$

where I is the unit matrix with dimension m which is the number of ensembles. $VD^{-1}V^T$ and $VD^{-1/2}V^T$ can be calculated from the eigenvalue decomposition of VDV^T .

Table 3.1 gives a detailed description of the terms in the LETKF algorithm. X^a (posterior state estimator) is a matrix of N number of rows and m number of columns which is the end result of data assimilation algorithm. This posterior state estimator contains the all variables assimilated within the considered domain/system (here after local patch) in rows direction and its ensembles in the column direction. Similarly, for X^f the rows contain the prior state estimates (model forecasts) of the local patch and its ensembles in the columns. The observation vector is denoted by Y^o , which contains all the observation available inside the local patch. It is column vector with dimension p

Table 3.1: Description of the terms of LETKF. N is the system dimensions (river pixels inside the local patch), m is the ensemble size and p is the number of observations

Term	Explanation	Dimension	Description
X^a	posterior state estimator	$N \times m$	a matrix containing ensembles of assimilated states for the system
X^f	prior state estimator	$N \times m$	a matrix containing ensembles of model forecasted states for the system
Y^o	observation vector	$p \times 1$	vector containing the available observations in the system
H	observation operator	$p \times N$	a matrix used operate N-dimensional ensemble mean state vector to return p-dimensional observation vector
E^f	prior state error covariance	$N \times m$	a matrix containing perturbations (deviation from mean) of the prior state estimator
R	observation error covariance	$p \times p$	a matrix containing the observation error covariance (can be affected by observation localization)

(number of observations inside the local patch) H is the observation operator with the dimensions $p \times N$ which is used to convert the ensemble mean prior states to observational space. H consist 1 if the observation is available and 0 if no observation, in the row direction. Row direction corresponds to number of pixels in the local patch, column direction corresponds to number of observations in observation operator. R is the observation error covariance which is a diagonal matrix if the observations are uncorrelated.

3.3.4 Stepwise computation of LETKF

In this section, the step wise analysis of LETKF is being presented which used in this study;

1. Select the target pixel (the pixel which need to do the assimilation)
2. Obtain pixel locations of the local patch (only river pixels are considered)
3. The ensembles of prior state variables are stacked to X^f where columns direction is for pixels in the local patch and ensembles are stacked in row direction.
4. Then the observations available inside the local patch is found.
5. Create H , the observation operator considering the available observations inside the local patch. H will have either 1 or 0 depending on the availability of the observation. One row of H represents one observation. That row will have 1 in the respective places where there are observations in the system dimension (local patch).
6. Calculate ensemble mean of X^f , denoted by \bar{X}^f
7. Calculate prior state error covariance, E^f by calculating the perturbations of X^f (subtract each column of X^f by \bar{X}^f to create E^f)
8. Stack the observations available inside the local patch to Y^o and create the observation error covariance matrix R considering the error of the observation and observation localization weight. Basically, divide observation error by weightage for each pixel observation. This localization forces a large error to far observation and small error to closer observation from the target pixel.
9. Calculate VDV^T using the eq 3.6, then by eigen value decomposition calculate V , $m \times m$ matrix containing eigen vectors whose i^{th} column is the eigenvector q_i of VDV^T and corresponding eigen values are in diagonal elements in D . Then calculate the D^{-1} and $D^{-1/2}$ (by Cholesky factorization) to calculate the $VD^{-1}VT$ and $VD^{-1/2}V^T$.
10. Then calculate posterior estimate, X^a using the eq 3.5

3.3.5 Localization techniques

Not only the observations on target pixel but also the surrounding observations carry information about the target pixel. However, when assimilation distant observation spurious error can occur due to the error covariance occur due to limited ensemble size (Miyoshi et al. 2007). Errors due to the distance observations can be reduced by localization techniques by weighting the observational error covariance according to the distance from the local patch centre. This observation localization can be performed by multiplying the observation error covariance by inverse of localization weighting function such as Gaussian function explained as:

$$w(r) = e\left(-\frac{r^2}{2\sigma^2}\right), \quad \text{eq 3.7}$$

where σ is the localization length and r are the distance between the target pixel and observation.

3.3.6 Number of Ensembles

We limited ensembles to 20 because the computational cost of CaMa-Flood simulations significantly higher than the data assimilation algorithm even though the errors in the Monte Carlo sampling decrease with increasing size n of ensembles following $1/\sqrt{n}$.

3.4 Hydrodynamic model description and implementation

3.4.1 introduction

We used the global river hydrodynamic model CaMa-Flood (Yamazaki et al. 2011, 2012, 2013) to propagate the hydrodynamic parameters over time within our data assimilation framework. CaMa-Flood receives runoff forcing (amount of water entering a river from a unit land area in mm/day) from a land surface model (LSM) as the input forcing (amount of water entering a river from a unit of land area in mm/day), and simulates river and floodplain hydrodynamics (i.e., river discharge, WSE, inundated area, and surface water storage) at the global scale. The spatial resolution of CaMa-Flood (set to 0.25° in this study) is coarser than that of two-dimensional flood inundation models

(typically < 1 km) (e.g., Bates et al. 2010). Instead of solving two-dimensional floodplain flows at a high resolution, CaMa-Flood represents floodplain inundation dynamics using sub-grid topography parameters delineated from fine-resolution topography. While the water mass balance (i.e., surface water storage and river discharge) is explicitly calculated at a coarse-grid resolution, the complex floodplain inundation is represented as diagnostic sub-grid physics. Therefore, CaMa-Flood achieves computationally efficient simulations of global-scale river hydrodynamics.

CaMa-Flood calculates river discharge using a local inertial flow equation (a computationally efficient modification of the shallow water equation) (Bates et al. 2010; Yamazaki et al. 2013). Because the pressure term is considered in the local inertial equation, river discharge is estimated based on the water surface slope. This is a key difference between CaMa-Flood and conventional global river models, which use a kinematic-wave flow equation that neglects the pressure term. The combination of the sub-grid flood inundation scheme and the local inertial flow equation enables a realistic representation of the water surface elevation along river channels and in floodplains. Furthermore, the WSE values simulated using CaMa-Flood were directly comparable to WSE observations based on satellite altimetry (Yamazaki et al. 2012). Though the 0.25° (~ 25 km near the equator) resolution simulation by CaMa-Flood was applicable for large-scale rivers (Yamazaki et al. 2011, 2012), comparison between model and observation might be difficult in smaller and steep rivers. For the fully utilization of satellite altimetry, higher-resolution river model is being developed currently. Therefore, we select CaMa-Flood as the hydrodynamic core of our data assimilation framework.

3.4.2 Channel Cross-section Parameters

The channel cross-section parameters (channel length and channel depth) are estimated by an empirical function of river discharge climatology, while the other topographic parameters are explicitly derived from the fine-resolution flow direction map and DEM. The channel width (w) and channel depth (B) are generated using the following empirical equations:

$$w = \max[0.70 \times R_{up}^{0.75}, 10.0], \quad \text{eq 3.8}$$

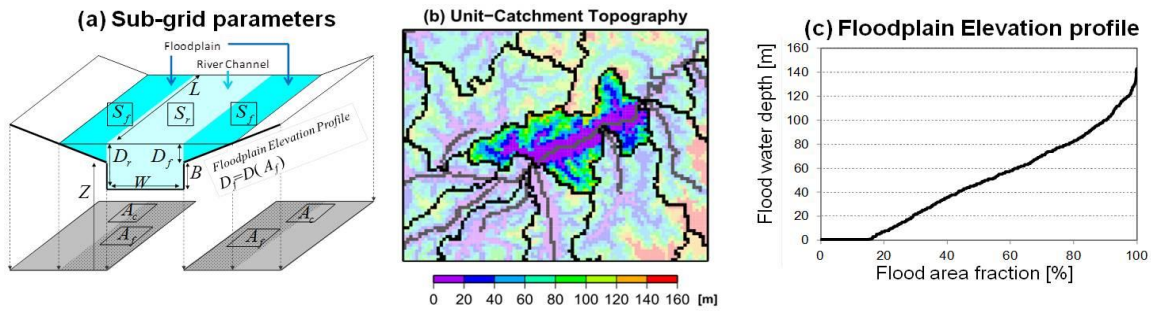


Figure 3.3 : (a) Schematic illustration of the sub-grid parameters for the river channel and floodplains. (b) Unit-catchment topography. The height above the nearest river channel is shown by the background colour. (c) Floodplain elevation profile.

$$B = \max[0.14 \times R_{up}^{0.40}, 2.0], \quad \text{eq 3.9}$$

where W is the channel width (m), B is the channel depth (m), and R_{up} is the annual maximum of 30-day moving average of upstream runoff (m^3s^{-1}).

3.4.3 Input runoff forcing

We used the runoff output from the Minimal Advanced Treatment of Surface Interaction Runoff (MATSIRO) (Takata et al. 2003) LSM as the input runoff forcing for CaMa-Flood. Previous assessments showed that river hydrodynamics were reasonably well represented by the combination of CaMa-Flood and MATSIRO runoff forcing (Yamazaki et al. 2011, 2012, 2013), supporting the use of CaMa-Flood simulations as a ‘virtual truth’ method for the data assimilation framework. For the true simulation, the runoff from MATSIRO (Kim et al. 2009) was used directly, whereas in the corrupted and assimilated simulations, the runoff forcing was intentionally modified to represent uncertainty in runoff data.

3.4.4 Manning’s coefficient

CaMa-Flood model uses a constant Manning’s coefficient values for whole globe (0.03 for river channel flow and 0.1 for floodplains). River channel width and bank height were given as the function of monthly based discharge (Yamazaki et al. 2011). Those empirical parameters were assumed to be identical for all the basins in order to execute global simulations because observations for parameter calibration are not enough in many basins. However, the bathymetry of river channel and the roughness coefficient must vary for each basin (or each sub basin) according to geomorphologic conditions (e.g., slope

and curvature) and geological conditions (e.g., sediment type and grain size). The extensive calibration of the bathymetric parameters and the roughness coefficient for each basin was not performed in this study.

3.5 Synthetic SWOT observations

We generated synthetic SWOT observations at the end of each daily time step using the WSE from the true simulation (Figure 3.4, left). Generation of synthetic SWOT observations followed three steps: (1) obtaining WSE from the true simulation, (2) delineating SWOT observations using the SWOT coverage mask, and (3) adding observation error (following the basic steps presented in Figure 3.4). The true simulation was carried out as described in Section 3.2. The SWOT coverage mask was created using SWOT orbit data, which are available online from the website of the National Centre for Space Studies, France (CNES 2015). Orbit data provide the path of the 120 km wide observation swath containing a 20 km nadir gap for each day of the 21-day orbit cycle. We converted these path data into a 0.25 observation coverage mask with the same grid coordinate system used by CaMa-Flood (Figure 3.4: upper middle). If the centre point of a 0.25 grid was within the observation coverage of the path data, the grid was considered

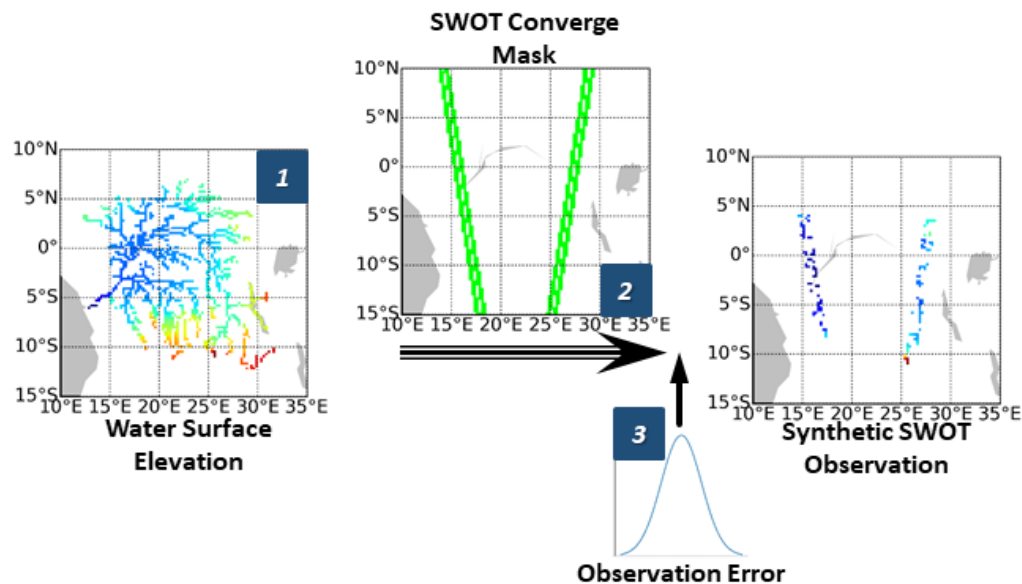


Figure 3.4 : Generation of synthetic Surface Water and Ocean Topography (SWOT) observations. (1) True surface elevation (left), (2) SWOT coverage mask (upper middle: 2), and (3) observational error modelled using a Gaussian distribution (lower middle: 3). Synthetic SWOT observations are presented in the rightmost panel

within the coverage mask. Because the observation area differed daily within the orbit cycle, we prepared 21 coverage masks to generate synthetic SWOT observations for grids containing rivers wider than 50 m within the coverage mask.

We assumed Gaussian random error with zero mean and standard deviation of 5 cm (Figure 3.4, lower right), following previous studies (Yoon et al. 2012; Andreadis et al. 2007; Andreadis and Schumann 2014). SWOT data will have error of less than 10 cm for areas greater than 1 km² (Andreadis and Schumann 2014; Domeneghetti et al. 2018); as the observation error decreases exponentially with increasing averaging area (Andreadis et al. 2007), our assumption about observation error appears valid. The CaMa-Flood grid resolution of 0.25 is about 25 × 25 km near the equator. Therefore, we assume most of the river pixels will have nominal observation error of 5 cm in this study. The true CaMa-Flood WSE is treated with a spatially constant value from a normal distribution with zero mean and 5cm standard deviation.

3.6 Evaluation methods

We used the assimilation index (AI) (Ikeshima et al. 2017) to evaluate the effectiveness of data assimilation in a virtual experiment. AI is calculated from the ratio of river discharge error rates between the assimilated and corrupted simulations, using following equation:

$$AI = 1 - \left| \frac{\text{Assimilated Discharge} - \text{Corrupted Discharge}}{\text{True Discharge} - \text{Corrupted Discharge}} - 1 \right| \quad \text{eq 3.10}$$

AI describes the similarity between the assimilated and true simulations compared to the corrupted simulation. A high AI (near the maximum of 1) indicates that the assimilated discharge is closer to the true discharge than to the corrupted discharge, while a low AI indicates that the assimilated discharge did not have improved accuracy over the corrupted discharge. AI is particularly useful for evaluating the effectiveness of data assimilation, as river discharge in the corrupted simulation is generally 25% lower than that of the true simulation for most places and times. AI is a metric representing the relative effectiveness of data assimilation and not a measure of simulation accuracy, such as the Nash–Sutcliffe (NS) coefficient (Nash and Sutcliffe 1970). In addition, AI can be calculated for any time and location during the experiment, enabling analysis of when and where the data assimilation framework was effective at estimating river discharge.

Furthermore, we used NS coefficient to determine the degree of correction for the discharge estimate based on the assimilation. The root mean square error (RMSE) also used to evaluate the accuracy of the each estimated parameter. To assess the effectiveness of each local patch, we used normalized root mean square error (NRMSE).

3.7 Conclusion

Here we introduced the OSSE, which is methodology to test potential of new measurement (satellite, in situ gauge, etc.) before it is implemented or deployed. In this study we use LETKF assimilation algorithm which is used extensively in numerical weather prediction/reanalysis system (Miyoshi 2011; Anderson 2012). Furthermore, each pixel can be assimilated in parallel due to localization in the LETKF, which completes the update step in the area spanned by the ensembles, and therefore the computational cost of LETKF is considerably lower (Szunyogh et al. 2005, 2008) in global applications. We used CaMa-Flood hydrodynamic model as the core of the data assimilation framework which use to propagate the model states through the time. CaMa-Flood is purposefully developed for the global applications unlike other hydrodynamic modelling frameworks, therefore CaMa-Flood provide us good opportunity to perform data assimilation in global scale. In addition, the synthetic SWOT observations are generated by masking out CaMa-Flood modelled WSE using SWOT orbit data and adding observation error. The evaluation methods used in this study such as; AI, NS, RMSE, and NRMSE are introduced in the context of a data assimilation study.

Chapter 4

Development of a Physically Based Empirical Localization Method for Hydrologic Data Assimilation

4.1 Introduction

River discharge is a key variable for global and regional water cycle assessments(Oki and Kanae 2006). Number of accessible in-situ gaging stations is not adequate for detailed assessments. With the upcoming satellite altimetry missions such as Surface Water and Ocean Topography (SWOT) direct measurements of the water surface elevation (WSE) of inland waters (i.e., river, lakes, wetlands, and reservoirs), will become available(Alsdorf et al. 2007b). Recent advances in data assimilation techniques make it possible to estimate river discharge via satellite remote sensing, complementing data measured by existing in-situ gage networks.

Data assimilation techniques have been used to reduce the uncertainty of hydraulic models, in order to estimate the river discharge(Andreadis et al. 2007; Durand

et al. 2008) but most of these methods only applied to small scale rivers. Different variations of Kalman filtering techniques have been used to assimilate WSE in regional scales such as Extended Kalman Filter (EKF), Ensemble Kalman Filter (EnKF), and Local Ensemble Batch Smoother (LEnBS). EKF, EnKF, and LEnBS are mostly suited for local scale assimilation schemes because of calculation involve large covariance matrix.

Global hydrodynamic data assimilation demands efficient Kalman filtering technique which has the lower computational burden. Global Climate models use Local Ensemble Transformation Kalman Filter (LETKF: Hunt et al. 2007) which uses large amounts of variables in a local patch. Several studies suggest that LETKF can be utilized for estimating the river discharge in a reasonable computational efficiency (Ikeshima et al. 2017). Therefore, LETKF will provide an efficient technique to estimate the river hydrodynamics in global scale.

River discharge shows a large degree of spatiotemporal autocorrelation(Yoon et al. 2012); thus increasing the patch size will make it possible to extract information about the places which cannot be simultaneously or directly observed. But localization techniques should be introduced to avoid spurious errors occur from distant observations because of sampling errors caused by the limited ensemble size(Miyoshi et al. 2007).In LETKF localization is realized by multiplying observational error variance by the inverse of a localization weighting function such as the Gaussian function which referred to as “observation localization”(Miyoshi et al. 2007). So, a novel approach is needed in defining the localizations for river pixels in hydrodynamic models.

River hydrodynamics show large difference depending on the location, affecting the spatial dependency. In most of the hydrodynamic data assimilation schemes a fifth order(Hamill et al. 2001) function was used for covariance localization in EnKF(Munier et al. 2015; Yoon et al. 2012; Biancamaria et al. 2011). In LETKF a Gaussian weighting function was used for observation localization(Miyoshi et al. 2007). Most of the above studies used trial and error method to find the localization parameters. But in the complex river network there was no method have been proposed to find the localization parameters.

The purpose of this chapter is to examine the potential of an adaptive physically based empirical localization method for hydrologic data assimilation for continental-scale rivers. We develop empirical localization parameters considering (e.g. local patch,

localization weight) the autocorrelation of WSE and test them using operating system simulation experiment (OSSE). Then empirical local patch performance is compared with conventional local patch methods.

4.2 Methodology

Mainly our methodology for determining decorrelation length of each river pixel consists of two major steps 1) transforming daily water surface elevation (WSE) data suitable for semi-variogram analysis, 2) finding the auto-correlation lengths for each river pixel using semi-variogram analysis.

WSE data were obtained by a CaMa-Flood hydrodynamic model simulation for 1980 to 2000. Runoff forcing data was obtained by the Minimal Advanced Treatment of Surface Interaction Runoff (MATSIRO) land surface model (LSM). Atmospheric forcing variables for LSM (precipitation, temperature, radiations, pressure, humidity, and wind speed) were prepared based on the atmospheric reanalysis data provided by Japanese Meteorological Agency Climate Data Assimilation System.

4.2.1 Data transformation

When performing semi-variogram analysis, the data should first be transformed into a time series that is normally distributed, with seasonality removed (Skøien et al. 2003). Therefore, a number of transformation steps were implemented, each using the data from the previous step, starting with CaMa-Flood-modeled daily WSE data. Three steps were used for transformation of data: 1) removing trends, 2) removing seasonality, and 3) standardizing.

Some hydrological time series may have trends in the time domain (i.e. Global Warming, Deforestation, Land Surface Changes) that can be represented by a simple straight line. Therefore, we calculated the intercept and gradient using the time series of CaMa-Flood-modeled WSE for 1980 to 2000, and then subtracted the trend represented by the straight line

$$y = a + bt, \quad \text{eq 4.1}$$

where y is WSE, t is time (in days), b is gradient, and a is the intercept of the line:

$$b = \frac{(n \sum yt - \sum y \sum t)}{(n \sum t^2 - (\sum t)^2)}, \quad \text{eq 4.2}$$

$$a = \bar{y} - b\bar{t} \quad \text{eq 4.3}$$

where n is number of data points, \bar{y} and \bar{t} are mean of y and t respectively

We removed seasonality, to avoid exaggerating temporal dependence, using Fourier representation; a periodic function was fitted to the data using a sum of the sine and cosine functions (Chiverton et al. 2015) at frequencies that are integer multiples of the annual cycle, as well as half- and quarter-year cycles. For each river pixel, the number of covariates was set to six to allow a good fit to the data (more covariates increase the flexibility of the function, enabling a better fit to the data). The effect of seasonality was removed by deducting the magnitude of changes caused by seasonality, calculated from the periodic function, for each day in the time period considered.

The WSE data with trend and seasonality removed were standardized for each model grid by subtracting the mean and dividing by the standard deviation of the time series. Standardizing enables comparison of locations with different magnitudes of WSE.

4.2.2 Semi-variogram analysis

A theoretical semi-variogram will exhibit a monotonic increase with increasing lag distance from the ordinate of appropriate shape until it reaches a constant maximum or asymptote, called a ‘sill’ Figure 4.1. A semi-variogram has several components, as shown in Figure 4.1. The ‘sill’ is defined as the semi-variance where the gradient of the semi-variogram is zero. A gradient of zero indicates the limit of temporal dependence and is an indicator of the total variance between the ordinate and the surroundings. The ‘range’ is the time required to reach the zero gradient. The positive intercept on the ordinate is the ‘nugget’.

An experimental semi-variogram was calculated for each pixel using the average squared difference between all pairs of values that are separated by a spatial distance lag. As noted above, the experimental semi-variogram is calculated as follows:

$$\gamma(\vec{h}) = \frac{1}{2N} \sum_{i=1}^N (Z_i - Z_{i+\vec{h}})^2, \quad \text{eq 4.4}$$

where γ is the experimental semi-variance, h is the lag distance, N is the number of data

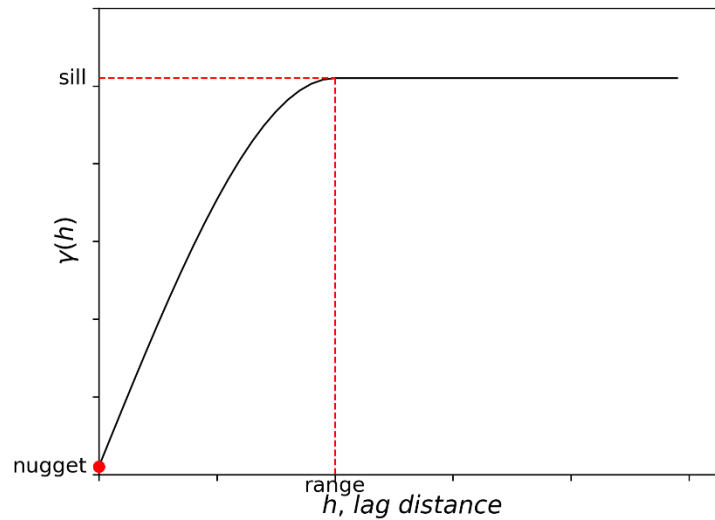


Figure 4.1 : Example of Semi-variogram

points, and Z is the variable considered, in this case standardized WSE.

A semi-variogram model, selected from the conventional semi-variogram models including Spherical, Cubic, Gaussian, Pentaspherical, Sine hole effect and Exponential, was fitted to the data using a weighted least-squares method with the Levenberg-Marquardt algorithm, an optimal solution for parameter estimation of nonlinear functional models (Yonathan Bard 1970). We identified the best performing semi-variogram model as that with the lowest Akaike's Information Criterion (AIC) value. We determined the sill, range, and nugget corresponding to the best fitted semi-variogram using the weighted least squares method.

4.2.3 Empirical determination of the local patch

After finding the corresponding sill, range and nugget from the best-fitting semi-variogram model, the experimental data were inverted to obtain a distribution with unity for the ordinate and zero outside of the range (auto-corrected length). We fitted semi-variograms for the upstream and downstream areas independently for each river pixel. Then, the experimental semi-variance was converted to a weighting term representing the spatial dependency, hereafter the spatial dependency weighting. Values closer to 1 indicate higher spatial dependency and those closer to zero show low spatial dependency. Furthermore, we allocated the largest weight to common upstream river stems in the target pixel. We defined the threshold for spatial dependency weighting to derive the

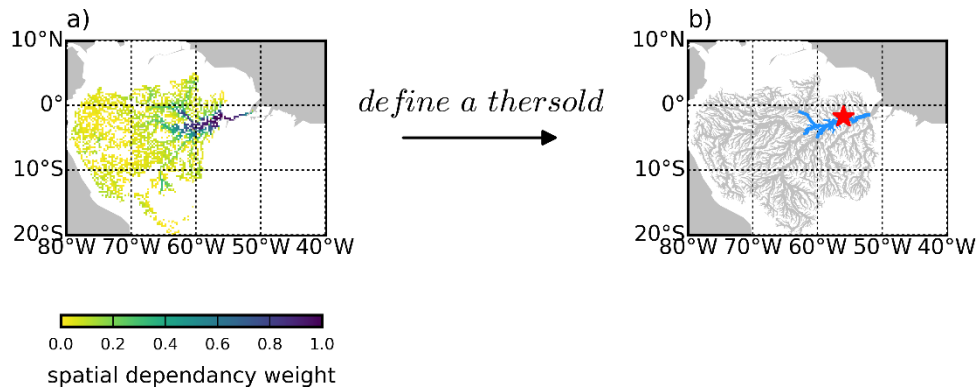


Figure 4.2 : Schematic diagram of the delineation of the empirical local patch for the target pixel indicated by a red star. (a) Spatial dependency weights and (b) local patch. River pixels inside the local patch are shown in blue, while other river pixels are shown in grey.

empirical local patch. In this study, we treated each river pixel independently and determined the empirical local patch for each pixel. Schematic representation of deriving empirical local patch is presented in Figure 4.2. By defining a threshold (0.6) to the spatial dependency weightage (Figure 4.2a) to define an empirical local patch as shown in Figure 4.2b for the target pixel in red star.

4.2.4 Deriving observation localization weights

We derived the observation localization weighting factor to force large errors for distant observations in the LETKF algorithm. In this study, we used a Gaussian function to calculate the localization weight (Miyoshi et al. 2007).

$$w(r) = e\left(\frac{-r^2}{2\sigma^2}\right), \quad \text{eq 4.5}$$

where σ is the localization length and r are the distance between the target pixel and observation.

Here, we use a lag distance corresponding to the threshold of spatial dependency weighting (used to define the local patch) as the limiting value, and the weight to drops to zero beyond that lag distance following a fifth-order piecewise rational function (Hamill et al. 2001). Therefore, we calculated σ as follows:

$$\sigma = \frac{1}{2} \sqrt{\frac{3}{10}} a, \quad \text{eq 4.6}$$

where a is the lag distance corresponding to the threshold used to define the local patch. We did not assimilate observations beyond the lag distance a from the target pixel.

4.2.5 Experimental conditions for assess empirical local patch

We test the developed empirical local patches and the localization parameters using observing system simulation experiment (OSSE). Then we compared the performance of empirical patch with the other conventional local patch methods.

4.2.5.1 Observing System Simulation Experiment

We used an observing system simulation experiment (OSSE) (Andreadis et al. 2007; Yoon et al. 2012) to assess the potential for assimilating river bathymetry at the continental scale. The OSSE consisted of three separate simulations: ‘true simulation’, ‘corrupted simulation’, and ‘assimilated simulation’ (Ikeshima et al. 2017). The CaMa-Flood hydrodynamic model (Yamazaki et al. 2011) was used to generate the true, corrupted, and assimilated simulation estimates for the data assimilation framework in this study.

To create synthetic SWOT observations, we performed the true simulation to generate the true virtual water state, which was continuous in space and time. In the true simulation, the river hydrodynamic model was forced by true (assumed to be true) input runoff forcing (or non-corrupted runoff) and river bathymetry, and the true water state (river discharge, WSE, and water storage) was generated. Then, synthetic SWOT observations were generated by applying a SWOT coverage mask delineated from orbit data (CNES 2015) to the true WSEs, followed by the addition of noise. Therefore, we assumed that only a portion of the true water state (i.e., WSEs in the SWOT observation area, with some observation errors) was known when data assimilation was performed.

A ‘corrupted simulation’ was performed to compare the corrupted state of the model with the assimilated and true simulations. The corrupted simulation used in this study was executed with corrupted model settings (i.e., corrupted input runoff forcing, corrupted Manning’s coefficient) representing both forcing and parameter/formulation errors. All other parameters (i.e., river channel depth, river width, elevation) in the corrupted simulation were identical to those in the true simulation. Furthermore, noise

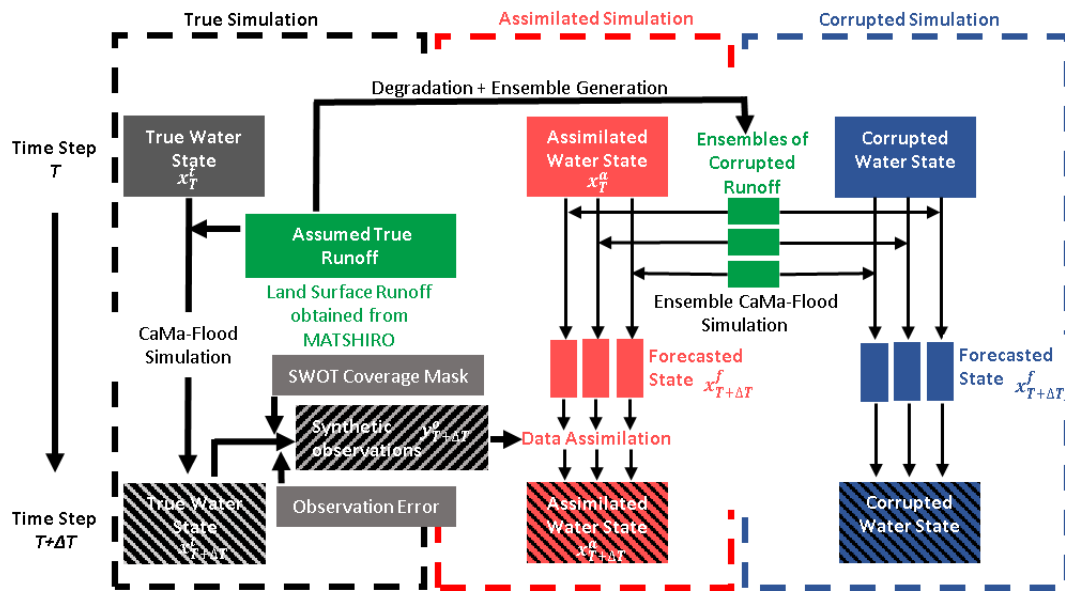


Figure 4.3: General framework of the observing system simulation experiment (OSSE)

was added to the corrupted settings (runoff and Manning’s coefficient) to generate the ensemble states required for the assimilation procedure.

We executed the ‘assimilated simulation’ to test the potential for using SWOT observations to estimate discharge. We used the same model settings as for the corrupted simulation, but with assimilation of synthetic SWOT observations. At the end of each day, the synthetic SWOT observations were assimilated into the water state forecast, and the initial conditions of the simulation for the following day were updated to reflect the assimilated water state.

4.2.5.2 Hydrodynamic model implementation

We used the runoff output from the Minimal Advanced Treatment of Surface Interaction Runoff (MATSIRO) (Takata et al. 2003) land surface model (LSM) as the input runoff forcing for CaMa-Flood. Previous assessments showed that river hydrodynamics were reasonably represented by the combination of CaMa-Flood and MATSIRO runoff forcing (Yamazaki et al. 2011, 2012, 2013), supporting the use of CaMa-Flood simulations as a ‘virtual truth’ for the data assimilation framework. For the true simulation, the runoff from MATSIRO (Kim et al. 2009) was used directly, whereas in the corrupted and assimilated simulations, the runoff forcing was intentionally modified to represent uncertainty in the runoff data. Though the 0.25° (~ 25 km near the

equator) resolution simulation by CaMa-Flood was applicable for large-scale rivers (Yamazaki et al. 2011, 2012), comparison between model and observation might be difficult in smaller and steep rivers. Furthermore, we conducted the experiment for 1 year using runoff forcing from 2008. The initial conditions of the true simulation were set using 2007 true runoff data.

We added an artificial bias to the true runoff forcing to create the corrupted runoff, following previous SWOT assimilation experiments (Andreadis et al. 2007). Thus, the corrupted runoff value was generated through addition of a -25% bias to the true runoff forcing. In general, river discharge and WSE in the corrupted simulation are 25% smaller than those of the true simulation, due to the bias added to the runoff forcing. The initial conditions of the corrupted and assimilated simulations were generated using corrupted runoff data for 2007.

In this study, the ensemble of model simulations was represented using multiple runoff forcing. We used 20 ensembles in this study, even though errors in Monte Carlo sampling decrease with increasing ensemble size (Evensen 2009). The ensemble size strongly affects the computational cost of data assimilation because the CaMa-Flood model has a higher computational burden than data assimilation. We prepared 20 different runoff forcing conditions by adding a random Gaussian noise variable to the corrupted runoff, to simulate 20 different forecasted water states in the assimilated simulation. The standard deviation of the Gaussian noise was set to 25% of the monthly mean runoff value.

Furthermore, the artificially corrupted Manning's coefficients were used for the corrupted and assimilated simulations to represent errors in model parameters or formulation. In the true simulation, Manning's coefficient was set based on the original CaMa-Flood model (0.03 for river channel flow and 0.1 for flood plain). Meanwhile, for the corrupted and assimilated simulations, Manning's coefficient (river channel flow) was determined by multiplying the original Manning's coefficient by a Gaussian noise term representing the unit mean and 25% standard deviation. However, Manning's coefficient is distributed approximately normally in the range of 0.0225 to 0.0375 for the river channel. Manning's coefficients for natural streams seems to be vary between 0.02 to 0.05 according to Chow 1959, Barnes 1967, and Akan 2006. In addition, the error of the model should not to be very large, hence the assimilation always finds the observation is much accurate. Therefore, we select CaMa-Flood Manning's coefficient to be normally

distributed between -25% to $+25\%$ of the original Manning's coefficient in assimilated and corrupted simulations.

4.3 Experimental Settings

We performed three different OSSEs, referred to as the “Empirical”, “Zero” and “Fixed” local patch experiments, to examine the efficiency of the assimilation scheme. We examined the potential of the empirical local patch to assimilate distance observations without being affected by the error covariance due to the limited ensemble size. In the empirical patch experiment, empirically derived local patches were used for assimilation. A conventional fixed square-shaped local patch was used in the fixed local patch experiments. We assimilated observations only in the target pixel for the Zero local patch experiment. The details of these experiments are explained in following sections for the empirical, zero and fixed local patch experiments, respectively.

4.3.1 Empirical local patch experiment

Here, we derive the adaptive local patch shapes and sizes to filter the error covariance observations as much as possible; such filtering cannot be achieved using the conventional local patch. Empirical local patches were derived from CaMa-Flood-modeled WSE for each river pixel separately. First, CaMa-Flood-modeled WSE for 1980 to 2000 was converted into spatial dependency weights. This spatial dependency weighting was derived from the auto-correlation length, which was obtained from semi-variogram analysis. Calculating spatial dependency weights involved four steps: (1) removing trends, (2) removing seasonality, (3) standardizing, and (4) finding auto-correlation lengths. Then, we derived the empirical local patches by defining the spatial dependency weight threshold for each river pixel separately. We used those developed empirical local patch in Empirical local patch experiment.

4.3.2 Conventional local patch experiments

We performed three different OSSEs namely, “Zero” and “Fixed” local patch experiments to compare the efficiency of the assimilation scheme with empirical local patch. We examine the potential of the empirical local patch to assimilate distance observations without affected by the error covariance due to limited ensemble size. A conventional fixed square shaped local patch is used in fixed local patch experiments. We

assimilate the observation only in the target pixel in the Zero local patch experiment. The details of the fixed local patch experiments are explained in following sections.

4.3.2.1 Zero local patch experiment

Here we assimilate the river pixels only when direct observation is available at that pixel and WSE of only the observed pixel is updated. Therefore, we did not consider any observation localization techniques here as we do not assimilate distant observations.

4.3.2.2 Fixed local patch experiment

Here we performed two OSSE with assimilation scheme using two different conventional square shaped local patches. The local patch sizes for two fixed local patch OSSEs are 11×11 pixels for small, and 21×21 pixels for large local patches. Schematic representation of delineating conventional fixed local patch is shown in Figure 4.4. The corresponding localization parameters of small and large local patch were 1000km and 3000km, respectively and those observation localization weights were calculated considering the river length. Here after we name the two OSSEs as: “Fixed-Small” local patch OSSE for 11×11 and “Fixed-Large” local patch OSSE for 21×21 grids. In Fixed-Small and Fixed Large local patch assimilation schemes are equivalent to the assimilation windows used in the studies by Durand et al. 2008, Andreadis and Schumann 2014, respectively.

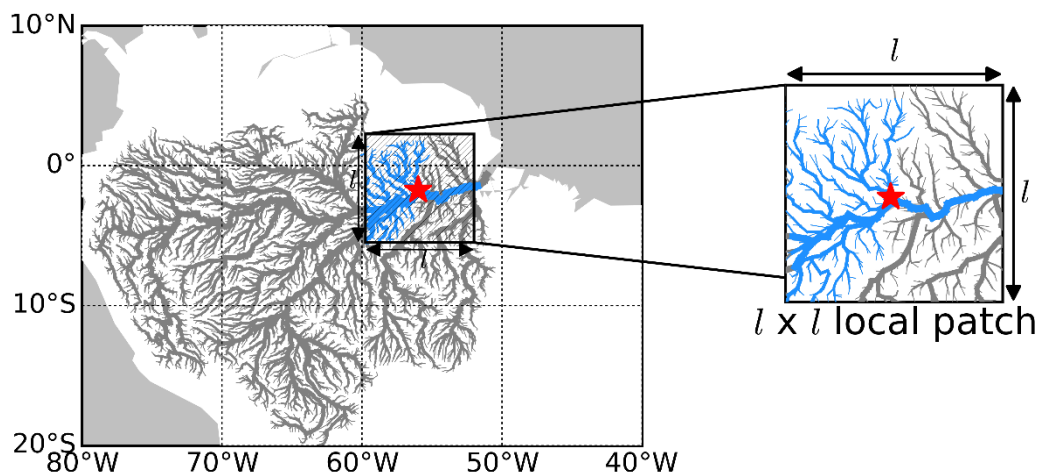


Figure 4.4 : Schematic diagram of the delineation of the conventional $l \times l$ fixed local patch for the target pixel indicated by a red star (l , number of pixels). River pixels inside the local patch are shown in blue, while other river pixels are shown in grey

4.4 Results

4.4.1 Validating CaMa-Flood Discharge

CaMa-Flood discharge was compared with GRDC observation of the stations for some major rivers. Figure 4.5 shows the comparison of CaMa-Flood modelled river discharge (blue) and GRDC observation (black) for Amazon, Congo, Mississippi, Lena, Ob, Brahmaputra, Mekong, and Yenisei rivers. Discharge of these observation stations' Nash-Sutcliffe (NS) coefficients suggest that the model predictions are more accurate than the mean of the observed data. Therefore, model predictions can be used as the representative variables for non-observed variables.

We used the Nash-Sheffield (NS) coefficient to evaluate the potential of usage CaMa-Flood simulated data for developing empirical local patch. NS coefficient is presented in each panel of the Figure 4.5 for GRDC locations of Amazon, Congo, Mississippi, Lena, Ob, Brahmaputra, Mekong, and Yenisei rivers. Obidos GRDC location in Amazon River indicate the highest NS coefficient and lowest is at Kinshasa GRDC location in Congo River. Most of those CaMa-Flood simulated discharge emulate the observation data.

4.4.2 Empirical localization parameters

We conducted semi-variogram analysis to derive the empirical localization parameters (local patch size and observation localization weight) using transformed CaMa- Flood-modeled WSE data. This section contains the results of deriving these localization parameters.

Derivation of empirical localization parameters using semi-variogram analysis involves two major steps: 1) transforming daily WSE data to be suitable for semi-variogram analysis, and 2) finding the weights for each river pixel using semi-variogram analysis.

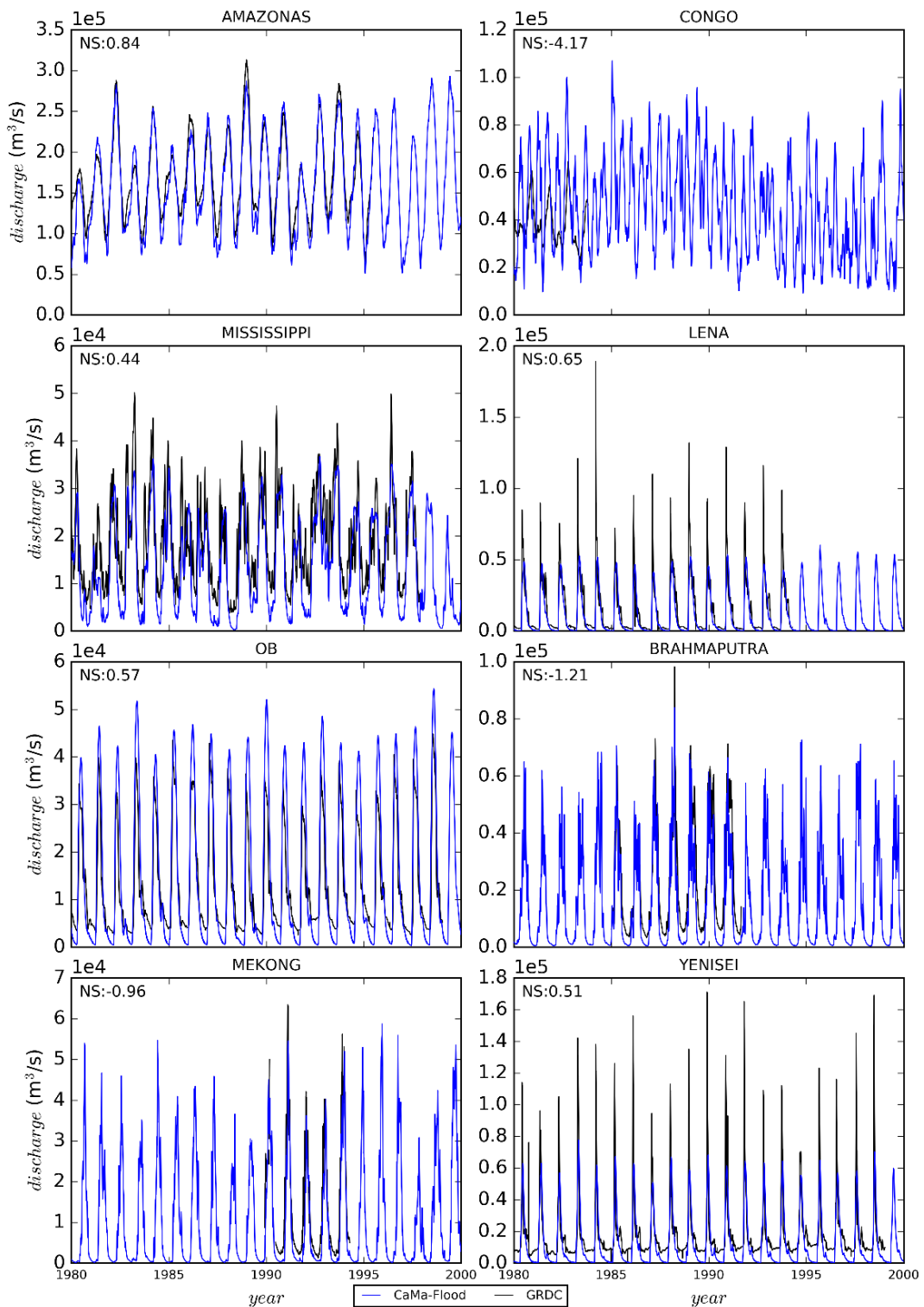


Figure 4.5 : Hydrographs for the Amazon, Congo, Mississippi, Lena, Ob, Brahmaputra, Mekong, and Yenisei. GRDC observation data is presented in black and CaMa-Flood simulated discharge is presented in blue. Nash-Sheffield coefficient is shown in upper left corner.

4.4.2.1 Data transformation

The CaMa-Flood-modeled WSE data were transformed into a variable that exhibits less periodicity with a distribution close to normal (Skøien et al. 2003) for semi-variogram according to the Kolmogorov-Smirnov, D'Agostino K-squared, Shapiro-Wilk, and analysis, as the CaMa-Flood-modeled daily WSE did not follow a normal distribution Anderson-Darling statistical tests (Table 4.1 shows summary of the results for the statistical test for Obidos GRDC location in Amazon River). We transformed the data by removing possible trends and seasonality from the CaMa-Flood-modeled daily WSE and then standardizing the data.

A slight upward or downward trend can be seen for each river pixel in the basin, with a magnitude of 10^{-4} (Figure 4.6). This may possibly indicate that there is an increment in the runoff but it not possible to distinguish whether it is from the increment in mean precipitation or changes in the land surface as we did not either perform an LSM modelling or precipitation analysis.

Our Fourier transformation showed higher spectrum densities near the frequency of the annual cycle (1/365 Hz). In the Figure 4.6b) red curve shows the seasonality curve fitted by Fourier representation and grey curve represents the trend and seasonality removed WSE data. In order to represent the intra-annual and inter-annual cycles we used frequencies represent integer multiples of annual cycle, and the 6-months and 3-months cycles to fit the seasonality curve shown in Figure 4.6b) (red). Furthermore, we used 6 covariates for each frequency in case the cycle is not exactly equal to desired frequency but very close to the desired frequency and it will increase the flexibility of the function, enabling a better fit to the data.

Histograms of transformed WSE data verify that transformation brought the CaMa-Flood-modeled WSE data much closer to a normal distribution, with zero mean and unit standard deviation. After transformation through removing trends, removing

Table 4.1 : Results of the statistical tests for normal distribution for Obidos, Amazon River

Test	Kolmogorove-Smirnov	D'Agustino K-squared	Shapiro-Wilk	Anderson-Darling
Statistic	0.96	4873.09	0.96	82.31
p-value	0.0	0.0	0.0	-

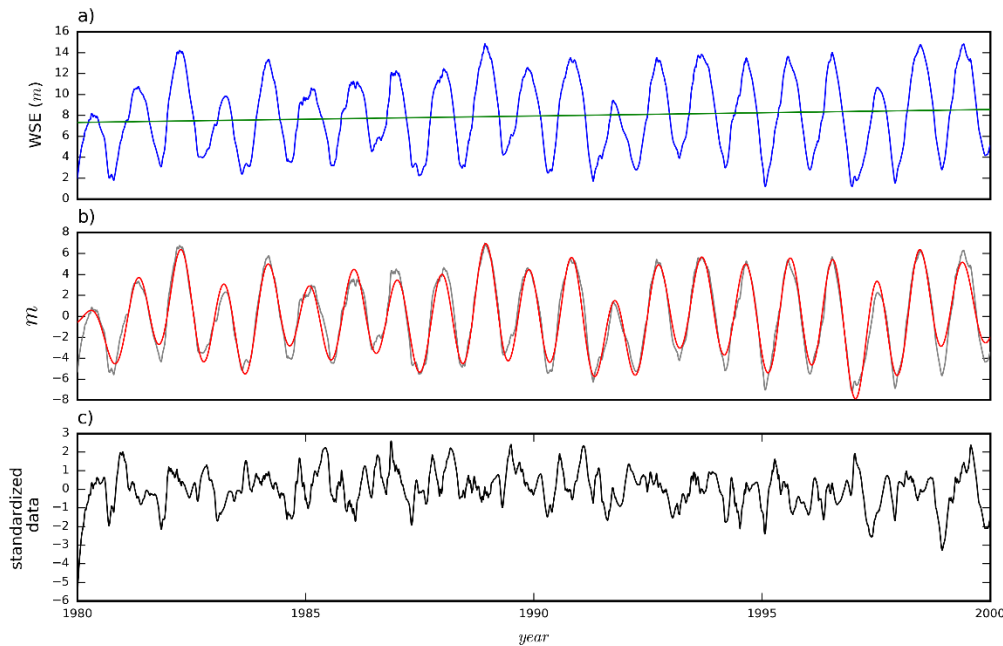


Figure 4.6: Timeseries of a) modelled WSE (blue) and trend line (green), b) trend removed WSE (grey) and seasonality curved fitted by Fourier representation (red), and c) standardized data of trend and seasonality removed WSE (black) for Obidos GRDC location of Amazon River

seasonality, and standardizing the CaMa-Flood modelled WSE data shows closer to a normal distribution (Figure 4.7). In Figure 4.7 a histogram of transformed data of Obidos GRDC location of Amazon River with mean of 0 and standard deviation of 1.0. Broken red line indicate the normal distribution curve.

4.4.2.2 Semi-variogram analysis

Standardized data which was transformed into a normally distributed data used to fit semi-variogram model using the weighted least-squares method using Levenberg-Marquardt algorithm. Different semi-variogram models were fitted to the experimental semi-variogram data such as Spherical, Cubic, Gaussian, Exponential, and Pentaspherical and Akaike's Information Criterion (AIC) was used to find the best fit among the above models. AIC takes into account not only the goodness of fit but the parsimony of the model as well (Jian et al. 1996). The estimate of this criterion is:

$$\hat{AIC} = n \ln \left(\frac{R_m}{n} \right) + 2p, \quad \text{eq 4.7}$$

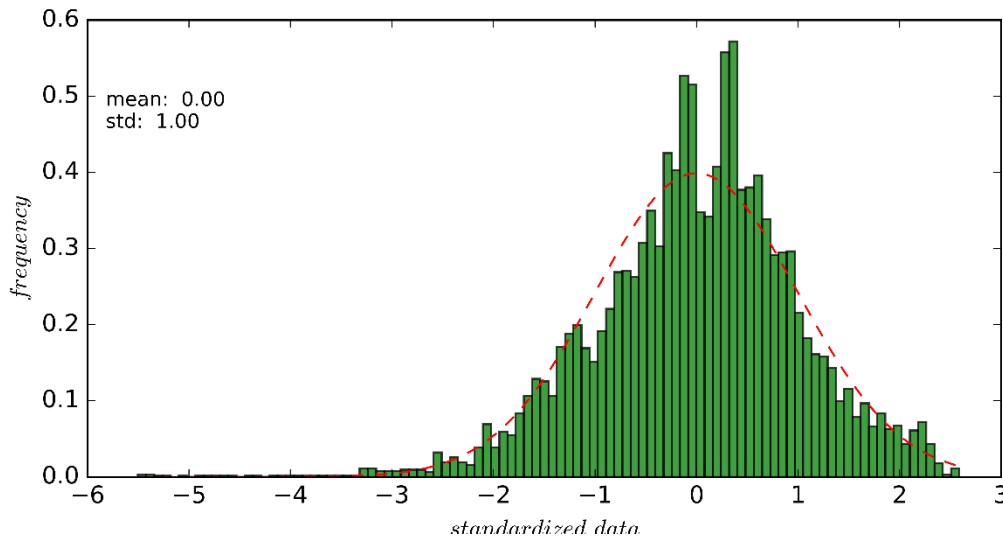


Figure 4.7 : Histogram of standardized WSE data of Obidos GRDC location of Amazon River. Red dashed line indicates the normal distribution with 0.0 mean and 1.0 standard

where n is the number of points in the experimental semi-variogram, R_m is the sum of the square of the weighted differences, and p is the number of parameters in the model.

Table 4.2 presents mean AIC value for each theoretical semi-variogram models namely, Spherical, Cubic, Gaussian, Exponential, and Pentaspherical. From the Table 4.2, it is revealed that the Gaussian semi-variogram model performs better than another model. Therefore, we used Gaussian semi-variogram model to find the characteristics of the semi-variogram (sill and range).

Figure 4.8 shows one of the examples for the fitted semi-variogram for the Obidos GRDC location, Amazon River Figure 4.8a) represents the semi-variograms of upstream and Figure 4.8b) downstream of the Obidos GRDC location. Fitted semi-variogram is

Table 4.2 : Mean AIC values for different semi-variogram models

Semi-variogram model	mean AIC
Spherical	-152.97
Cubic	-188.49
Gaussian	-189.09
Pentaspherical	-151.58
Sineholeeffect	-124.23
Exponential	-145.91

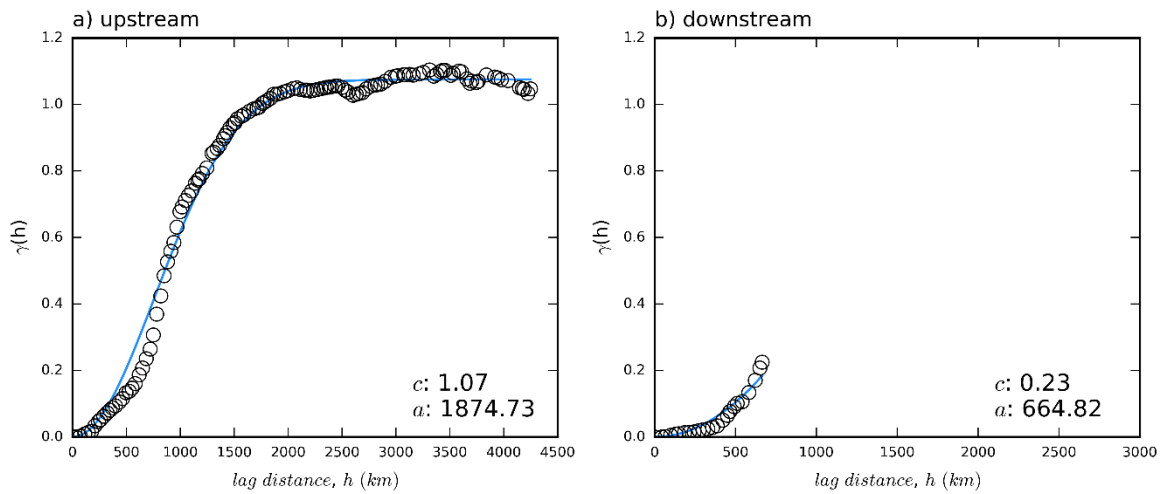


Figure 4.8 : Fitted semi-variogram (blue line) and Experimental semi-variogram (black circle) of a) upstream and b) downstream of Obidos GRDC location of Amazon River. Semi-variogram was fitted using the weighted least-squares method. Sill and range are shown in the lower right corner.

presented in blue and the experimental semi-variogram is shown in black circles. Average AIC values of semi-variogram models such as Spherical, Cubic, Gaussian, Pentaspherical, Sineholeeffect, and Exponential are tested and we found that Gaussian model shows the lowest AIC value for the Amazon River. Therefore, we adopt Gaussian semi-variogram model for Amazon (Figure 4.8). It should be noted that if the fitted range of the semi-variogram is greater than the largest lag distance of experimental semi-variogram the largest lag was considered as the auto-correlation length. Fitted Gaussian semi-variogram revealed (Figure 4.8) the range for upstream is 1874.73 km and downstream is 835208.44 km for Obidos GRDC location but respectively 1874.73 km and 664.82 km are considered as the autocorrelation lengths. Furthermore, we found that the large tributaries (Negro, Jupura, Jurua, Purus, and Madeira) have larger auto-correlation lengths and vice-versa. It suggests that the large tributaries have much dependency than small tributaries.

4.4.2.3 Empirical weighting of spatial dependency

We fitted several semi-variogram models (i.e. Spherical, Cubic, Gaussian, Pentaspherical, Sinehole effect and Exponential) to the transformed WSE data to determine the sill and range, as in Figure 4.1. The best performing semi-variogram model was identified as that with the lowest AIC value (Revel et al. 2018). Then, the fitted parameters (sill and range) were used to convert the experimental semi-variances into

empirical spatial dependency weightings. The spatial dependency weightages for each river pixel was calculated by subtracting the ratio between the semi-variance and sill of the fitted semi-variogram from unity. Thus, the spatial dependency weightage represents the spatial auto-correlation between target pixel and the surrounding river pixels.

Figure 4.9 indicates the spatial dependency weights based on the maximum correlated upstream river reach to the downstream correlated river length in the Amazon River. Zero indicate the target pixels and positive values are for downstream and negative distances for upstream along the maximum correlated upstream. Analysis suggests that the correlated length (inverted weighting) can be explained by: 1) change in the WSE slope and/or 2) discharge from the connecting tributary. Figure 4.9 shows a classic example of a mild WSE slope limiting the correlation length (inverted weighting); the weighting is almost zero when the WSE slope is large beyond the lag distances of -1,000 km upstream and 500 km downstream. At a lag distance of -1,000 km upstream, the WSE slope becomes very steep due to topographic changes (weighting drops from 0.8 to almost zero). So, the correlations beyond -1,000 km is rapidly reduced. In the downstream pixels, the downstream correlated length is limited by the distance to the river mouth, which

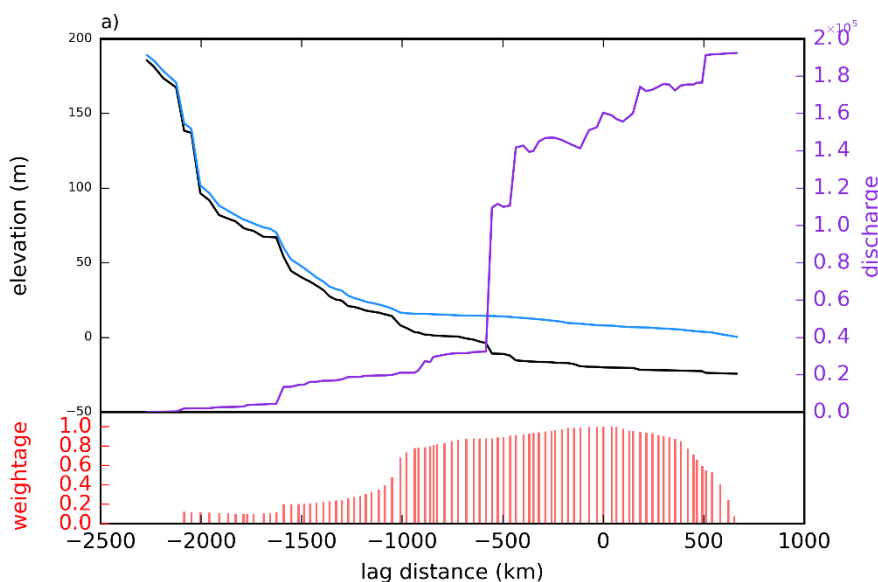


Figure 4.9: Variation of spatial dependency as a weighting factor (red vertical lines) along each river stem, with target pixels. The upstream area has the largest correlated length. The horizontal axis shows the distance from the target pixel, with negative values being upstream and positive downstream. A bathymetric profile is shown in black. The average water surface elevation (WSE) is indicated in blue. The average discharge is shown in indigo. Average values are calculated for 1980-2000.

causes a sharp gradient in the weight. This result suggests that the derived localization weights have more physical basis than the conventional Gaussian or fifth-order piecewise rational function localization weighting functions.

4.4.2.4 Selecting local patches

The local patches used for the target pixels were selected through derived weighting based on semi-variogram analysis. We used a weighting threshold of 0.6 to derive the local patches, while considering the effectiveness of assimilating observations with weights of less than 0.6 and spurious error caused by distant observations due to the limited ensemble size. Example of local patches for target pixels Obidos GRDC location in Amazon River is shown in Figure 4.10. We derived the local patches for each river pixel, which have unique shapes and sizes according to the river's hydrodynamics.

The size of each empirical local patch is determined from the river hydrodynamics, and therefore empirical local patches derived for different river pixels had different sizes (Figure 4.12a). Large rivers are associated with large empirical local patches (in terms of area), whereas the empirical local patches of small rivers are small. Large river stems show a right - skewed distribution of empirical local patch sizes, with a mean of 50 pixels. Medium and small rivers show relatively small spread with mean pixel sizes of 9 and 5, respectively. Therefore, small rivers have relatively smaller local patches, while large rivers have large local patches.

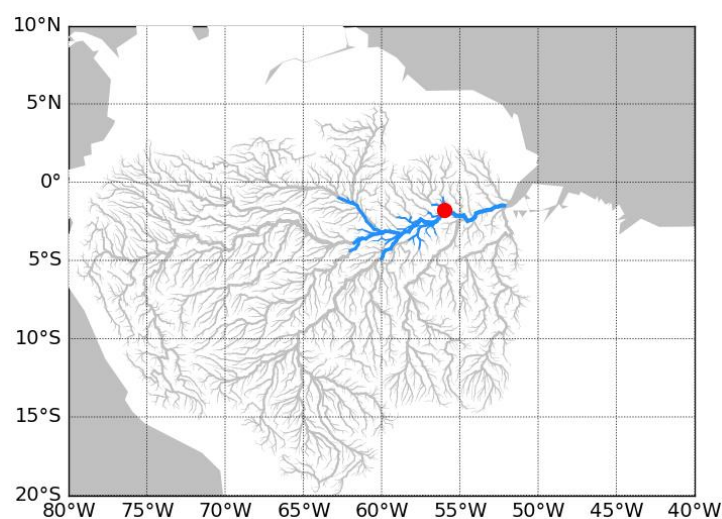


Figure 4.10: Local patches for target pixels (red circles) in the Amazon River (blue area), with locations. Red circles indicate the target pixels. Grey denotes major tributaries of the Congo River.

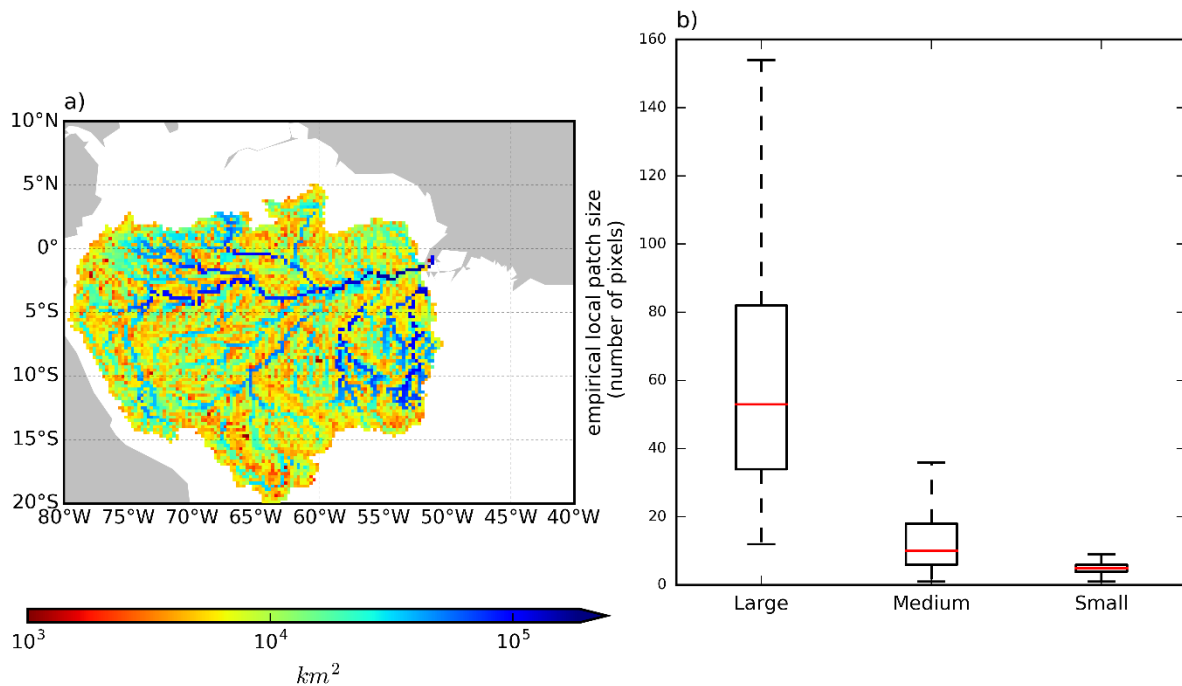


Figure 4.12 : (a) Size of the empirical local patch for the Congo basin (as area, km^2). (b) Box plot of the empirical local patch sizes (number of pixels) for large (watershed area $\geq 10^5 \text{ km}^2$), medium ($10^5 \text{ km}^2 > \text{watershed area} \geq 5000 \text{ km}^2$), and small (watershed area $< 5000 \text{ km}^2$) river pixels.

4.4.2.5 Observation availability

Figure 4.11 shows the number of observations available for one assimilation cycle inside the derived local patch (indicated by the light blue bars) for Obidos GRDC location in Amazon River. Days with direct SWOT observations are indicated by red stars. Here, we assume that SWOT observations have the same resolution as the CaMa-Flood model for a virtual experiment. Observations at Obidos GRDC location, which is represented by

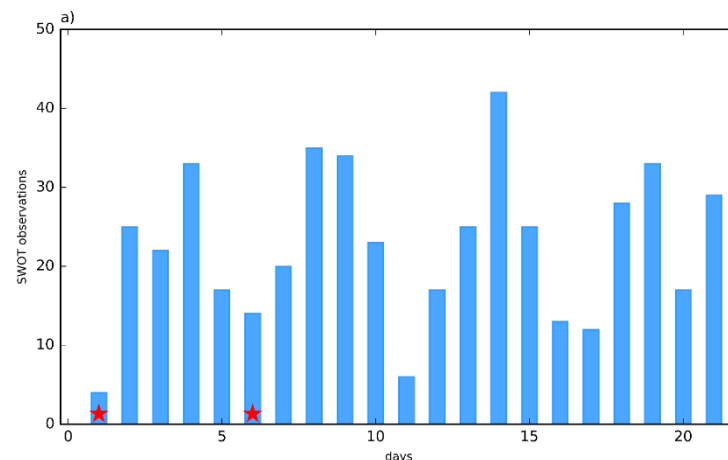


Figure 4.11 : Number of SWOT observations in the derived local patch (light blue). Red stars indicate days for which direct SWOT observations are available.

only two direct SWOT observation per SWOT cycle, increased to 474 per cycle. Hence, by deriving an empirical local patch, the observation frequency increases by a large margin compared to direct observations.

4.4.3 Empirical Local Patch Experiment

We demonstrate the effectiveness of hydrological data assimilation using Empirical local patch by conducting an observing system simulation experiment (OSSE) in this section. Furthermore, we present the details of the assimilation and computational efficacy of our method. In this section, we discuss the results of the data assimilation scheme developed using empirical local patches and evaluate the potential of a future SWOT mission to estimate river discharge in a situation with 25% negatively biased runoff. A relative effect was determined using AI, considering Obidos GRDC location in Amazon River.

4.4.3.1 Discharge estimation

Hydrograph for Obidos GRDC location during the simulation period (366 days) are shown in Figure 4.13. Red, blue, and black lines indicate the assimilated, corrupted and true discharge values, respectively. The green line represents AI. When the true and corrupted discharges are very similar (within 10%), we used a light green line to indicate AI. Green dots on the AI curve represent days with direct observations for the target pixel. Mean AI and percentage bias (pBias) are provided in the upper left corner.

Figure 4.13 shows the hydrograph for Obidos GRDC location in Amazon River. The assimilated (red line) and the true (black line) discharge are similar for most of the simulation period, except for beginning of January. The corrupted discharge is constantly negatively biased by roughly 25%. This indicate the annual mean AI of 0.97 and AI value stays high ($AI > 0.8$) for whole simulation. The transitioning from the initial-corrupted state to the well-assimilated sate takes around 15 days for Obidos GRDC location.

4.4.3.2 Assimilation Efficiency

Annual mean AI of Amazon basin is presented in the Figure 4.14, where the annual mean discharge was greater than $500 \text{ m}^3/\text{s}$. The annual mean AI was computed for each grid to compare the effectiveness of data assimilation spatially. Annual mean AI is

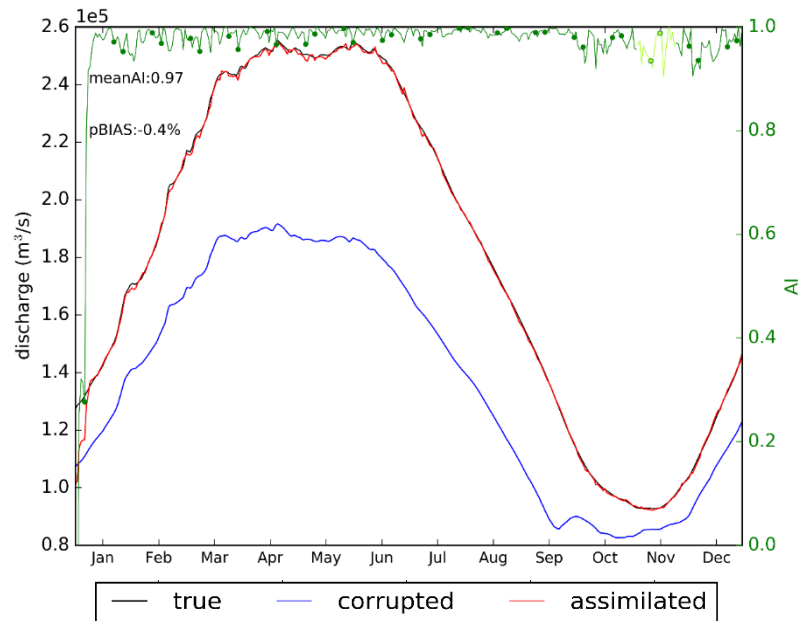


Figure 4.13: Hydrograph of the Kinshasa for year 2008. True, corrupted, and assimilated discharge values are indicated by black, blue, and red lines, respectively. The thin blue and red lines show the ensembles of corrupted and assimilated discharge, respectively. The assimilation index (AI) is shown in green, and the light green line indicates the bias of corrupted discharge relative to true discharge. Green dots represent the times of synthetic SWOT observations.

nearly 1 for most large tributaries (Figure 4.14), indicating good assimilation. We excluded days from the calculation of annual mean AI if the pBias was $< 10\%$ of the corrupted discharge, with respect to the true discharge. The main stem and large

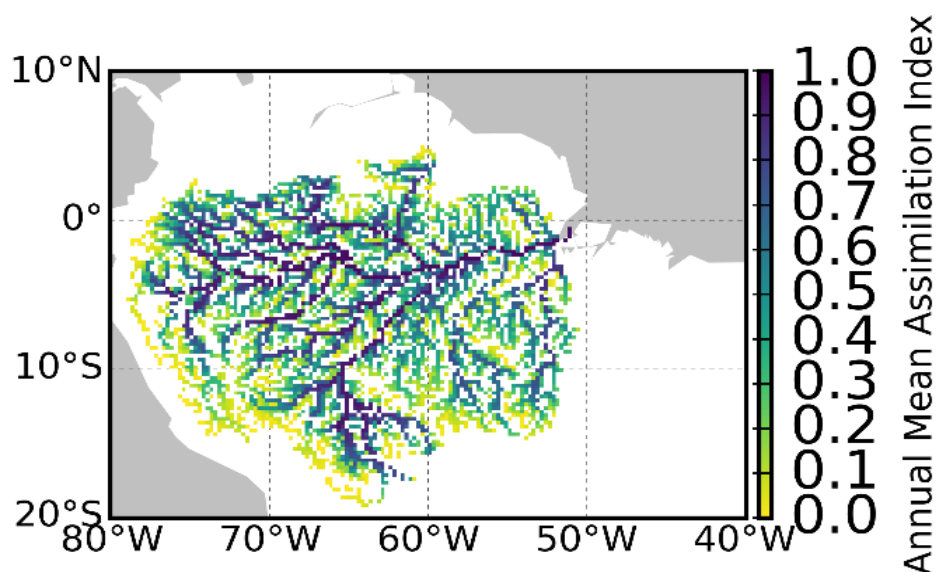


Figure 4.14 : Annual mean AI of Amazon basin. Pixels $> 100 \text{ m}^3/\text{s}$ presented for visualization purposes.

tributaries (Jupura, Negro, Solimoes, Juruá, Purus, Madeira, Tapajós, and Xingu) of the Amazon River have high mean AI values (> 0.8), and other tributaries also exhibit relatively high mean AI (> 0.6). Only the most upstream river pixels show very low AI (< 0.3). Although most upstream sites have low efficiency of assimilation, the majority of the Amazon River appears to be reasonably well estimated, with river discharge estimates close to the true values.

4.4.4 Comparison among OSSEs

Figure 4.15 represents the hydrographs for Empirical, Zero, Fixed-Small, and Fixed-Large experiments in panels a–d, respectively, for the GRDC location at Obidos on the Amazon River. Annual mean AI indicates that empirical patch assimilation outperformed other assimilation methods. Ensemble spread is lowest in the Empirical local patch experiment and increased in the order of Zero, Fixed-Small, and Fixed-Large OSSEs. Comparison with the hydrograph from Obidos (which is on the main stem of the Amazon River) revealed that the empirical local patch scheme is best among the Empirical, Zero, Fixed-Small, and Fixed-Large local patch assimilation schemes in terms of mean AI and ensemble spread.

We found that the low assimilation efficiency of the Empirical local patch experiment was caused by the low observation frequency. As noted above, the observation frequency increased with the use of a larger local patch. However, the annual mean AI of both fixed local patch experiments are smaller than that of the zero patch OSSE. This discrepancy is primarily due to two factors: 1) uneven distribution of SWOT cycle observations (Figure 4.17) and 2) low spatial dependency of the observations in small tributaries on the target pixel (tributaries that the empirical local patch did not include) (Figure 4.16). The empirical local patch contains more than 20 observations for each day of the 21-day SWOT cycle (Figure 4.17), whereas for fixed local patches (Fixed-Small and Fixed-Large), observations are available only on days 1, 6, 11, 12, 16, and 17 for Fixed-Small experiment (Figure 4.17b); and 1, 2, 5, 6, 7, 11, 12, 13, 16, 17, 18, and 21 for Fixed-Large (Figure 4.17c). Furthermore, spatial dependency along the main stem of the Amazon River appears up to 1000 km upstream. In the fixed local patches, such spatial dependency was not considered for assimilation. Thus, the empirical local patch for Obidos on the Amazon River performs better than the fixed local patches.

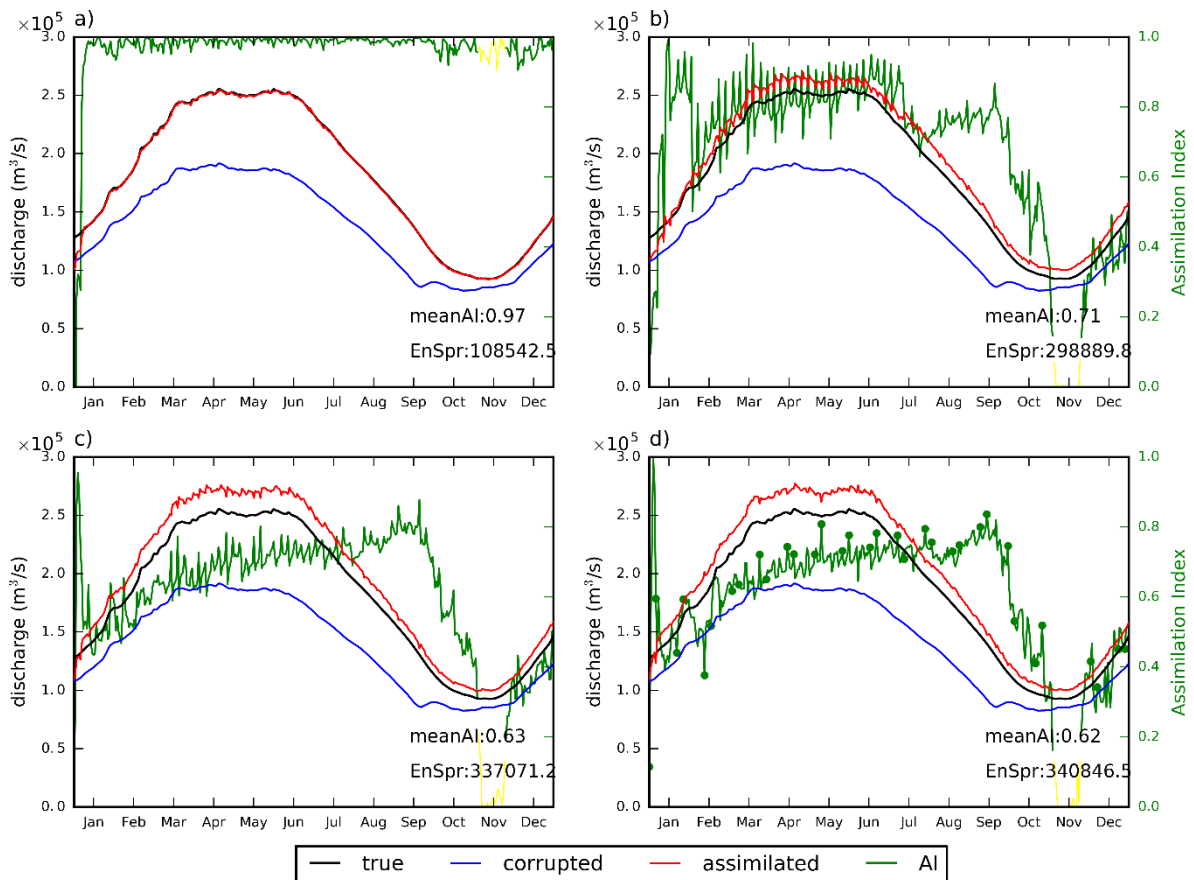


Figure 4.15 : Hydrograph at Obidos for the year 2008 in the a) Empirical, b) Zero, c) Fixed-Small, and d) Fixed-Large local patch experiments. True, corrupted, and assimilated discharge values are indicated by black, blue, and red lines, respectively. The thin blue and red lines show the ensembles of corrupted and assimilated discharge, respectively. The AI is shown in green, and the light green line indicates the bias of corrupted discharge relative to true discharge. Green dots represent the times of synthetic SWOT observations. The mean AI and ensemble spread (EnSpr) of the assimilated simulation are shown in the lower-right corner of each hydrograph.

In Figure 4.18a–c, we present the difference in mean annual AI between the empirical local patch experiment and the Zero, Fixed-Small, and Fixed-Large local patch experiments, respectively. For most places on the Amazon River, the annual mean AI of the Zero local patch was one unit (difference ≈ 0.1) lower than that obtained from the Empirical local patch experiment. The Fixed-Small and Fixed-Large OSSEs show a similar pattern, where large streams have lower annual mean AI than the Empirical patch experiment (Fixed-Small: 0.1~0.3, Fixed-Large: 0.3~0.5). Meanwhile, the upstream sites and smaller tributaries show slightly elevated AI in the fixed local patch experiment. Thus,

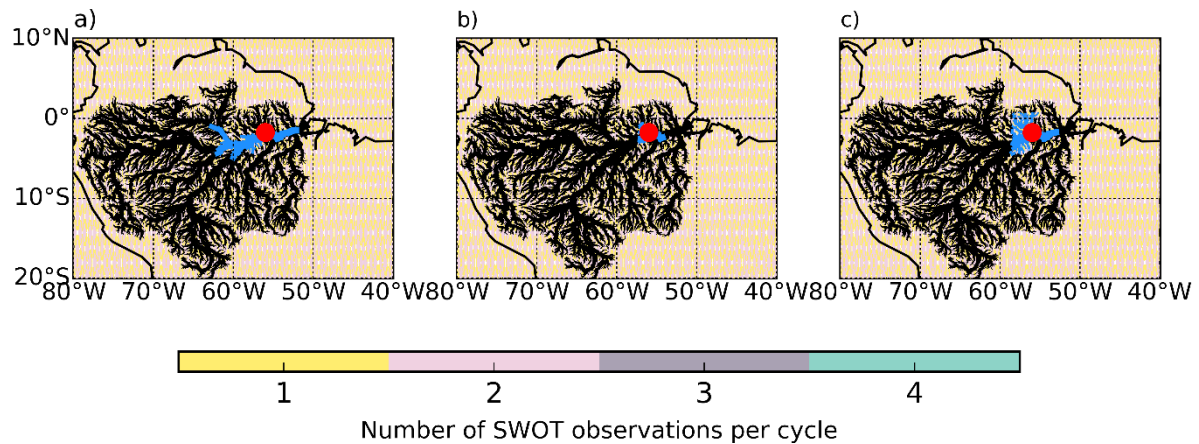


Figure 4.16 : Local patch for Obidos used in the a) Empirical, b) Fixed-Small, and c) Fixed-Large local patch experiments (blue). Background colour indicates the number of SWOT observations per cycle. The Amazon River network is shown in black. Red circle indicates the target pixel.

assimilation of the empirical local patch is better than that of the Zero local patch for most of the Amazon River and better than the Fixed-Small and Fixed-Large local patches in downstream reaches of large river stems.

4.4.5 Very large local patch assimilation

We carried out a very large local patch OSSE, using 81×81 pixels with 20 ensembles, in addition to the Zero, Fixed-Large, Fixed-Small, and Empirical local patch experiments. We found that WSE assimilation leads to large errors caused by error covariance between small tributaries due the limited ensemble size. Several researchers

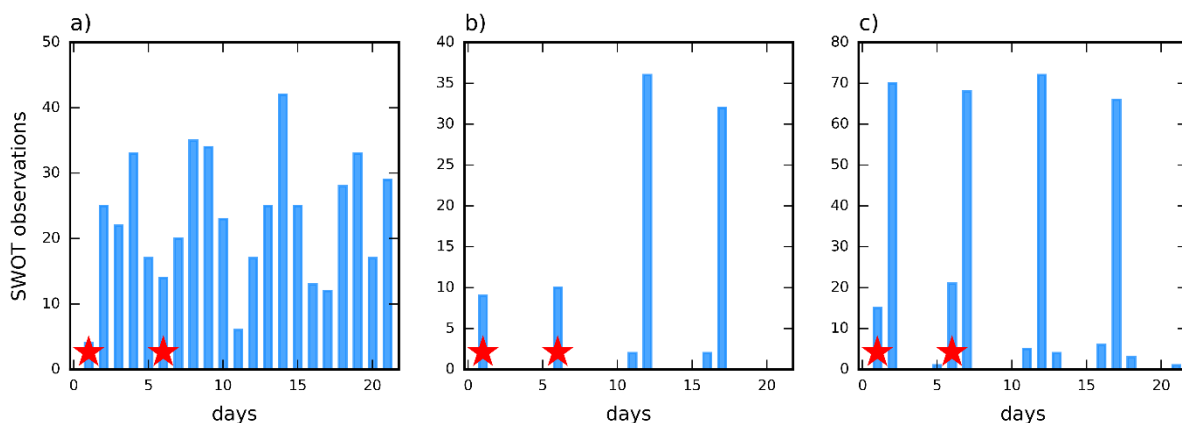


Figure 4.17 : Number of SWOT observations in the a) Empirical, b) Fixed-Small, and c) Fixed-Large local patches (light blue) for Obidos. Red stars indicate days for which direct SWOT observations are available.

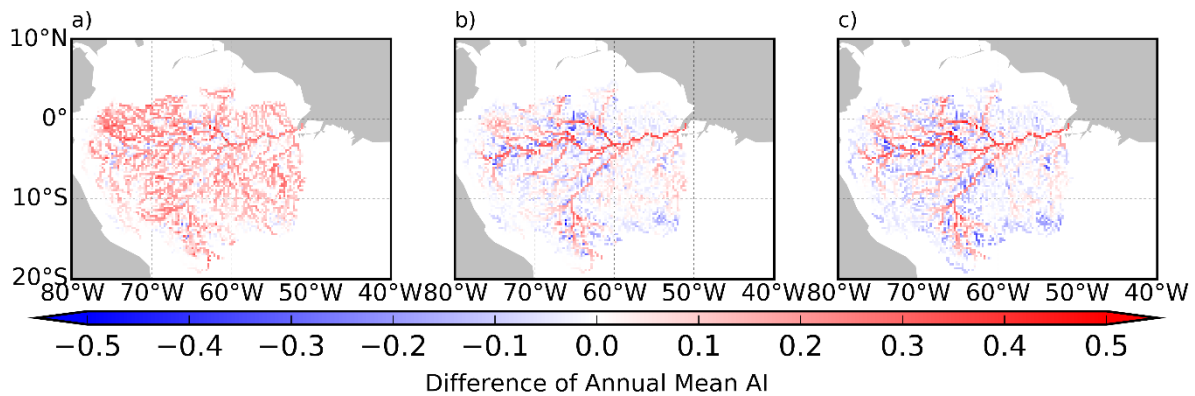
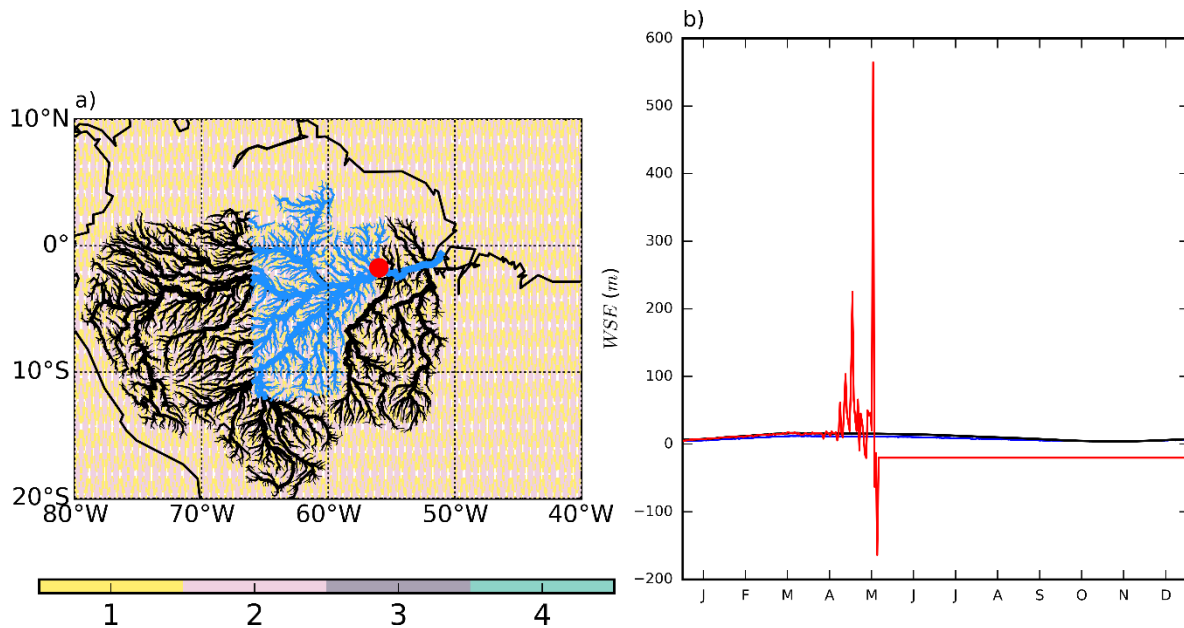


Figure 4.18 : Difference in the annual mean AI between the Empirical and a) Zero, b) Fixed-Small, and c) Fixed-Large local patch experiments. Pixels with annual mean discharge $> 100 \text{ m}^3/\text{s}$ are shown for visualization purposes.

have reported spurious errors caused by error covariance due to limited ensemble size when assimilating distant observations in NWP. Our adaptive empirical local patches can effectively filter observations with error covariance and extend the local patch to utilize the maximum possible number of observations.

Figure 4.19 present an example of the very large fixed local patch data assimilation in Obidos GRDC location in Amazon basin. The size and shape of the local patch is presented in Figure 4.19a and the time variation of WSE is presented in Figure 4.19b. The WSE values have very high errors after May, indicating that the assimilation became inefficient. The discharge is very large after around April ($> 1 \times 10^{20}$) at Obidos. These spurious errors are due to error covariance between non-significantly correlated areas and the target pixels. Even though this large patch can utilize more observations (similar number of observations on the main stem) than the empirical local patch, it cannot filter out areas affected by error covariance from the assimilation. The empirical local patch only includes locations with significant correlations, particularly along the main stem at Obidos. Therefore, increasing conventional local patch size introduces more errors into the assimilation.

A conventional fixed local patch is not effective at utilizing information from distant observations due to the fixed shape and size. When extending the size of a fixed local patch to capture significantly correlated areas (such as those included in the empirical local patch; Figure 14a), other areas with non-significant correlations are also included. Therefore, error covariance between small tributaries causes spurious correlations. More strict localization (Fixed-Small local patch) reduces errors due to non-



Number of SWOT observations per cycle
 Figure 4.19 : a) Local patch with the number of SWOT observations (colours) and b) time series of WSE of Obidos. The Amazon River network is shown in black. Red circle indicates the target pixel.

significant correlation areas but disregards flow-dependent areas with significant correlations. Consequently, the conventional fixed local patch technique is effective for utilizing available observations while removing error covariance.

Local patch size can be adjusted according to observation error and ensemble size in the assimilation. In this study, we assumed that observation error could be represented as spatially uncorrelated, following a Gaussian distribution with a mean of zero and standard deviation of about 5 cm, in accordance with previous works (Andreadis et al. 2007; Biancamaria et al. 2011). Moreover, we limited the ensemble size to 20 members. Depending on the observation error and ensemble size, the threshold for identifying the local patch based on the spatial dependency weight can be adjusted; importantly, this will increase the availability of observations.

4.4.6 Assimilation efficiency

Figure 4.20 presents a comparison of the NRMSE values of different OSSEs. The zero, fixed-small, fixed-large, and empirical local patch experiments have mean NRMSE values of 0.064, 0.075, 0.079, and 0.016, respectively, after rounding to the third decimal point. All experiments have lower NRMSE values than the corrupted state (blue line in

Figure 16). In the first 2 months (January and February), the lowest NRMSE was observed for the empirical local patch. This finding indicates that conversion from the initial state to the well-assimilated state is efficient in the empirical local patch assimilation scheme. Thus, the empirical local patch OSSE performed well in terms of estimating discharge and efficiently converting the corrupted initial state to the well-assimilated state.

When comparing NRMSE among experiments (Figure 4.20), NRMSE values from all experiment other than the empirical local patch were similar, while the empirical local patch experiment shows a markedly lower NRMSE. In all experiments aside from the empirical local patch experiment, the localization weight was calculated along the river, rather than from the spatial distance, using Hubeny's formula. Therefore, weights are qualitatively similar for the same location. NRMSE is calculated using the mean ensemble discharge, and does not reflect the ensemble spread of assimilated discharge. Mean NRMSE is lower for the empirical local patch OSSE, largely because of the efficiency of transformation from the initial corrupted state to the well-assimilated state.

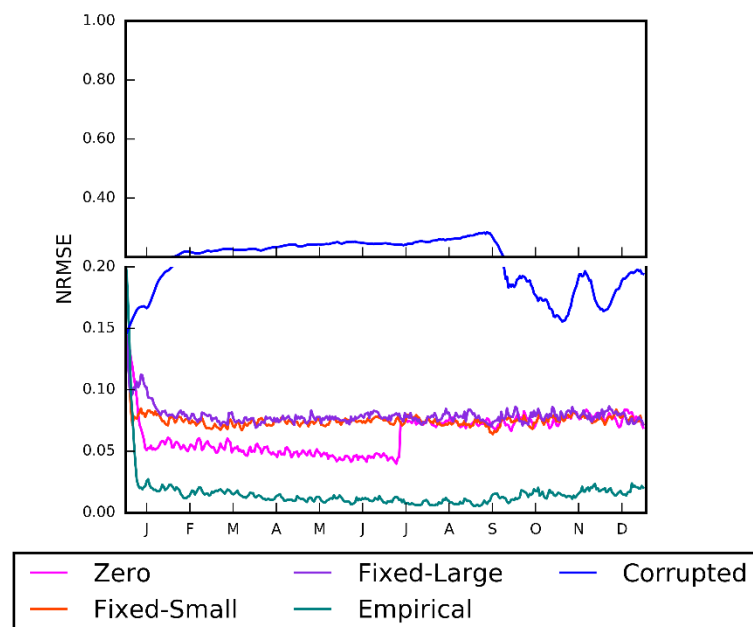


Figure 4.20 : Time series of normalized root mean square error (NRMSE) of assimilated discharge in the zero (magenta), fixed-small (red), fixed-large (violet), and empirical (cyan) local patch OSSEs. Blue line indicates the NRMSE of the corrupted simulation. The fixed-small and fixed-large patches were 11×11 and 21×21 pixels, respectively. The y-axis has been stretched to enhance the visibility of low NRMSE values

Figure 4.20 shows that the empirical local patch experimental NRMSE is lowest in January and February. When sufficient observations were available, NRMSE converged to a similar value in the zero, fixed-small, and fixed large experiments. The latter part of the simulation benefitted from the increased number of direct observations and propagation of the inflow correction from upstream areas. Large errors in NRMSE (January–March) in the large local patch experiment may be the result of spurious error covariance due to sampling errors caused by the limited ensemble size for assimilating distant observations. Thus, the small fixed local patch can be used as a simplified method for empirical local patches, but it is essential that localization be performed along the river.

4.5 Conclusion

In this chapter we primarily developed an efficient data assimilation method considering the spatial autocorrelation of the WSE for continental-scale hydrologic data assimilation. The CaMa-Flood modelled WSE was transformed into distribution which is similar to a normal distribution. The transformation involves three steps namely; remove linear trends, remove seasonality, and standardization. Then the experimental semi variances calculated considering the spatial autocorrelation of the river WSE was converted to a spatial dependence weightage. Those spatial dependency weights were found to follow the trends of the hydrodynamics of the surrounding river WSE (i.e. mild slopes, topography changes etc.). Using the spatial dependency weights, we derived adaptive empirical local patches for each river pixel. The observation localization weightages for LETKF data assimilations were derived considering distance from target pixel to the edge of the empirical local patch (according to Gaussian function (Miyoshi et al. 2007)).

We compared the empirical localization technique with three localization techniques namely, Zero, Fixed-Small, and Fixed-Large local patches, to evaluate the potential of physically-based localization parameters for use in hydrological data assimilation using LETKF. We conducted semi-variogram analysis to determine the spatial dependency weights and derived local patches by defining a threshold in these weights. A fixed number of grids were used for each of the Zero (1×1), Fixed-Small (11×11), and Fixed-Large (21×21) local patch experiments. Then, we compared the four OSSEs with synthetic SWOT observations for 2008 (366 days) and found that the

Empirical local patch experiment estimated river discharge more efficiently than the fixed local patch assimilation methods. The empirical local patches were derived adaptively for each river pixel, with consideration of spatial auto-correlation. We were able to use the maximum number of observations for assimilation without promoting error covariance due to the limited sample size by using empirical local patches. Conventional local patches cannot filter based on error covariance of observations, which lead to spurious errors from small tributaries. Using the empirical local patch technique allows use of distant observations, which cannot be effectively used with the conventional local patch method. Therefore, the limitations of conventional patches can be overcome using empirical local patches.

The Empirical local patch OSSE results suggested that SWOT observations have the potential to improve continental-scale river discharge with the use of physically based spatial dependency parameters. Overall, assimilation was effective for the entire Amazon Basin, with high AI values even in upstream river sections where direct observations are unavailable (river width < 50 m). The hydrodynamics of continental-scale rivers can be well estimated by assimilating SWOT observations using an empirical local patch, even when the model formulation and input runoff forcing contain errors. Hence, our study provides a useful technique for improving observation frequency by enlarging the local patch in an effective manner and performing data assimilation at the continental-scale with a low computational burden.

In our comparison of the fixed and empirical local patch experiments, we note that the latter OSSE has a lower mean NRMSE over the entire simulation. The Fixed-Large local patch experiment is most strongly affected by sampling errors due to limited ensemble spread when assimilating distant observations. The NRMSE of the initial months (January–February) suggested notable differences between the small and empirical local patch OSSEs, showing that the transition from the initial-corrupted state to the well-assimilated state is highly effective with an Empirical local patch OSSE.

We used a simple error structure for both input runoff forcing and model parameters. Future studies should test more complicated error structures, including those that may be spatially correlated. Future studies should focus on developing a hybrid system that combines conventional and empirical localization techniques to overcome the limitations (i.e., assimilation in upstream areas).

Chapter 5

Estimating Global River Discharge using Satellite Observations with Runoff Forcing Uncertainty

5.1 Introduction

River discharge is a key variable for understanding the global hydrological cycle and making water resources assessments (Oki and Kanae 2006). Networks of in situ stream gauging stations are a fundamental data source for estimating spatial and temporal variations in the discharge of major rivers worldwide. However, the numbers of accessible stream gauges are not adequate to fully understand details of the global hydrological cycle, and real-time access to gauged discharge data is usually only available in developed countries. Although remote sensing of river discharge is a challenging research topic, recent advances in satellite observations are expected to enhance our understanding of river discharge variation on the global scale (Marcus and Fonstad 2010). The Surface Water and Ocean Topography (SWOT) satellite is a next-generation satellite

altimetry mission slated to launch in 2021 (Lee et al. 2010). This satellite will measure the two-dimensional distributions of water surface elevations within its 120 km wide swath using the Ka-band Radar Interferometer (KaRIn). For inland regions, the water surface elevations of rivers and lakes will be measured at a <100 m spatial resolution with approximately 5–10-day intervals, depending on the location during its 21-day repeat-cycle orbit (Biancamaria et al. 2016). The fine spatial resolution will encompass rivers wider than 50–100 m (Pavelsky et al. 2014) and lakes larger than 1–5 ha (Lee et al. 2010), providing unprecedented details of surface water dynamics. In addition to water surface elevations, the high-resolution measurements will also provide accurate information on water surface slopes along river networks. Although the SWOT satellite cannot directly measure river discharge, some algorithms to estimate discharge from SWOT-observable variables (e.g., water surface elevation, slope, and width) have been developed (Gleason and Smith 2014; Durand et al. 2016; Garambois and Monnier 2015). These algorithms are able to estimate river discharge in some ungauged rivers with approximately 35% root mean square error (Durand et al. 2016; Bonnema et al. 2016); however, these satellite-based methods cannot produce spatially and temporally estimates of continuous river discharge because of limited observation frequency. Therefore, possibilities for integrating SWOT measurements with river hydrodynamic models (i.e., data assimilation) have been examined (e.g. Andreadis et al. 2007; Biancamaria et al. 2011; Pedinotti et al. 2014). The potential benefits of assimilating future SWOT observations into river hydrodynamic models have been assessed based on a framework called the “virtual satellite experiment” (Andreadis et al. 2007). Because the SWOT satellite has not yet been launched, the virtual experiment generates synthetic SWOT observations using an assumed-to-be-true river hydrodynamics model, and the synthetic observations are assimilated into a corrupted hydrodynamics model. The ability of the data assimilation framework is evaluated by comparing the estimated river discharge improved by the assimilation against the ‘true’ simulation. Some SWOT assimilation frameworks have already been developed and tested in several river basins, including a 50 km reach of the Ohio River (Andreadis et al. 2007), the main stem of the Ob River (Biancamaria et al. 2011), and the Niger River (Pedinotti et al. 2014; Munier et al. 2015). These studies demonstrated the potential for using SWOT observations to improve river hydrodynamic simulations and estimate river discharge continuously in space and time. However,

previous SWOT assimilation frameworks were only developed for single-river reaches or regional-scale river basins, although the SWOT satellite will observe surface waters on a global scale. The applicability of SWOT observations for a continental-scale, or even a global-scale, needs to be discussed.

Therefore, the purpose of this chapter was to use SWOT observations to evaluate the potential of estimating river discharge on a global scale. To this end, we introduced a new data assimilation framework for integrating future SWOT observations into a global river hydrodynamic model. Using the Catchment-based Macro-scale Floodplain (CaMa-Flood) global river model (Yamazaki et al. 2011) and a highly efficient data assimilation method called local ensemble transform Kalman filter (LETKF), we achieved global-scale data assimilation at a reasonable computational cost. A detailed description of the new assimilation framework and initial evaluation results are explained in the following sections.

5.2 Methodology

5.2.1 Framework of the virtual assimilation experiment

We used an observing system simulation experiment (OSSE: explained in section 3.2) (Andreadis et al. 2007; Yoon et al. 2012) to assess the potential estimation of discharge through assimilation of WSE at the continental scale. The OSSE consisted of three separate simulations: the ‘true simulation’, ‘corrupted simulation’, and ‘assimilated simulation’. The CaMa-Flood hydrodynamic model (Yamazaki et al. 2011) was used to generate the true, corrupted, and assimilated simulation estimates for the data assimilation framework in this study.

To create synthetic SWOT observations, we carried out the true simulation to generate the true virtual water state, which was continuous in space and time. In the true simulation, the river hydrodynamic model was forced by true (i.e., assumed to be true) input runoff forcing (or non-corrupted runoff) and true water state data (river discharge, WSE, and water storage) were generated. Then, synthetic SWOT observations were generated by applying a SWOT coverage mask delineated using orbit data (CNES 2015) to the true WSEs, followed by addition of Gaussian noise. Therefore, we assumed that only a portion of the true water state was known (i.e., WSEs in the SWOT observation area with some observation errors) when data assimilation was performed.

The ‘corrupted simulation’ was carried out to compare the corrupted state of the model with the true and assimilated simulations. The corrupted simulation in this study was executed using corrupted model settings (i.e., corrupted input runoff forcing, corrupted Manning’s coefficient) representing errors in both forcing and formulation parameters. All other parameters (i.e., river channel depth, river width, elevation) in the corrupted simulation were identical to those in the true simulation. Furthermore, noise was added to the corrupted settings (runoff and Manning’s coefficient) to generate the ensemble states used in the assimilation procedure. The data assimilation using LETKF was not performed in this simulation.

We executed the ‘assimilated simulation’ to test the potential utility of SWOT observations for estimating discharge. We used the same model settings employed in the corrupted simulation, but with assimilation of synthetic SWOT observations. At the end of each day, the synthetic SWOT observations were assimilated into the water state forecast, and the initial conditions of the simulation for the following day were updated to reflect the assimilated water state. The assimilation of WSE was carried out using LETKF.

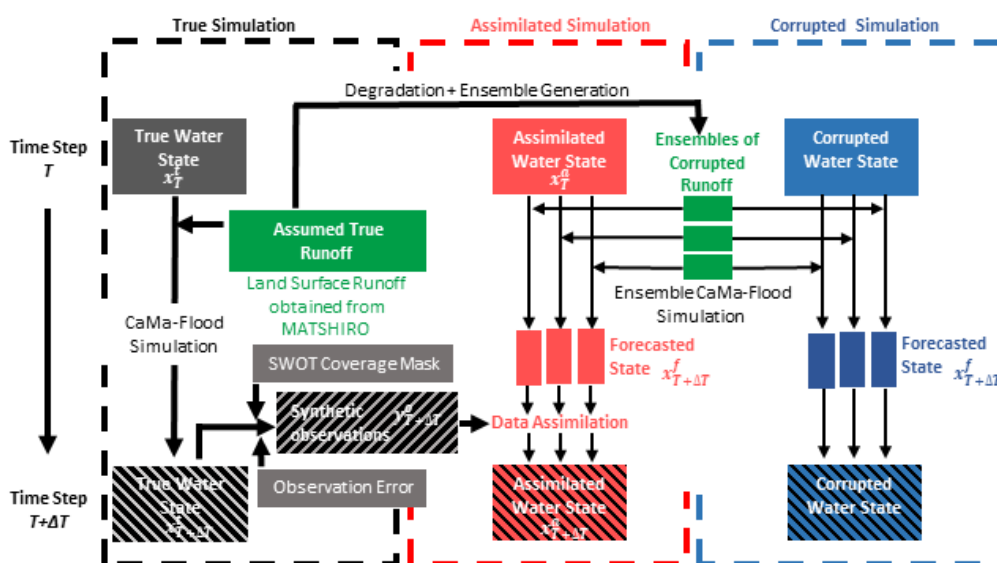


Figure 5.1: General framework of the observing system simulation experiment (OSSE)

5.2.2 Hydrodynamic model description and implementation

We used the global river hydrodynamic model CaMa-Flood (Yamazaki et al. 2011, 2012, 2013) to propagate the hydrodynamic parameters over time within our data assimilation framework. CaMa-Flood receives runoff data from a land surface model (LSM) as the input forcing (amount of water entering a river from a unit of land area in mm/day), and simulates river and floodplain hydrodynamics (i.e., river discharge, WSE, inundated area, and surface water storage) at the global scale. The spatial resolution of CaMa-Flood (set to 0.25° in this study) is coarser than that of two-dimensional flood inundation models (typically < 1 km) (e.g., Bates et al. 2010). CaMa-Flood calculates river discharge using a local inertial flow equation (a computationally efficient modification of the shallow water equation) (Bates et al. 2010; Yamazaki et al. 2013). Furthermore, the WSE values simulated using CaMa-Flood were directly comparable to WSE observations based on satellite altimetry (Yamazaki et al. 2012). Though the 0.25° (~ 25 km near the equator) resolution simulation by CaMa-Flood was applicable for large-scale rivers (Yamazaki et al. 2011, 2012), comparison between model and observation might be difficult in smaller and steep rivers. For the fully utilization of satellite altimetry, higher-resolution river model is being developed currently. Therefore, we selected CaMa-Flood as the hydrodynamic core of our data assimilation framework.

We used the runoff output from the Minimal Advanced Treatment of Surface Interaction Runoff (MATSIRO) (Takata et al. 2003) LSM as the input runoff forcing for CaMa-Flood. Previous assessments showed that river hydrodynamics were reasonably well represented by the combination of CaMa-Flood and MATSIRO runoff forcing (Yamazaki et al. 2011, 2012, 2013), supporting the use of CaMa-Flood simulations as a ‘virtual truth’ method for the data assimilation framework. For the true simulation, the runoff from MATSIRO (Kim et al. 2009) was used directly, whereas in the corrupted and assimilated simulations, the runoff forcing was intentionally modified to represent uncertainty in runoff data. We conducted the experiment over 1 year using runoff forcing from 2008. Thus, the initial conditions of the true simulation were determined from 2007 true runoff data.

We artificially corrupted the corrupted and assimilated runoff forcing by adding bias to the true runoff forcing, following previous SWOT assimilation experiments

(Andreadis et al. 2007) or by using different runoff forcing data. Thus, corrupted runoff values were generated as described in the experimental settings. Therefore, river discharge and WSE in the corrupted and assimilated simulation are contrast to those of the true simulation demonstrating different characteristics (biased, blind and different) due to corrupted runoff forcing. The initial conditions of the corrupted and assimilated simulations also were generated using corrupted runoff data.

In this study, the ensemble of model simulations was represented using multiple runoff forcing conditions. We used 20 ensembles in this study, although errors in Monte Carlo sampling decrease with increasing ensemble size (Evensen 2009). Ensemble size strongly affects the computational cost of data assimilation, as the CaMa-Flood model has a higher computational burden than other data assimilation methods. We prepared 20 different runoff forcing conditions by adding a random Gaussian noise variable to the corrupted runoff, to simulate 20 different water state forecasts in the assimilated simulation. The standard deviation of the Gaussian noise was set to 25% of the monthly mean runoff value.

Furthermore, artificially corrupted Manning's coefficients were used for the corrupted and assimilated simulations, representing errors in model parameters or formulation. In the true simulation, Manning's coefficient was determined using the original CaMa-Flood model (0.03 for river channel flow and 0.1 for floodplains). Meanwhile, for the corrupted and assimilated simulations, Manning's coefficient (river channel flow) was determined by multiplying the original Manning's coefficient by a Gaussian noise term representing a unit mean and 25% standard deviation. Hence, Manning's coefficient is distributed approximately normally over the range of 0.0225 to 0.0375 for the river channel representing the common range of Manning's coefficients in natural streams. Manning's coefficients for natural streams seems to be vary between 0.02 to 0.04 according to Chow (Chow 1959), Barnes (Barnes 1967), and Akan (Akan 2006). In addition, the error of the model should not to be very large, hence the assimilation always finds the observation is much accurate. Therefore, we select CaMa-Flood Manning's coefficient to be normally distributed between -25% to +25% of the original Manning's coefficient in assimilated and corrupted simulations.

5.2.3 Data assimilation strategy

A data assimilation scheme is typically used to estimate time-varying model state variables, e.g., hydraulic model states such as discharge or water depth. In this study, we utilized LETKF (Hunt et al. 2007; Miyoshi et al. 2007), which is a variation of the Ensemble Kalman Filter (EnKF) (Evensen 2009), an advanced Kalman filter (KF) (Kalman 1960), to assimilate WSE from SWOT observations. The computational cost of using an EnKF at the global scale can be reduced with LETKF, which enables global-scale data assimilation.

Our implementation of the data assimilation strategy involves: (1) propagation of the model state variables through time with the CaMa-Flood model, and (2) updating the state variables based on SWOT observations using LETKF. The LETKF analysis equation for the update step is:

$$X^a = X^f + E^f \left[VD^{-1}V^T(HE^f)^T(R/w)^{-1}(Y^o - HX^f) + \sqrt{(m-1)}VD^{-1/2}V^T \right], \quad \text{eq 5.1}$$

where X^a is the posterior state estimator (or assimilator); X^f is the prior state estimator (or forecast); Y^o is the observation (here, WSE); H is the observation operator, which is linearly related to the observation and the state; m is the number of ensembles; E^f is the prior state error covariance, which is obtained directly from the ensembles; R is the observation error covariance, determined from the uncertainty of the measurements; w is the weighting term for the observation localization (Miyoshi et al. 2007); and VDV^T is given by:

$$VDV^T = (m-1)I + (HE^f)^TR^{-1}HE^f, \quad \text{eq 5.2}$$

where I is the unit matrix with dimension m which is the number of ensembles. $VD^{-1}V^T$ and $VD^{-1/2}V^T$ can be calculated from the eigenvalue decomposition of VDV^T .

5.2.4 Experimental Settings

We performed two different OSSEs, namely biased, blind, and different runoff experiments. We imposed a 25% constant reduction on the input runoff forcing in the biased runoff experiment. In different runoff experiment, input runoff forcing from different LSM was used. We used input runoff forcing for a different year in the blind

Table 5.1: Summary of the Experimental Settings

<i>Experiment Name</i>	<i>Corrupted Runoff Forcing</i>	<i>Remarks</i>
<i>Biased Runoff</i>	-25% biased was added to monthly mean runoff	error percentage is constant with the time
<i>Blind Runoff</i>	runoff of the year 2004 is used for year 2008	slight difference in the magnitude but shape of the hydrograph remains the same
<i>Different Runoff</i>	Runoff of a different LSM (H08: Hanasaki et al. 2008a,b) model is used	Both magnitude and the shape of the hydrograph is different

runoff experiment. The details of the experiments are explained in following sections. Summary of the experimental settings are presented in the Table 5.1.

5.2.4.1 Biased runoff experiment

In the biased runoff experiment, we added an artificial bias to the true runoff forcing, following previous SWOT assimilation experiments (Andreadis et al. 2007) (Figure 5.2). Thus, the corrupted runoff value was generated through addition of a -25% bias to the true runoff forcing. In general, river discharge and WSE in the corrupted simulation is 25% smaller than those of the true simulation, due to the bias added to the runoff forcing. We conducted the experiment for 1 year using runoff forcing values from 2008. We generated corrupted runoff data by adding a -25% bias to the true runoff from 2008, which was used in the corrupted and assimilated simulations. The initial conditions of the true simulation were calculated using 2007 runoff data, whereas those of the corrupted and assimilated simulations were generated using -25% biased runoff data for 2007. Hence, we could identify the most useful locations and times for data assimilation in river discharge estimation.

5.2.4.2 Blind runoff experiment

In the blind runoff experiment, we constructed a relative realistic scenario for corrupted runoff by assuming variable uncertainty in the runoff forcing (Figure 5.3). In reality, accurate prediction of precipitation has limitations and the subsequent runoff generation calculation has errors that vary in both space and time. Thus, we assumed that

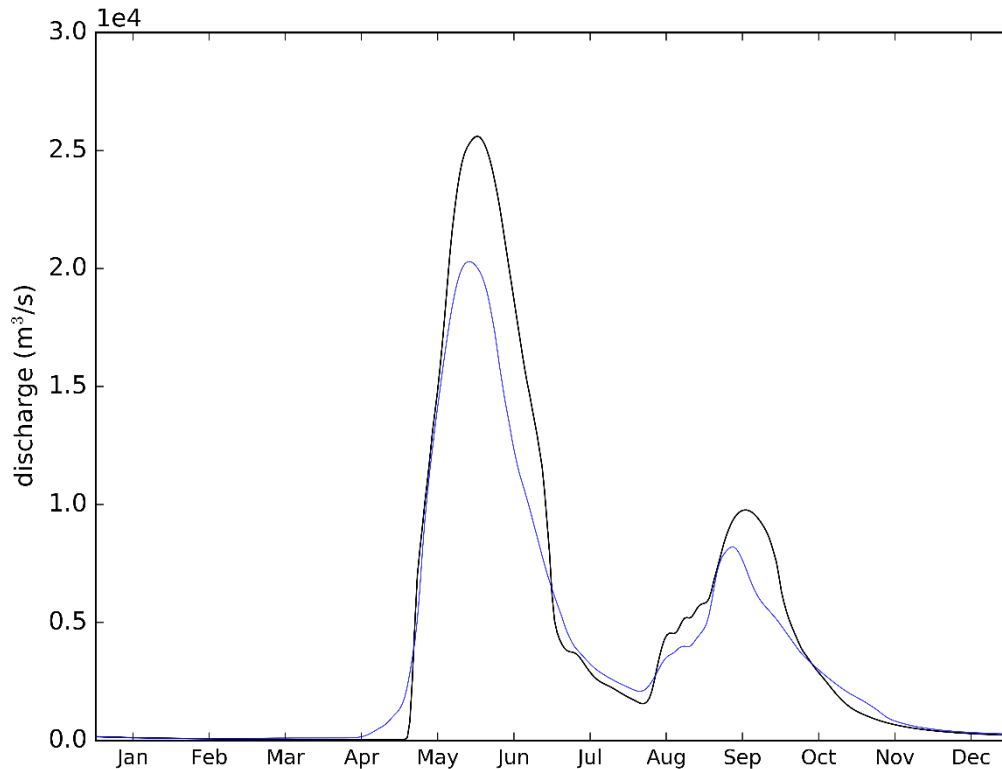


Figure 5.2: Representation of comparison of hydrograph for true (black) and corrupted (blue) for biased runoff experiment.

virtual experiments were ‘blind’ to the location and time of runoff generation in the true simulation. The blind runoff experiment was also conducted for 2008 using runoff forcing data from 2004 for the corrupted and assimilated simulations. Note that the initial water state of the corrupted and assimilation simulations in the blind runoff experiment was generated using 2003 runoff data, assuming realistic runoff data were not available for the spin-up period. Therefore, we could evaluate this effect even when realistic runoff data were not available.

5.2.4.3 Different runoff experiment

In the different runoff experiment, we constructed a more realistic scenario for corrupted runoff by assuming variable uncertainty in the runoff forcing (Figure 5.4). In reality, accurate prediction of precipitation has limitations and the subsequent runoff generation calculation has errors that vary in both space and time. Thus, we assumed that the physics of true experiments were ‘different’ to the location and time of runoff

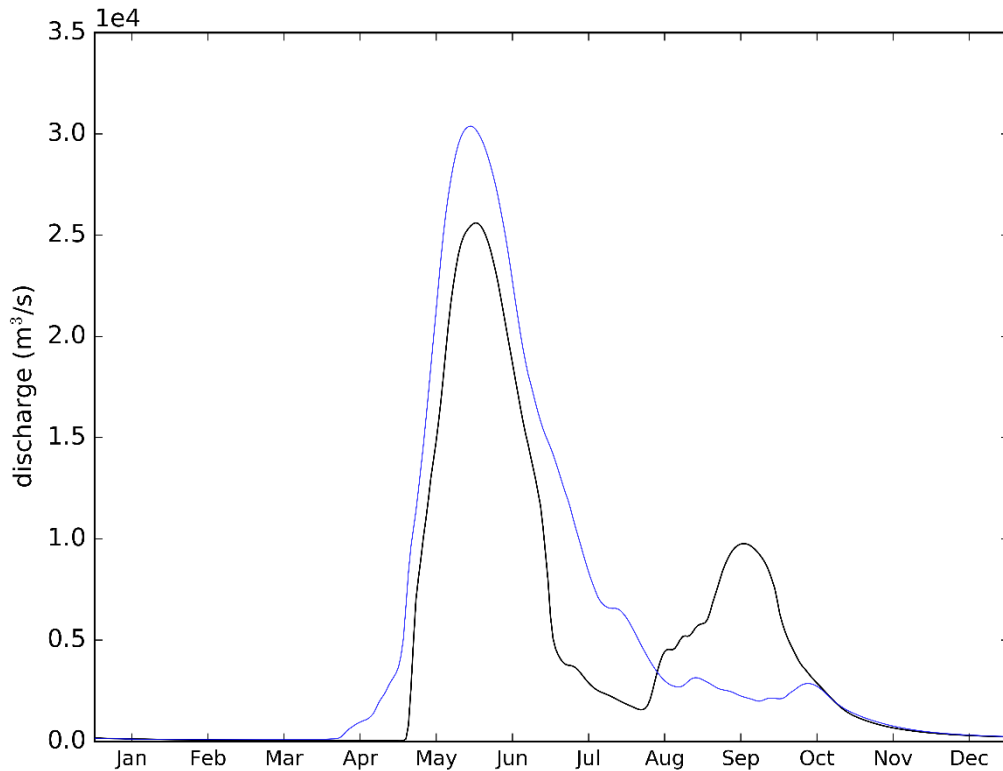


Figure 5.3 : Representation of comparison of hydrograph for true (black) and corrupted (blue) for blind runoff experiment.

generation in the true simulation. The different runoff experiment was also conducted for 2008 using runoff forcing data from a different LSM model (H08:Hanasaki et al. 2008a,b) for the corrupted and assimilated simulations. Therefore, we could evaluate this effect even when realistic runoff data were not available.

5.2.5 Evaluation method

We used the assimilation index (AI) (Ikeshima et al. 2017) to evaluate the effectiveness of data assimilation in a virtual experiment. AI is calculated from the ratio of river discharge error rates between the assimilated and corrupted simulations, using following equation:

$$AI = 1 - \left| \frac{\text{Assimilated Discharge} - \text{Corrupted Discharge}}{\text{True Discharge} - \text{Corrupted Discharge}} - 1 \right| \quad \text{eq 5.3}$$

AI describes the similarity between the assimilated and true simulations compared to the corrupted simulation. A high AI (near the maximum of 1) indicates that the

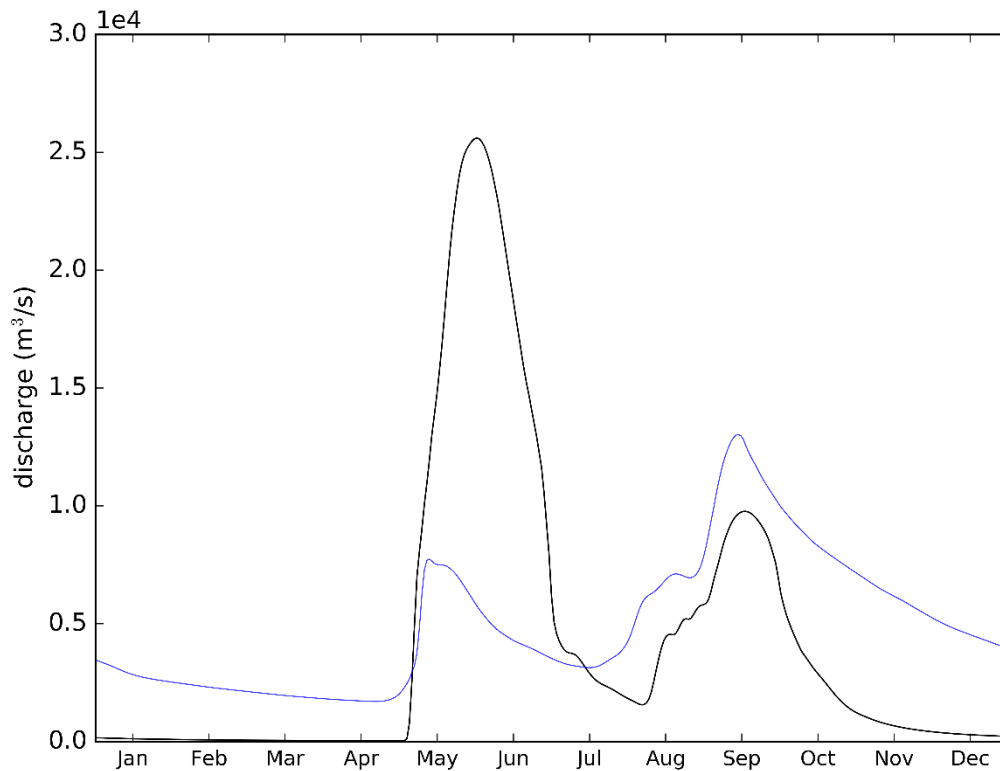


Figure 5.4 : Representation of comparison of hydrograph for true (black) and corrupted (blue) for different runoff experiment.

assimilated discharge is closer to the true discharge than to the corrupted discharge, while a low AI indicates that the assimilated discharge did not have improved accuracy over the corrupted discharge. AI is particularly useful for evaluating the effectiveness of data assimilation, as river discharge in the corrupted simulation is generally 25% lower than that of the true simulation for most places and times. AI is a metric representing the relative effectiveness of data assimilation and not a measure of simulation accuracy, such as the Nash–Sutcliffe (NS) coefficient (Nash and Sutcliffe 1970). In addition, AI can be calculated for any time and location during the experiment, enabling analysis of when and where the data assimilation framework was effective at estimating river discharge. Furthermore, we used NS to determine the degree of correction for the discharge estimate based on the assimilation.

5.3 Results

5.3.1 Biased runoff experiment

In this section, we discuss the results of the data assimilation scheme developed using empirical local patches and evaluate the potential of a future SWOT mission to estimate river discharge in a situation with 25% negatively biased runoff. A relative effect was determined using AI and NS.

5.3.1.1 Discharge estimation

Hydrographs for GRDC locations in major rivers during the simulation period (366 days) are shown in Figure 5.5. Red, blue, and black lines indicate the assimilated, corrupted and true discharge values, respectively. The green line represents AI. When the true and assimilated discharges are very similar (within 10%), we used a light green line to indicate AI. Green dots on the AI curve represent days with direct observations for the target pixel. Mean AI and percentage bias (pBias) are provided in the upper left corner for each location.

Figure 5.5a shows the hydrograph for Obidos GRDC location in Amazon basin. The assimilated discharge (red line in Figure 5.5a) and the true discharge (black line in Figure 5.5a) are similar for most of the simulation period, except for beginning for January. The mean AI (green line in Figure 5.5a) for the entire simulation period is 0.97, and AI usually stays above 0.9 for most of the simulation period. Some low AI values occurred, indicated by the light green in Figure 5.5a, in the beginning of November due to the similarity between the true and corrupted discharge values (percentage difference $< 10\%$), as explained above. Assimilation efficiency in January is strongly affected by the initial condition, which is similar to the corrupted state, and therefore more time (around 15 days) is needed to reach high AI values (> 0.8). As Amazon is very large river basin the frequency of observations higher as well as the upstream corrections propagate downwards (i.e. Obidos is in the downstream of the Amazon River).

The hydrograph of the downstream GRDC location, Kinshasa of the Congo River is presented in Figure 5.5b. The assimilated discharge (red lines in Figure 5.5b) is almost identical to the true discharge (black lines in Figure 5.5b), except in the first half of January, June, and July. In January, a significant impact was observed from the initial-

corrupted conditions, which were generated using corrupted runoff. The AI values remained above 0.8 for most of the simulation period, but reached low values around June and July (shown in light green in Figure 5.5b) when the river had low flow (dry season in the downstream Congo basin (Baker 2008)). The low AI values in June and July were caused by the small difference between the mean corrupted and true discharge values (percentage error < 10%). Average percentage bias is -0.9% indicating that the estimated river discharge after assimilation is slightly lower than the true discharge. This bias is largely due to the initial-condition state error in first half of January. Once the initial-condition state was transformed to the well-assimilated state (AI > 0.8) around mid-

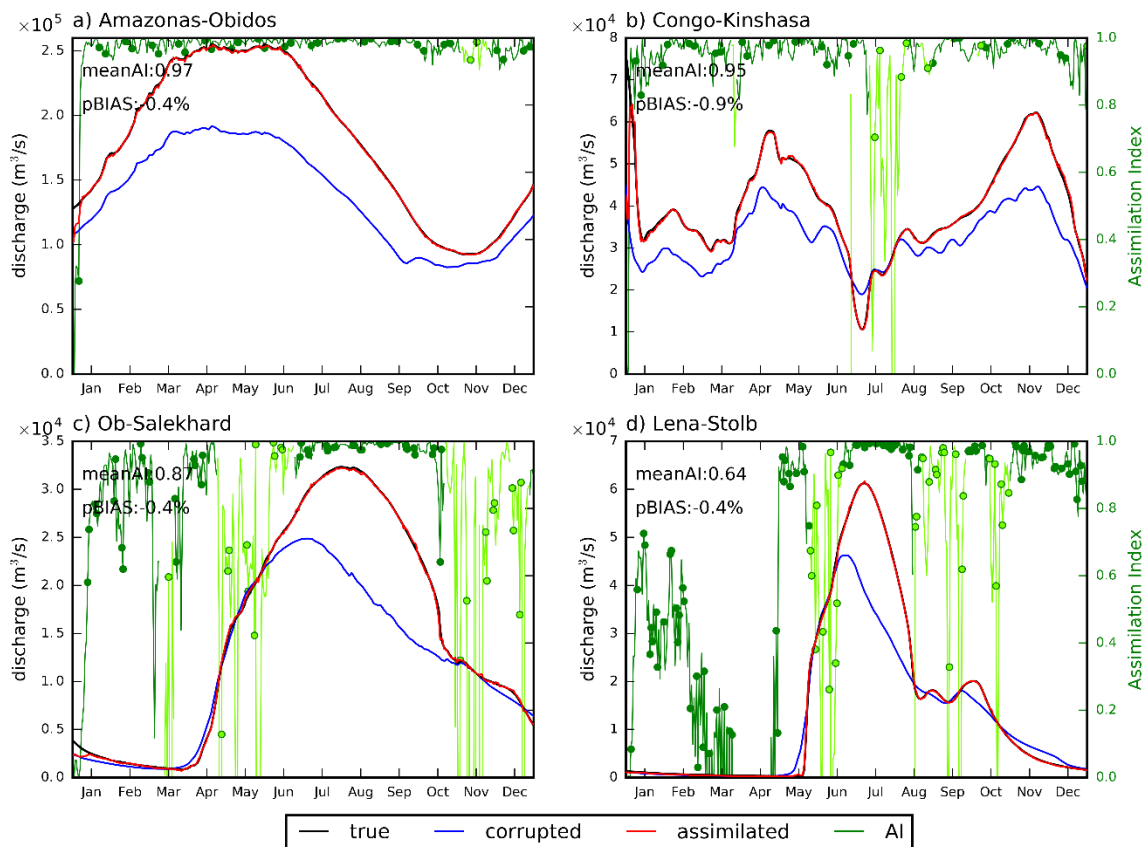


Figure 5.5: Hydrograph of the GRDC locations a) Obidos, b) Kinshasa, c) Salekhard, and d) Stolb for year 2008 in the Amazon, Congo, Ob, and Lena Rivers, respectively for biased runoff experiment. True, corrupted, and assimilated discharge values are indicated by black, blue, and red lines, respectively. The thin blue and red lines show the ensembles of corrupted and assimilated discharge, respectively. The assimilation index (AI) is shown in green, and the light green line indicates the bias of corrupted discharge relative to true discharge. Green dots represent the times of synthetic SWOT observations. The mean AI and percent bias (pBIAS) of the assimilated simulation are shown in the left corner of each hydrograph.

January, the percentage bias became very low. Hence, the AI is high and settled through most of the simulation.

Figure 5.5c presents the time variation of discharge at Salekhard GRDC location in Ob River. This location (Salekhard) has an annual mean AI of 0.87. The assimilated discharge (red line in Figure 5.5c) and the true discharge (black line in Figure 5.5c) are generally similar, but some low AI values can be observed in January, mid-March, May, November, and December. January was affected by the initial-corrupted state error, and July by the similarity of corrupted and true discharge (light green line in Figure 5.5c). Almost all other discrepancies are due to low observation frequency and distant observations. In addition, the peak was well replicated in the assimilated simulation. Thus, the assimilation efficiency is higher for most of the simulation in Salekhard GRDC location in Ob River.

Hydrograph of Stolb GRDC location of Ob River is presented in Figure 5.5d. This location demonstrates an annual mean AI of 0.64. All the significant variation of discharge was emulated well in the assimilated assimilation (red line in Figure 5.5d). The AI curve shows high fluctuations until end of April where discharge demonstrate very low values. This low AI values and fluctuations were may be due to low flow values. All the other low AI values shown in light green color, is due to small difference between the mean corrupted and true discharge values (percentage error < 10%). The peak discharge, troughs, and time to peak discharge were well represented in assimilated simulation. Therefore, the discharge is well estimated in Stolb GRDC location of Ob River.

5.3.1.2 Global assimilation efficiency

Figure 5.7 shows the global annual mean AI for biased runoff experiment. Most of the continental-scale rivers were well assimilated. At most downstream locations, mean AI was greater than 0.8, indicating good assimilation using our derived assimilation scheme. Upstream river reaches at higher latitudes were also well assimilated ($AI > 0.8$), but those at lower latitudes had AI values of 0.3–0.8. For most downstream river stems and rivers at higher latitudes, assimilation of SWOT observations was effective at improving river discharge estimation, even when runoff data were constantly biased.

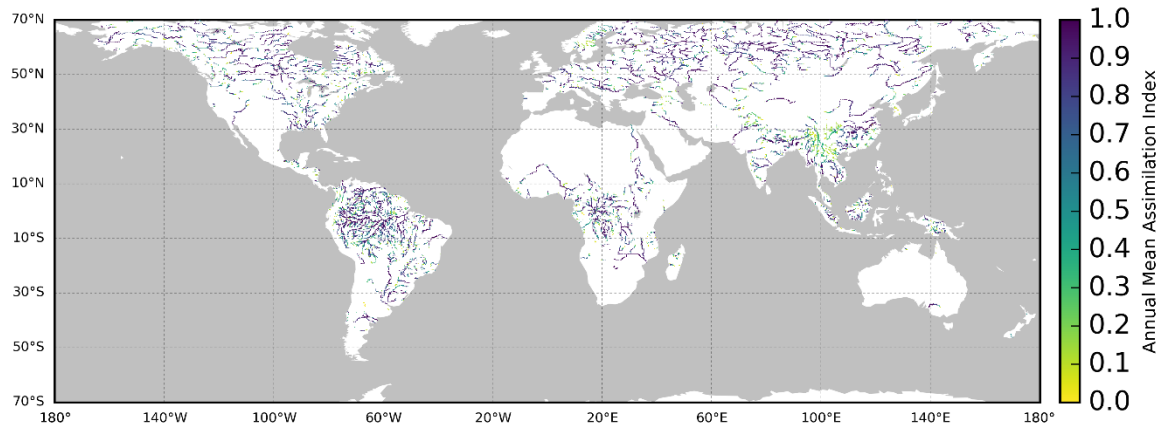


Figure 5.7 : Global annual mean AI for biased runoff experiment. Pixels $> 500 \text{ m}^3/\text{s}$ presented for visualization purposes.

Rivers located at high latitudes as well as low latitudes had high AIs even at upstream locations, disregarding the variation of observation frequency depend on the latitudes. There were more than four observations available within the 21-day orbital cycle at latitudes $> 50^\circ\text{N}$, whereas lower-latitude regions had only one or two. High-

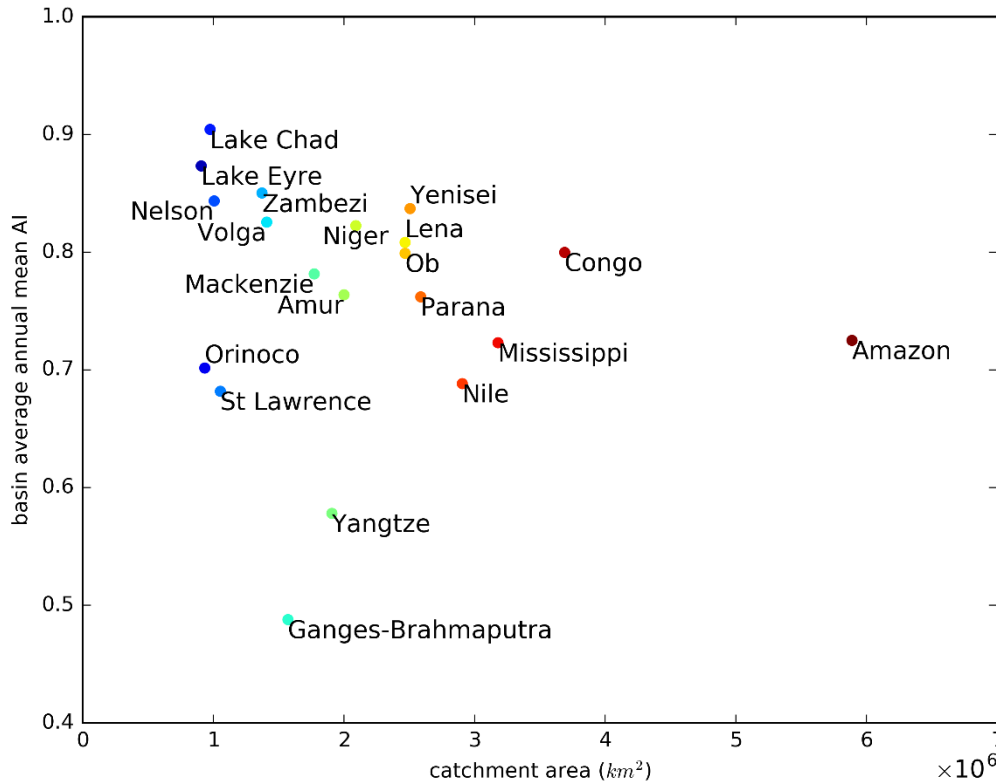


Figure 5.6: Basin average annual mean AI with the catchment area of the basin for 20 largest basins in the world for biased runoff experiment.

frequency SWOT observations and their associated corrections allowed the AI to be maintained at a high value, which resulted in a high mean AI in higher latitude rivers. Rivers in high-latitude regions (e.g., the Ob and Lena Rivers; Figure 5.5c and d) had high mean AIs. At the downstream Lena River (Figure 5.5d), AI remained high, even on days with no local observations, except for days when the corrupted and true discharge were close (days with light green lines in Figure 5.5d). Even on low latitudes AI remain high on days with no local observations at the downstream Congo River. Even though there are differences in the numbers of total observations (Lena: 69 times/year, Congo: 35 times/year) did not cause difference in assimilation effectiveness due to the Empirical local patch. Therefore using Figure 5.6 illustrates the relationship between the upstream drainage areas and basin average annual mean AI for 20 largest river basins. Basins with larger drainage areas had higher basin average annual mean AI because more SWOT observations were available as the drainage area increased. Rivers at high latitudes (e.g. Yenisei, Ob, Lena) had slightly higher AIs than similar-sized rivers at lower latitudes (e.g. Nile and Parana). This tendency of AI is also related to the number of available SWOT observations, because higher-latitude rivers had more SWOT observations due to the orbital characteristics. Hence, there is a trade-off between catchment size and the location of the river basin.

5.3.1.3 Model Efficiency

In this section, we explain the results for model efficiency with and without data assimilation using the empirical local patch. Figure 5.8 presents the spatial distribution of the NS coefficient (Nash and Sutcliffe 1970) of discharge using the empirical local patch on biased runoff experiment. The NS coefficients for the assimilated and corrupted simulations, and the difference in the NS coefficient between them, are presented in Figure 5.8a–c. As the NS coefficient is a measure of model efficiency, we use it to evaluate the efficiency of simulation with assimilation (assimilated simulation) and without assimilation (corrupted simulation). The NS coefficient of the assimilated simulation is very close to 1, indicating high efficiency (Figure 5.8a), with a few upstream sites showing relatively low values (around 0.8). On the other hand, NS coefficients of the corrupted simulation have values around 0.7–0.9 due to degradation of the runoff forcing (Figure 5.8b). Interestingly, the NS coefficient of the corrupted simulation for the

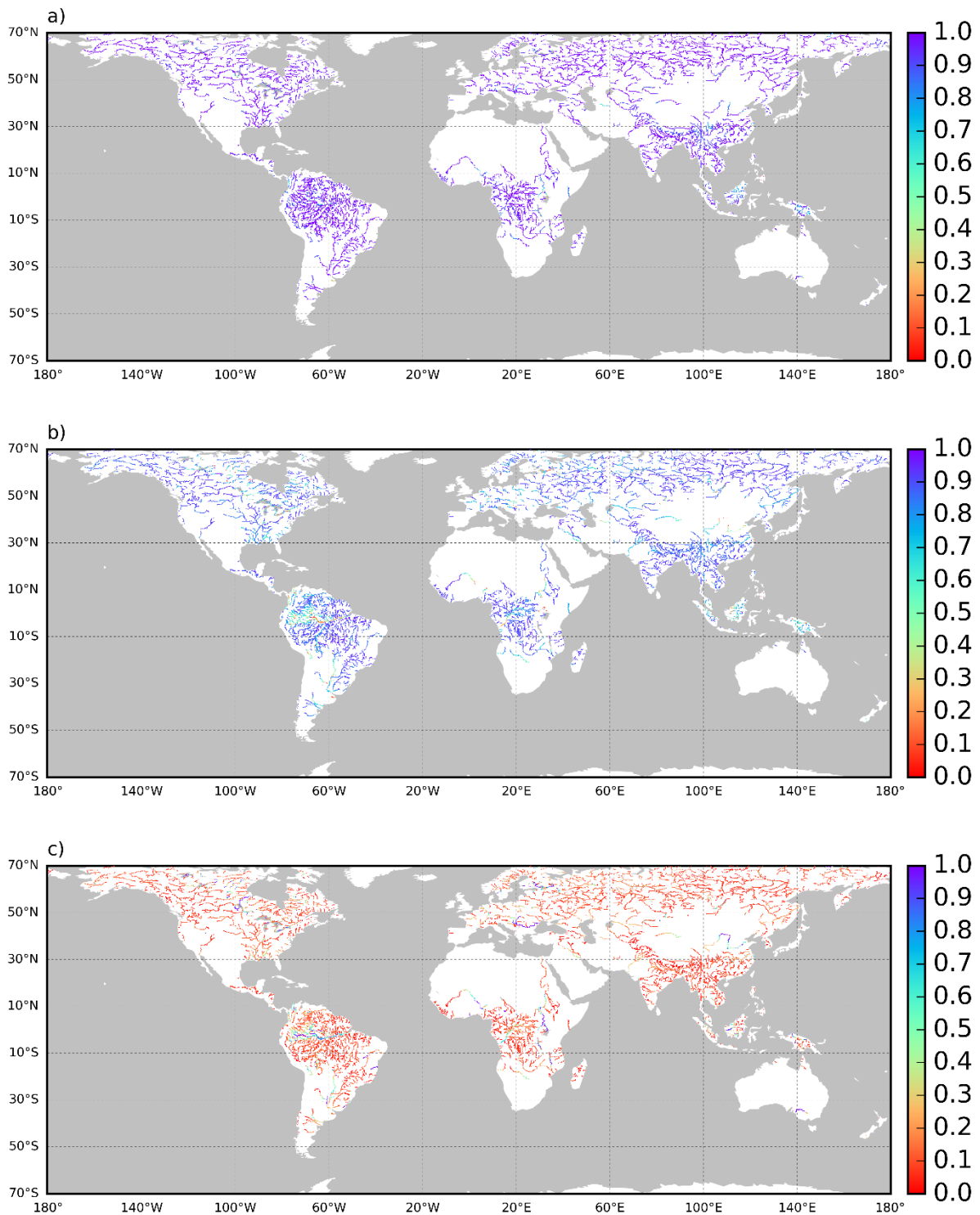


Figure 5.8 : Nash-Sutcliffe (NS) coefficient for model efficiency with a) assimilated discharge, b) corrupted discharge, and c) the difference between assimilated and corrupted discharge for biased runoff experiment. Discharge values $> 500 \text{ m}^3/\text{s}$ are presented for visualization purposes.

main stem of large river basins (Amazon and Congo) shows relatively low values,

indicating importance of the assimilation on the continental-scale river streams. Furthermore, the difference in NS (Figure 5.8c) supports the low efficiencies we detected, shown in Figure 5.8b. In most sites, the difference of NS was < 0.1 (difference in NS coefficients between assimilated and corrupted discharge) except for the main stems (0.2–0.7). The assimilated simulation had much better model efficiency compared to the corrupted simulation, especially for most downstream sites of the continental-scale rivers, which have large discharges. Thus, this assimilation scheme can be used to estimate river discharge well, even when the input forcing and model parameters result in low modeling efficiency ($NS \approx 0.3$).

5.3.2 Blind runoff experiment

In this section, we discuss the results of the data assimilation evaluate the potential of a future SWOT mission to estimate river discharge where different year's runoff forcing is used (blind runoff experiment). A relative effect was determined using AI and NS.

5.3.2.1 Discharge estimation

Hydrographs for GRDC locations in major rivers during the simulation period (366 days) are shown in Figure 5.9. Red, blue, and black lines indicate the assimilated, corrupted and true discharge values, respectively. The green line represents AI. When the true and assimilated discharges are very similar (within 10%), we used a light green line to indicate AI. Green dots on the AI curve represent days with direct observations for the target pixel. Mean AI and percentage bias (pBias) are provided in the upper left corner for each location.

Figure 5.9a shows the hydrograph for Obidos GRDC location in Amazon basin. The assimilated discharge (red line in Figure 5.9a) is closer to the true discharge (black line in Figure 5.9a) most of the simulation period (slightly higher) than the corrupted discharge. The mean AI (green line in Figure 5.9a) for the entire simulation period is 0.53, and AI fluctuated between 0.8 and 0 for most of the simulation period. The time to peak discharge is well assimilated but the peak discharge is slightly higher than true discharge. Even though the peak discharges were overestimated, timing of low flow and the magnitude of low flow was recreated well in the assimilated simulation compared to

corrupted simulation. Some low AI values occurred, in July, August, and September where corrupted discharge is closer to true discharge than assimilated discharge. These discrepancies may be due to assimilation of distant observations from the target pixel. Assimilation efficiency in January is strongly affected by the initial condition, which is similar to the corrupted state.

The hydrograph of the downstream GRDC location, Kinshasa of the Congo River is presented in Figure 5.9b. The assimilated discharge (red lines in Figure 5.9b) is closer to the true discharge (black lines in Figure 5.9b). In January, a significant impact was observed from the initial-corrupted conditions, which were generated using corrupted

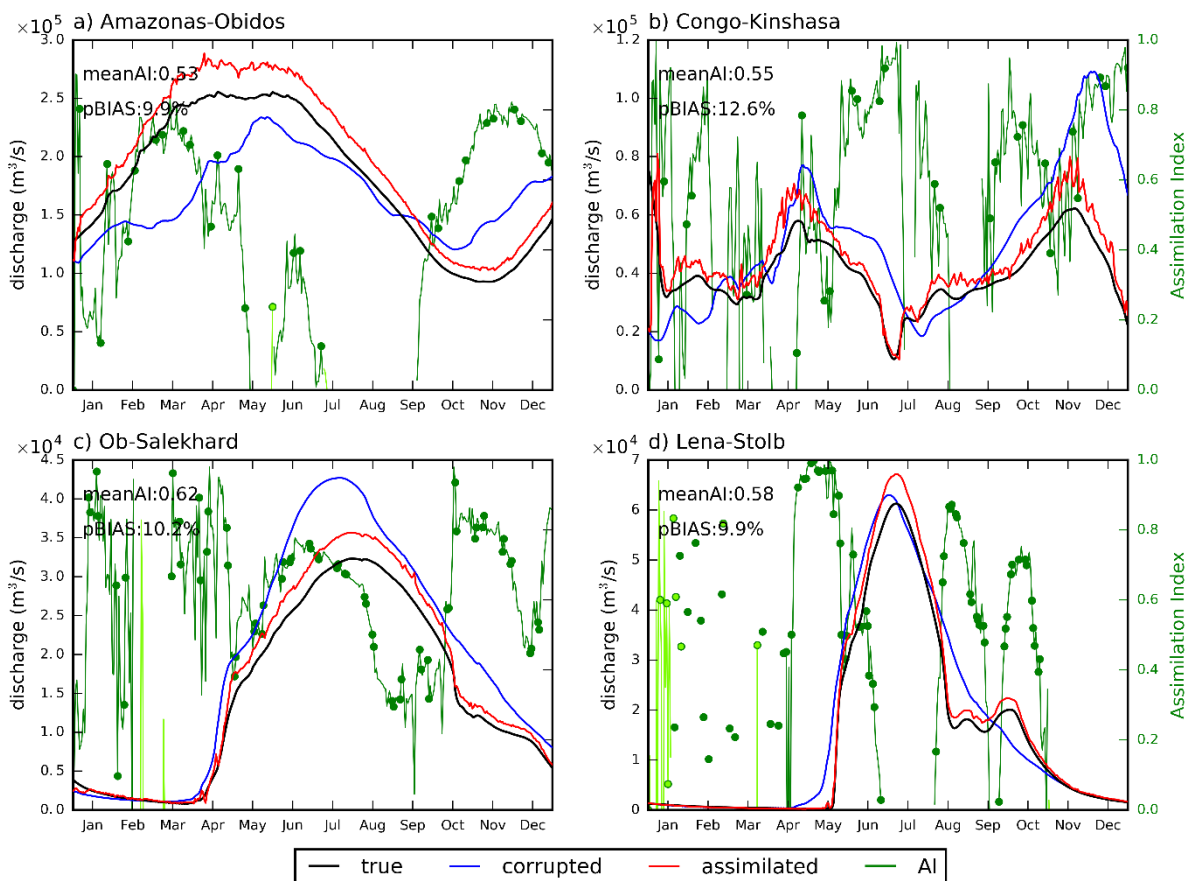


Figure 5.9 : Hydrograph of the GRDC locations a) Obidos, b) Kinshasa, c) Salekhard, and d) Stolb for year 2008 in the Amazon, Congo, Ob, and Lena Rivers, respectively for blind runoff experiment. True, corrupted, and assimilated discharge values are indicated by black, blue, and red lines, respectively. The thin blue and red lines show the ensembles of corrupted and assimilated discharge, respectively. The assimilation index (AI) is shown in green, and the light green line indicates the bias of corrupted discharge relative to true discharge. Green dots represent the times of synthetic SWOT observations. The mean AI and percent bias (pBias) of the assimilated simulation are shown in the left corner of each hydrograph.

runoff. The AI values remained above 0.6 for most of the simulation period, but reached low values around April and August. The assimilation discharge shows peaks and troughs are well assimilated compared to corrupted discharge. The low AI values in April and August were caused by the small difference between the mean corrupted and true discharge values (percentage error < 10%). Average percentage bias is 12.6% indicating that the estimated river discharge after assimilation is slightly higher than the true discharge.

Figure 5.9c presents the time variation of discharge at Salekhard GRDC location in Ob River. This location (Salekhard) has an annual mean AI of 0.62. The assimilated discharge (red line in Figure 5.9c) and the true discharge (black line in Figure 5.9c) are generally similar, but some low AI values can be observed in January and September. January was affected by the initial-corrupted state error, and July by the similarity of corrupted and true discharge (light green line in Figure 5.9c). In addition, the peak was well replicated in the assimilated simulation. Thus, the assimilation efficiency is higher for most of the simulation in Salekhard GRDC location in Ob River.

Hydrograph of Stolb GRDC location of Ob River is presented in Figure 5.9d. This location demonstrates an annual mean AI of 0.58. All the significant variation of discharge was emulated well in the assimilated assimilation (red line in Figure 5.9d). The AI curve shows high fluctuations until end of April where discharge demonstrate very low values. This low AI values and fluctuations were may be due to low flow values. The peak discharge, troughs, and time to peak discharge were well represented in assimilated simulation. Therefore, the discharge is well estimated in Stolb GRDC location of Ob River.

5.3.2.2 Global assimilation efficiency

Figure 5.10 shows the global annual mean AI for blind runoff experiment. Most of the continental-scale rivers were moderately assimilated (AI > 0.6). At most downstream locations, mean AI was greater than 0.8, indicating good assimilation using our derived assimilation scheme. Upstream river reaches at higher latitudes were also well assimilated (AI > 0.8), but those at lower latitudes had AI values of 0.3–0.8. For most downstream river stems and rivers at higher latitudes, assimilation of SWOT observations

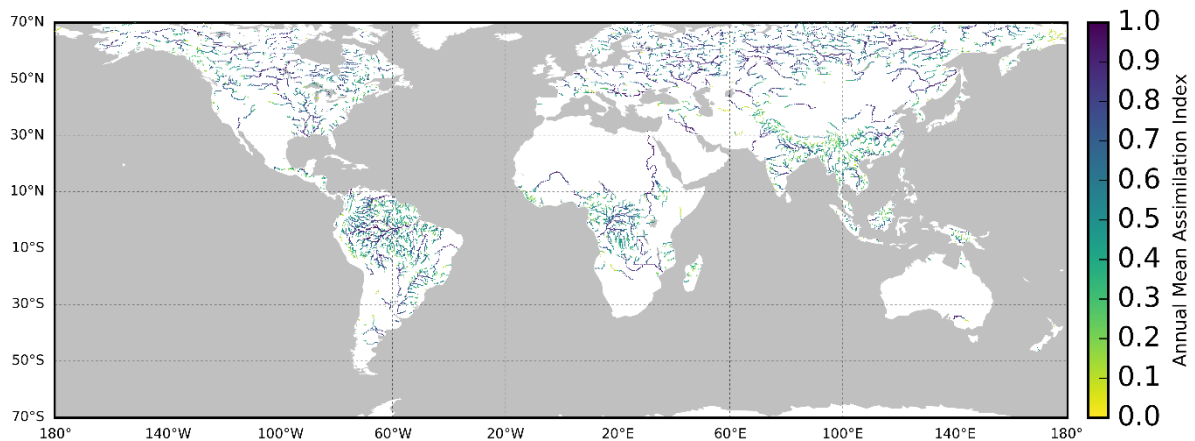


Figure 5.10 : Global annual mean AI for blind runoff experiment. Pixels $> 500 \text{ m}^3/\text{s}$ presented for visualization purposes.

was effective at improving river discharge estimation, even when true runoff data were not available.

Despite the observation frequency due to the SWOT satellite path the mean annual AI remain relatively high values. But the annual mean AI of the blind runoff experiment is around 1 unity lower than that of the biased runoff experiment. Downstream sections of the large continental-scale rivers in low latitudes and rivers in the high latitudes are well assimilated but the low latitude upstream seems to demonstrate low annual mean AI values.

Similar to the result of the biased runoff experiment, in most large-scale rivers, AI was high at downstream locations and low at upstream locations. From the overall global result, the AI was globally smaller than in the biased runoff experiment. AI is an index which is originally made to evaluate the effectiveness of data assimilation when true and corrupted simulation has large biased difference such as in biased runoff experiment. The blind runoff experiment had less biased difference and rather had random error, since we corrupted the simulation using the runoff forcing of different year instead of putting bias on the runoff. The bias between the true and corrupted discharge being small, the AI become lower, although we calculated the AI excluding the days when error between discharges are small ($< 5\%$). This randomly fluctuating error also made the assimilation difficult, since the daily trend of discharge may be completely different (i.e. daily variation of discharge increasing or decreasing does not match between the 2

simulations). Taking this into account, assimilation in this experiment was done reasonably well that most downstream or midstream locations had large AI (>0.6), or the discharge of assimilated simulation mostly matches that of corrupted simulation.

Some locations had a significantly low assimilation results compared to the biased runoff experiment. At Obidos in Amazon (Figure 5.9a), Kinshasa in Congo (Figure 5.9b), Salekhard in Ob (Figure 5.9c), and Stolb in Lena (Figure 5.9d), discharge of assimilated simulation usually had a similar trend as that of true simulation. However, there was some overestimation of discharge of assimilated simulation in rising limb of the hydrograph and the error between the true and assimilated simulation got unreasonably high. This can be explained by following; 1) the difference between corrupted and true runoff is too large. In blind runoff experiment, since we used completely different runoff data for forcing input of the model (runoff data of 2008 for true simulation and 2004 for corrupted/assimilated simulation), discharge of assimilated simulation can easily depart from that of true simulation, especially when there are no direct observations. This is not significant at downstream locations where water states are relatively stable, but at locations where rapid change of water state is large, daily variation of discharge cannot be detected. This denotes that even when observation and very optimistically accurate river model SWOT is available, we still need a good quality land surface runoff data, which is equivalent to having a good land surface model and rainfall observation. 2) Incorrect assimilation due to unreasonably large correlations between pixels in the local patch. In the developed data assimilation method, we used empirical local patch. Therefore, the local patch may contain pixels that have small relationship, such as pixels in a same elevation. However, when covariance between pixels became large, such pixels can be detected as highly correlated incorrectly. This cause introducing incorrect observation information to the data assimilation and introduce errors to the assimilation. This assumed to be happening sometimes in the blind runoff experiment that the WSE of assimilated simulation is jumping away from that of true simulation although the variance of ensemble members decreases.

Also, Salekhard (downstream) in Ob (Figure 5.9c) had a large bias error at the high-water season, although the WSE was assimilated well and had almost no error. This was because the manning coefficient was different between true and corrupted/assimilated simulation. In the developed data assimilation framework, the

manning coefficient was set to 0.030 at true simulation, while it was randomly selected at corrupted/assimilated simulation. In the CaMa-Flood, the river discharge is calculated with the local inertial equation (Yamazaki et al. 2011, 2012; Bates et al. 2010). When the manning coefficient becomes smaller, the river discharge would become larger. Therefore, in the assimilated simulation, when the WSE is corrected to the same value as that of true simulation, the river discharge would become larger than the true simulation.

To verify this effect of manning coefficient, we did the blind runoff experiment again without corrupted manning coefficient. Figure 5.11 is the resulted hydrograph of the GRDC locations Obidos in the Amazon River, Kinshasa in the Congo River,

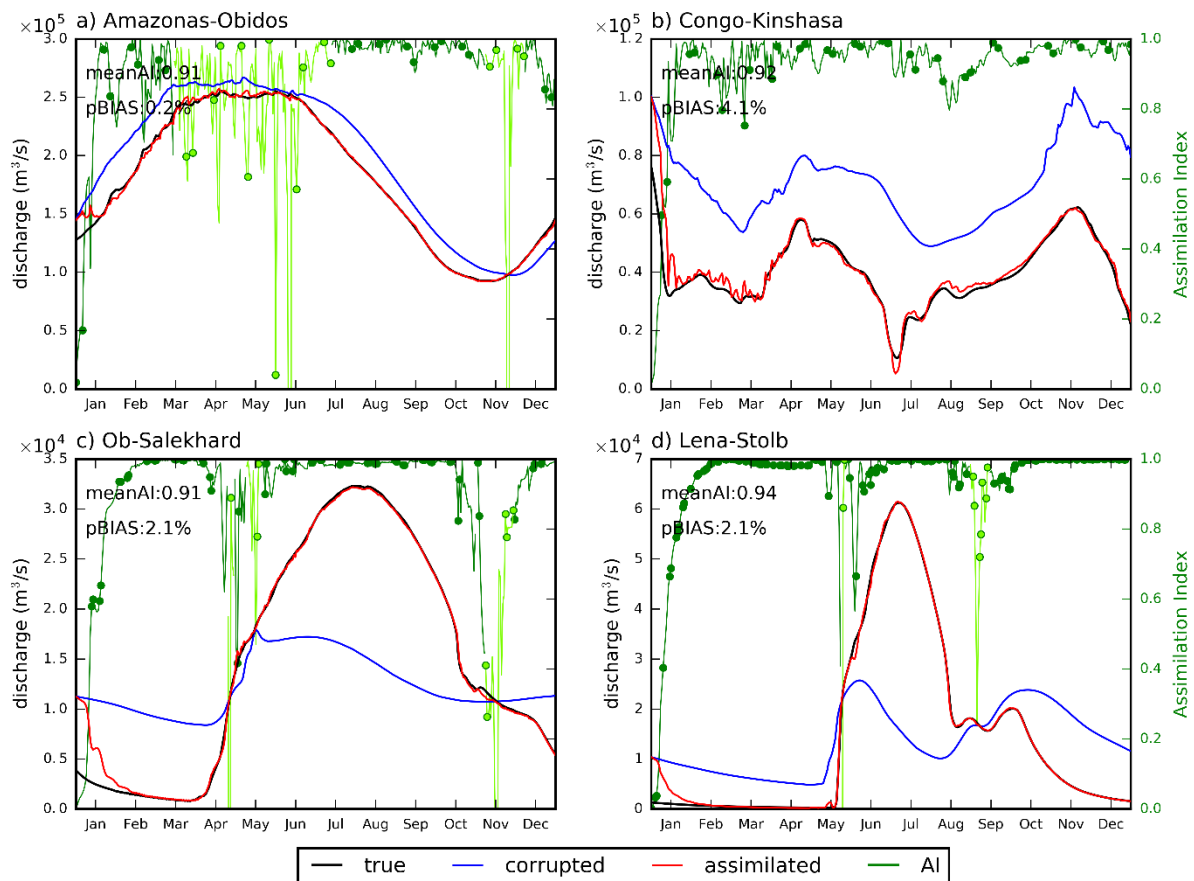


Figure 5.11: Hydrograph of the GRDC locations a) Obidos, b) Kinshasa, c) Salekhard, and d) Stolb for year 2008 in the Amazon, Congo, Ob, and Lena Rivers, respectively for blind runoff experiment without Manning's coefficient error. True, corrupted, and assimilated discharge values are indicated by black, blue, and red lines, respectively. The thin blue and red lines show the ensembles of corrupted and assimilated discharge, respectively. The assimilation index (AI) is shown in green, and the light green line indicates the bias of corrupted discharge relative to true discharge. Green dots represent the times of synthetic SWOT observations. The mean AI and percent bias (pBias) of the assimilated simulation are shown in the left corner of each hydrograph.

Salekhard in the Ob River, and Stolb in the Lena River for year 2008. In this experiment without Manning's coefficient error, presents very high annual mean AI values ($AI > 0.9$). Here, the manning coefficient of the discharge at those points were 0.003 at true simulation, larger than the corrupted/assimilated simulation (i.e. corrupted/assimilated simulation had smaller mean manning coefficient 0.0028). The discharge of assimilated simulation became slightly larger than the true simulation in the experiment with the Manning's coefficient error, which matches the provides evident to the above theory. This biased error in river discharges eminent in large river basins; such as Amazon river. However, the biased error is an important problem to be solved since it may reduce the benefit of SWOT observation. Further studies of correcting geographical parameters (i.e. Manning's coefficient) must be done to establish the correcting method in a global scale.

5.3.2.3 Model Efficiency

In this section, we explain the results for model efficiency with and without data assimilation using the empirical local patch. The Nash–Sutcliffe coefficients (NS) was additionally calculated for evaluating the result of blind runoff experiment, because unlike the biased runoff experiment, the simulation results of corrupted and true simulations could be sometime similar and AI was not reasonably calculated in such cases. Figure 5.12 presents the spatial distribution of the NS coefficient for the blind runoff experiment. NS of river discharge at assimilated simulation (Figure 5.12a), corrupted simulation (Figure 5.12b), and the relative difference between two simulations.

Similar to the result of AI (Figure 5.10), the NS in the assimilated simulation was large at midstream and downstream locations of the large-scale rivers. Although the upstream locations had a small NS value, the value rises in the downstream and it becomes almost 1.0 in the downstream. This denotes that data assimilation of SWOT observation has the potential to correct the simulation even when the model has inaccurate estimation of geographical parameters (Manning's coefficient) and/or has no accurate runoff data of current year. However, two important characteristics of this result must be pointed out: 1) Some locations near river mouth or in the high latitude region already had a high NS value in the corrupted simulation (Figure 5.12b). This is because the NS evaluates the prediction power of model, by focusing on seasonal variation. NS compares the daily error of model discharge, to the difference between daily true discharge and

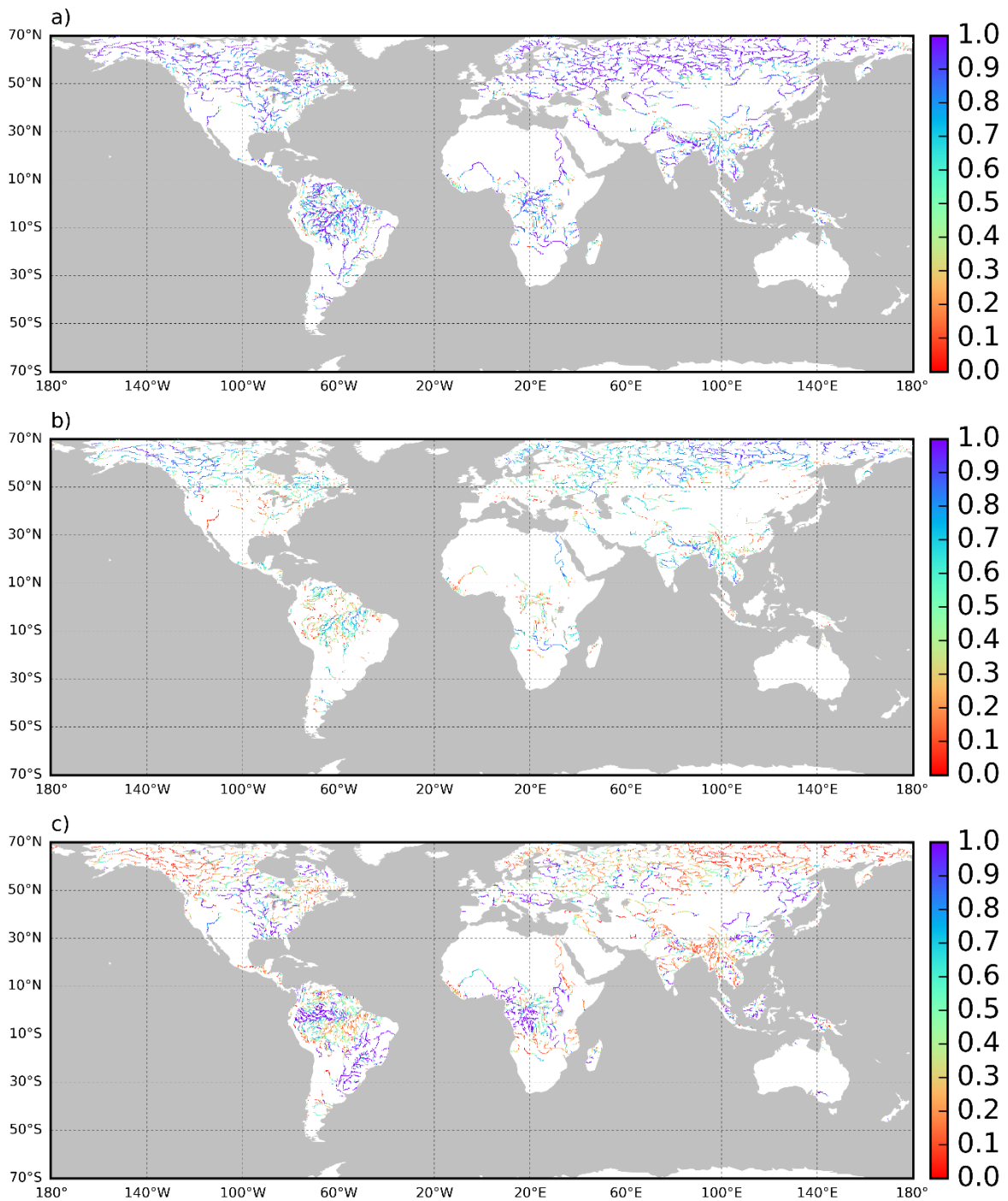


Figure 5.12 : Nash-Sutcliffe (NS) coefficient for model efficiency with a) assimilated discharge, b) corrupted discharge, and c) the difference between assimilated and corrupted discharge. Discharge values $> 500 \text{ m}^3/\text{s}$ are presented for visualization purposes.

annual average true discharge. This results NS to focus on seasonal error instead of daily discharge error. NS was able to become high at locations such as river mouths or high

latitude regions, because those locations tend to have similar seasonal trend (i.e. high-water season happened in the same time) between true and assimilated/corrupted simulation, or have a long period when seasonal trend is almost the same (i.e. discharge at winter season was almost same). 2) The NS calculated here may be optimistic, since we calculated them as the difference between simulations using same core river model. Usually, NS is calculated to evaluate the model prediction against the true state (i.e. actual observation). Here, the only difference at the core river model is that they have a different Manning coefficient. Therefore, the high NS here only means how the data assimilation can benefit the model, with the assumption that core river model has the correct water physics and river routing system. From the Figure 5.12c, relative difference of NS was near 1.0 at most locations, data assimilation can be said very effective under such assumptions. To make data assimilation effective under the real operation of SWOT satellite, river model uncertainties must be decreased.

5.3.3 Different runoff experiment

In this section, we discuss the results of the data assimilation scheme developed using empirical local patches and evaluate the potential of a future SWOT mission to estimate river discharge where different runoff forcing is used (different runoff experiment). A relative effect was determined using AI and NS.

5.3.3.1 Discharge estimation

Hydrographs for GRDC locations in major rivers during the simulation period (366 days) are shown in Figure 5.13. Red, blue, and black lines indicate the assimilated, corrupted and true discharge values, respectively. The green line represents AI. When the true and assimilated discharges are very similar (within 10%), we used a light green line to indicate AI. Green dots on the AI curve represent days with direct observations for the target pixel. Mean AI and percentage bias (pBias) are provided in the upper left corner for each location.

Figure 5.13a shows the hydrograph for Obidos GRDC location in Amazon basin. The assimilated discharge (red line in Figure 5.13a) is slight biased to the true discharge (black line in Figure 5.13a) most of the simulation period (slightly higher) than the corrupted discharge. The mean AI (green line in Figure 5.13a) for the entire simulation

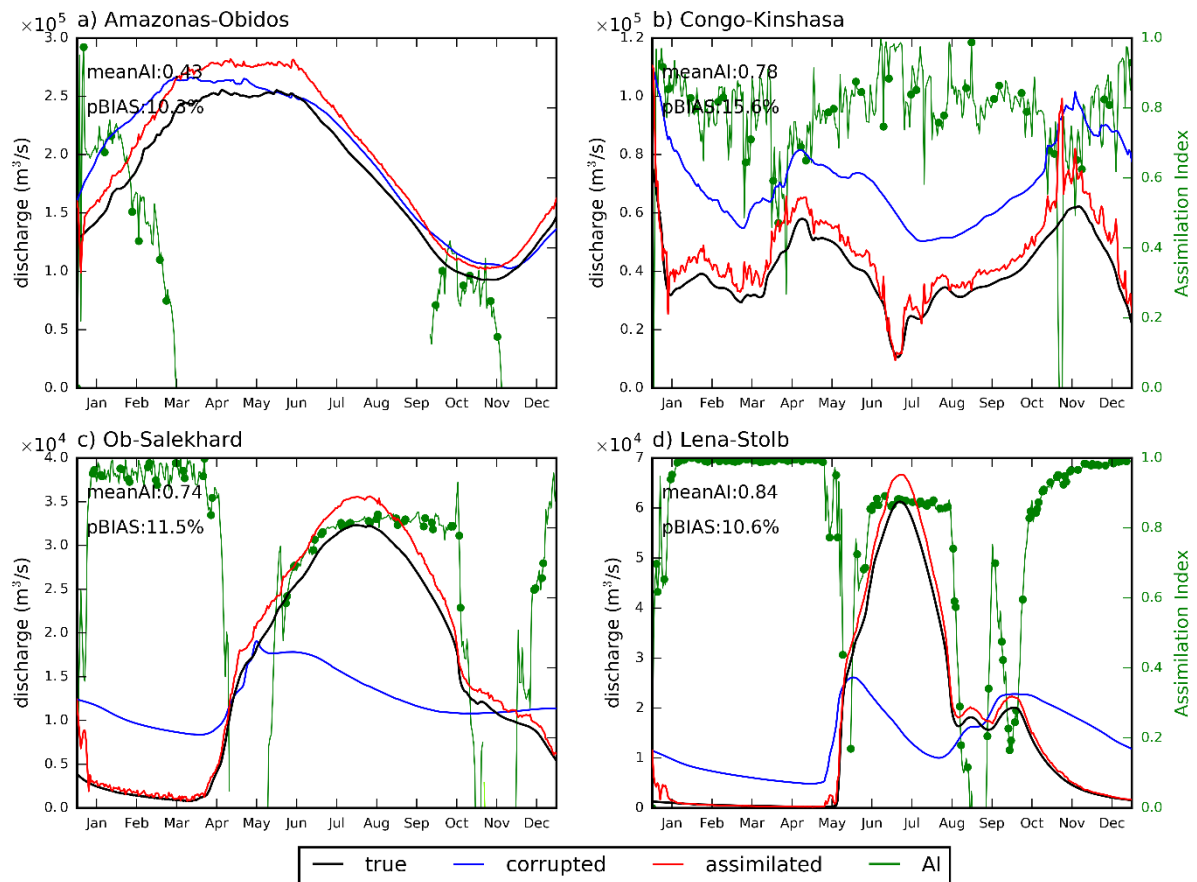


Figure 5.13 : Hydrograph of the GRDC locations a) Obidos, b) Kinshasa, c) Salekhard, and d) Stolb for year 2008 in the Amazon, Congo, Ob, and Lena Rivers, respectively. True, corrupted, and assimilated discharge values are indicated by black, blue, and red lines, respectively for different runoff experiment. The thin blue and red lines show the ensembles of corrupted and assimilated discharge, respectively. The assimilation index (AI) is shown in green, and the light green line indicates the bias of corrupted discharge relative to true discharge. Green dots represent the times of synthetic SWOT observations. The mean AI and percent bias (pBias) of the assimilated simulation are shown in the left corner of each hydrograph.

period is 0.43, and AI fluctuated between 0.8 and 0 for most of the simulation period. The time to peak discharge is well assimilated but the peak discharge is slightly higher than true discharge. According to the blind runoff experiment without Manning's coefficient, is due to the error in Manning's coefficient causes higher discharge when calculate using simplified St. Venant momentum equation (Yamazaki et al. 2011). Even though the peak discharges were overestimated, timing of low flow and the magnitude of low flow was recreated well in the assimilated simulation compared to corrupted simulation. Some low AI values occurred, in July, August, and September where corrupted discharge is closer to true discharge than assimilated discharge.

The hydrograph of the downstream GRDC location, Kinshasa of the Congo River is presented in Figure 5.13b. The assimilated discharge (red lines in Figure 5.13b) is closer to the true discharge (black lines in Figure 5.13b). In January, a significant impact was observed from the initial-corrupted conditions, which were generated using corrupted runoff. The AI values remained above 0.6 for most of the simulation period, but reached low values beginning of November. The assimilation discharge shows peaks and troughs are well assimilated compared to corrupted discharge. Average percentage bias is 15.6% indicating that the estimated river discharge after assimilation is slightly higher than the true discharge.

Figure 5.13c presents the time variation of discharge at Salekhard GRDC location in Ob River. This location (Salekhard) has an annual mean AI of 0.74. The assimilated discharge (red line in Figure 5.13c) and the true discharge (black line in Figure 5.13c) are generally similar, but some low AI values can be observed in January. January was affected by the initial-corrupted state error. In addition, the peak was well replicated in the assimilated simulation. Thus, the assimilation efficiency is higher for most of the simulation in Salekhard GRDC location in Ob River.

Hydrograph of Stolb GRDC location of Ob River is presented in Figure 5.13d. This location demonstrates an annual mean AI of 0.84. All the significant variation of discharge was emulated well in the assimilated assimilation (red line in Figure 5.13d). The AI curve shows high fluctuations until end of April where discharge demonstrate very low values. This low AI values and fluctuations were may be due to low flow values. The peak discharge, troughs, and time to peak discharge were well represented in assimilated simulation. Therefore, the discharge is well estimated in Stolb GRDC location of Ob River.

5.3.3.2 Global assimilation efficiency

Figure 5.14 shows the global annual mean AI for blind runoff experiment. Most of the continental-scale rivers were moderately assimilated ($AI > 0.6$). At most downstream locations, mean AI was greater than 0.8, indicating good assimilation using our derived assimilation scheme. Upstream river reaches at higher latitudes were also well assimilated ($AI > 0.8$), but those at lower latitudes had AI values of 0.3–0.8. For most downstream river stems and rivers at higher latitudes, assimilation of SWOT observations

was effective at improving river discharge estimation, even when true runoff data were not available.

Despite the observation frequency due to the SWOT satellite path the mean annual AI remain relatively high values. But the annual mean AI of the blind runoff experiment is around 1 unity lower than that of the biased runoff experiment. Downstream sections of the large continental-scale rivers in low latitudes and rivers in the high latitudes are well assimilated but the low latitude upstream seems to demonstrate low annual mean AI values.

Similar to the result of the biased runoff experiment, in most large-scale rivers, AI was high at downstream locations and low at upstream locations. From the overall global result, the AI was globally smaller than in the biased runoff experiment. AI is an index which is originally made to evaluate the effectiveness of data assimilation when true and corrupted simulation has large biased difference such as in biased runoff experiment. The difference runoff experiment had variable bias both spatially, and temporally and rather had random error, since we are using the runoff forcing from different LSM instead of adding a constant bias on the runoff. The bias between the true and corrupted discharge being small, the AI become lower, although we calculated the AI excluding the days when error between discharges are small ($< 5\%$). As the corrupted runoff forcing vary according to the place, some places have very small error relative to true runoff forcing, and vice-versa. Therefore, error caused by the Manning's coefficient is larger than the runoff forcing error, some place has large error in discharge estimation

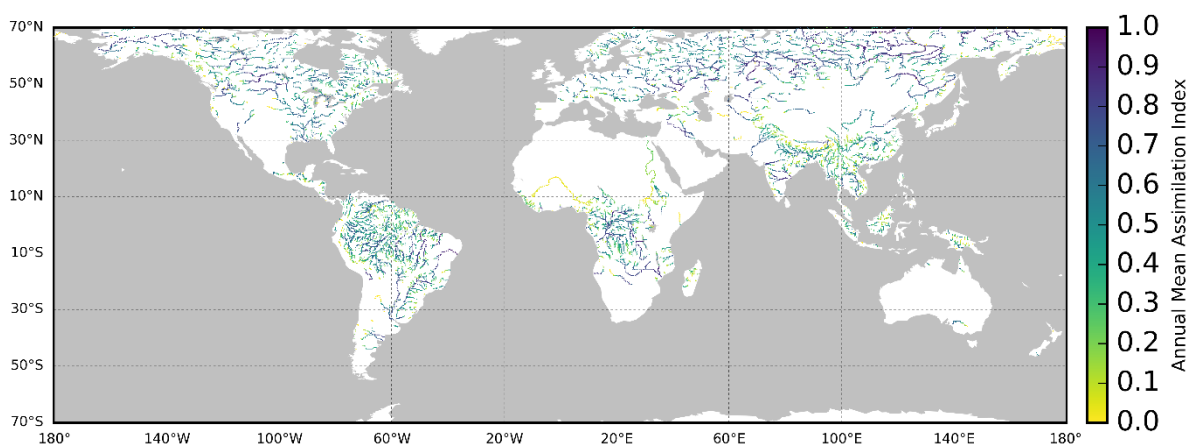


Figure 5.14 : Global annual mean AI for different runoff experiment. Pixels $> 500 \text{ m}^3/\text{s}$ presented for visualization purposes.

(i.e. Amazon River: Figure 5.13a), because Manning's coefficient error induce error on discharge estimation. In contrast when the hydrograph emulated by the corrupted runoff forcing is significantly different from the true hydrograph the AI was higher ($AI > 0.7$). For example, Ob and Lena River (Figure 5.13c and d) show better AI and the corrupted discharge is scientifically different. In addition, Niger Basin shows low AI, that is due to error in runoff forcing produces from different LSM model. Taking this into account, assimilation in this experiment was done reasonably well that most downstream or midstream locations had large AI (>0.6), or the discharge of assimilated simulation mostly matches that of corrupted simulation.

5.3.3.3 Model Efficiency

In this section, we explain the results for model efficiency with and without data assimilation using the empirical local patch. The Nash–Sutcliffe coefficients (NS) was additionally calculated for evaluating the result of different runoff experiment, because unlike the biased runoff experiment, the simulation results of corrupted and true simulations could be sometime similar and AI was not reasonably calculated in such cases. Figure 5.15 presents the spatial distribution of the NS coefficient for the blind runoff experiment. NS of river discharge at assimilated simulation (Figure 5.15a), corrupted simulation (Figure 5.15b), and the relative difference between two simulations.

Similar to the result of AI (Figure 5.14), the NS in the assimilated simulation was large (nearly 1.0) at midstream and downstream locations of the large-scale rivers. Although the upstream locations had a relatively small NS values (0.3 ~ 0.8) in some locations, the value rises in the downstream and it becomes almost 1.0 in the downstream. This denotes that data assimilation of SWOT observation has the potential to correct the simulation even when the model has inaccurate estimation of geographical parameters (Manning's coefficient) and/or has no accurate runoff data of current year. As the seasonal trends of each river basin is slightly differ between the corrupted and true simulations (Figure 5.15b), the NS values for the corrupted simulation were generally below the 0.5 (because we used an input runoff forcing from a different LSM). The difference of NS coefficient of corrupted and assimilate simulations (Figure 5.15c) can be discussed in three distant categories; 1. slight differences (0.0 – 0.3), 2. moderate differences (0.4 – 0.7), and 3. large differences ($NS > 0.8$). Amazon, Mekong and Cho-

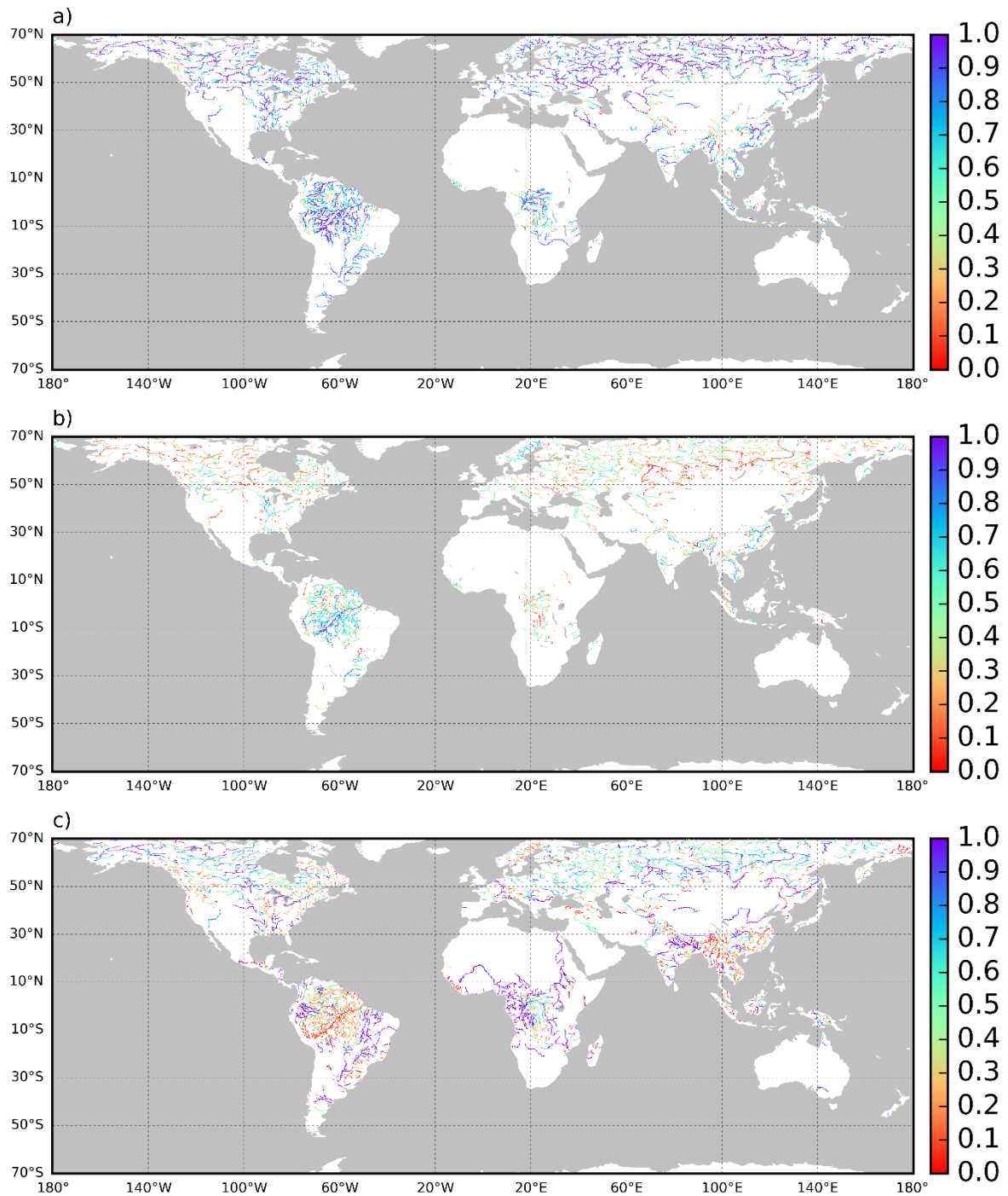


Figure 5.15 : Nash-Sutcliffe (NS) coefficient for model efficiency with a) assimilated discharge, b) corrupted discharge, and c) the difference between assimilated and corrupted discharge. Discharge values > 500 m³/s are presented for visualization purposes.

Priya rivers shows slight differences because the corrupted discharge is much closer to that of true discharge (Figure 5.15b). That means corrupted input runoff forcing was

relatively accurate for those places. Moderate differences can be seen on higher latitude rivers such as Lena, Ob, Yenisei, Volga, etc. even though the NS coefficient of corrupted is around 0.6 and that of assimilated is around 1.0. Those results indicate that those higher latitude rivers benefitted from high observation frequency despite of using empirical local patches. In contrast, rivers such as Mississippi, Congo, Nile, Ganges-Brahmaputra, etc. shows large difference, in addition to poor NS coefficient in corrupted simulation. Therefore, these results indicate that our assimilation scheme was successful even without accurate runoff forcing.

5.4 Conclusion

In this chapter, we examine the potential of physically-based data assimilation method to estimate global river discharge. We conduct three experiments namely, biased, blind, and different runoff experiments. In biased runoff experiment, a constant bias was added the true runoff forcing to use as corrupted runoff. Different year's runoff was used as corrupted runoff in blind runoff experiment. Whereas, runoff from a different LSM is used as corrupted runoff in different runoff experiment.

LETKF assimilation scheme was used with combination of empirical localization technique in global scale. We used the CaMa-Flood hydrodynamic model as the core of the data assimilation scheme. We derived empirical localization parameters using semi-variogram analysis from CaMa-Flood-modeled WSE data for 1980–2000. These empirical localization parameters were used for assimilating synthetic SWOT observations into CaMa-Flood model. We assumed that uncertainties arise from input runoff forcing (uncertainty in forcing) and Manning's coefficient (uncertainty in model/formulation).

The biased runoff experiment with the empirical local patch OSSE suggested that SWOT observations have the potential to improve regional-scale river discharge using physically based spatial dependency parameters. Overall, assimilation was effective, with high AI values even in upstream river sections where direct observations are unavailable (river width < 50 m). The NS coefficient suggests that the discharge can be correct even when the model formulation and input forcing result in low model efficiency. In summary, the hydrodynamics of continental-scale rivers can be reasonably estimated by assimilating SWOT observations using an empirical local patch, even when the model

formulation and input runoff forcing have errors. Furthermore, the blind runoff experiment carried out using empirical local patches indicated the ability of our assimilation scheme to improve discharge even without true runoff forcing. The blind runoff experiment creates a scenario that the runoff error is vary both spatially and temporally. In addition, different runoff experiment provides a realistic scenario actual observation have a district difference with the model predications. In the global scale the assimilation is relatively good in most of continental-scale river. Therefore, results from the different runoff experiment Hence, these three experiments provide knowledge useful for improving the frequency of SWOT observations and performing data assimilation at the global scale with less computational burden.

Chapter 6

Estimating Global River Bathymetry using Satellite Observations

6.1 Introduction

Assessment of global and regional water cycle is important to the society since it is depending on the water resources and is vulnerable to flood hazards. Even though river discharge is a key variable for water cycle assessments (Oki and Kanae 2006), number of accessible in-situ stream gaging station are not adequate for detailed assessments. Recent advances in satellite technology makes it possible to estimate river discharge via satellite remote sensing data, complementing data measured by existing in situ gage networks (Yoon et al. 2012). However river discharge cannot be directly measured from space, thus some of previous researchers (Alsdorf et al. 2007b; Bjerklie et al. 2005; Brakenridge et al. 2005; Kouraev et al. 2004; LeFavour and Alsdorf 2005) have used directly observable hydraulic data (such as channel width, water surface elevation (WSE), slope, and cross-sectional area) to estimate the river discharge.

The next-generation satellite altimetry mission, Surface Water and Ocean Topography (SWOT) satellite mission will be slated to launch in 2020 (Durand et al. 2010). The satellite mission intent to provide simultaneous mapping of inundation area and inland WSE (i.e., river, lakes, wetlands, and reservoirs), both temporally and spatially, using a Ka-band radar interferometer (Alsdorf et al. 2007b; Durand et al. 2010). With the channel centreline and width (above 50m; Biancamaria et al. 2016) which can be extracted from the dynamic water mask from SWOT (Smith and Pavelsky 2008), can be used to measure the water storage change in terrestrial water bodies and characterize river discharge (Lee et al. 2010). Even though it is possible to indirectly estimate WSE by the spatial intersection of a water mask and a digital terrain model, those shoreline methods were not eligible to characterize WSE for complex floodplain geomorphologies, such as those of the Amazon (Alsdorf et al. 2007a).

The river cross-sectional flow area will not be fully determined from SWOT as it will not measure the true depth to the river bottom. The SWOT sensor can directly measure the changes in water depth and cross-sectional area above the lowest measured WSE, but absolute river depths will not be observed (Yoon et al. 2012). In order to improve the discharge estimates from SWOT measurements, it would be necessary to estimate true cross-sectional flow area and river depth; thus, river bathymetry estimation would be necessary to gain remaining information. Some previous studies shown the potential to estimate coastal and stream bathymetry based on the relationship between water depth and spectral reflectance, measured by optical sensors (Lafon et al. 2002; Fonstad and Marcus 2005; Zhang et al. 2011); however, those theories are valid for shallow waters with little or no sediment load. Therefore, it is important to explore the methods to evaluate river bathymetry other than the methods mentioned above.

Most of the studies have disregarded or simplified the model uncertainties of hydrodynamic models in previous SWOT measurements pre-launch experiments (Andreadis et al. 2007; Biancamaria et al. 2011). Furthermore, uncertainty in bathymetry is said to be the largest of all uncertainties in the hydrodynamic modelling (Ikeshima et al. 2017). Ensemble data assimilation methods were able to retrieve the bathymetric depth and slope from WSE measurements and the LISFLOOD-FP model over a 240-km reach of the Amazon River floodplain (Durand et al. 2008). The methodology was able to retrieve the bathymetric depth and slope to within 56 cm and 0.30 cm/km, respectively,

by exploiting the flooding extent over the Amazon River floodplain. However, their study was limited by the assumption of simplified bathymetry; spatial variations in bathymetry at scales ≤ 50 km were not modelled. Yoon et al. (2012) had presented a methodology which has a potential of estimating the bed elevation and water depths from SWOT observations using the Local Ensemble Batch Smoother (LEnBS) for the Ohio River, but they only considered two critical uncertainties: precipitation forcing that propagates to boundary inflows and river bathymetry errors.

The purpose of this chapter is to use simulated SWOT observations to evaluate the potential of estimating river discharge and bathymetry on a global scale. We adopt LETKF and state-parameter estimation schemes (Evensen, 2009) to assimilate both WSE and bathymetry for integrating future SWOT observations into a global river hydrodynamic model, Catchment-based Macro-scale Floodplain (CaMa-Flood; Yamazaki et al. 2011), we achieved global-scale data assimilation at a reasonable computational cost.

6.2 Methodology

6.2.1 Observing system simulation experiment

We used an observing system simulation experiment (OSSE :Figure 6.1) (Andreadis et al. 2007; Yoon et al. 2012) to assess the potential of estimating river bathymetry on a global scale. The OSSE consists of three separate simulations: ‘true simulation’, ‘corrupted simulation (or open simulation)’, and ‘assimilated simulation’. CaMa-Flood hydrodynamic model (Yamazaki et al. 2011, 2012, 2013) was used to generate the ‘true’, ‘corrupted’, and ‘assimilated’ simulations (see Figure 6.1). For the OSSE, synthetic SWOT observations were generated from ‘true simulation’, then synthetic SWOT observations were integrated into the CaMa-Flood model using LETKF assimilation scheme via state-parameter estimation scheme (Evensen 2009), a method used to estimate non-observable model parameters (i.e. river bathymetry, Manning’s coefficient) using observable states. The LETKF scheme is applied to each daily time step during the experimental period and uncertainty in bathymetry is sequentially analysed and updated.

The ‘true simulation’ was performed to create synthetic SWOT observations, where CaMa-Flood was forced by true (assumed to be true) input runoff forcing (non-

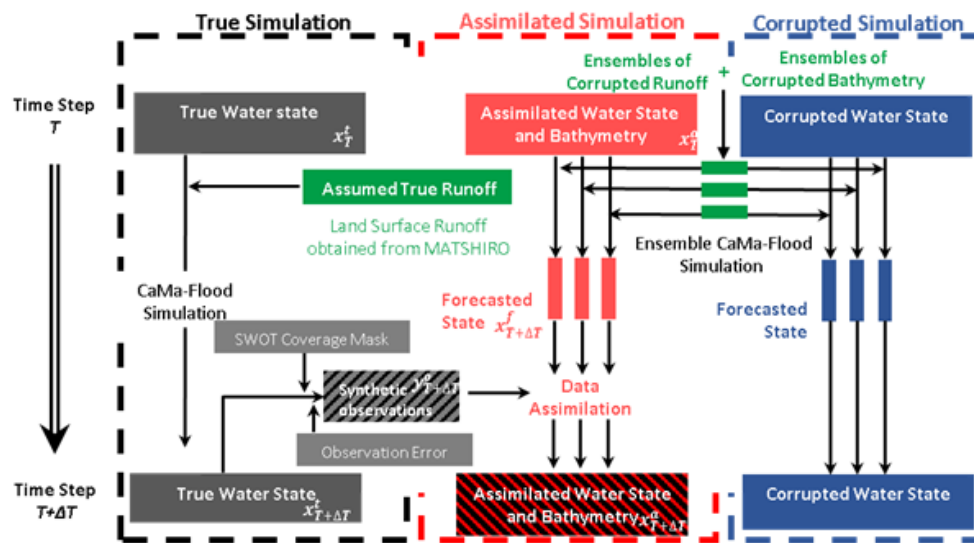


Figure 6.1: General framework of the observing system simulation experiment (OSSE) for river bathymetry assimilation

corrupted forcing) and true river channel bathymetry. Using the true states and parameters the true water state (river discharge, WSE, and water storage) was created. Then, synthetic SWOT observations were generated by applying the SWOT coverage mask to the true water surface elevations followed by addition of noise.

An ‘corrupted simulation’ was performed to compare the corrupted state with the ‘assimilated’ and ‘true’ simulations. The ‘corrupted simulation’ in this study was executed using the river model identical to the ‘true simulation’ but with corrupted river channel bathymetry and corrupted runoff forcing.

We executed the ‘assimilated simulation’ to test the potential of assimilation using SWOT observations for estimate global river bathymetry and discharge. We used the same model settings as the ‘corrupted simulation’, but with assimilating synthetic SWOT observations. At the end of each day, the synthetic SWOT observations were assimilated into the forecasted water state and corrupt bathymetry, and the initial conditions of the simulation for the following day were updated by the assimilated water state and river bathymetry was updated for the next day. The assimilation of both river channel bathymetry and WSE was done using LETKF.

6.2.2 Corrupted River Bathymetry

Creation of a corrupted channel bathymetry required two steps; 1. creating the base corrupted river bathymetry, and 2. adding noise to create ensembles. In the first step, average river water depth of the previous year (1990 or 2007) (avg_Dr) subtracted from average WSE of the for 1980-2000 (avg_WSE) for each river pixel in the model. In CaMa-Flood it is convenient to corrupt river channel height (B). Therefore, corrupted river channel height ($corrpt_B$) is created by subtracting, difference of avg_WSE and avg_Dr from true river bank elevation. As the second step, we added random noise to $corrpt_B$ following Gaussian normal distribution. From the second step, 20 ensembles were created considering the errors of Monte Carlo sampling and the computational cost of CaMa-Flood model. We limited ensembles to 20 because the computational cost of CaMa-Flood simulations significantly higher than the data assimilation algorithm even though the errors in the Monte Carlo sampling decrease with increasing size n of ensembles following $1/\sqrt{n}$.

6.2.3 Data assimilation strategy

A data assimilation scheme is typically used to estimate time-varying model state variables, e.g., hydraulic model states, such as discharge or water depth. In addition, data assimilation techniques can be used to estimate model parameters that are not directly observable (e.g., river bathymetry) via state-parameter estimation schemes (Evensen 2009). In this study we utilize the LETKF (Hunt et al. 2007) to simultaneously estimate river depth and bathymetry using SWOT observations. The computational cost using Ensemble Kalman Filter (EnKF) in global scale can be reduced by LETKF, which enables data assimilation at a global scale.

Our implementation of the data assimilation strategy involves: (1) the propagation of the model state variables in time via the CaMa-Flood model, and (2) the update of the state variables based on SWOT observations using LETKF. The LETKF analysis equation for the update is:

$$X^a = X^f + E^f \left[VD^{-1}V^T(HE^f)^T(R/w)^{-1}(Y^o - HX^f) + \sqrt{(m-1)}VD^{-1/2}V^T \right], \quad \text{eq 6.1}$$

where X^a is the posterior state estimator (or assimilated); X^f is the prior state estimator (or forecast); Y^o is the observation (here WSE); H is the observation operator, which linearly relates the observation and the state; m is the number of ensembles; E^f is prior state error covariance that is directly obtained from the ensembles; R is the observation error covariance that is determined by the uncertainty of the measurements; w is the localization weight; and VDV^T is given by;

$$VDV^T = (m - 1)I + (HE^f)^T R^{-1} HE^f , \quad \text{eq 6.2}$$

from Eigenvalue decomposition of VDV^T , $VD^{-1}V^T$ and $VD^{-1/2}V^T$ can be calculated.

We apply a data assimilation scheme to simultaneously estimate the river water depth y and bathymetry z from measurements of WSE; note $\text{WSE} = z + y$. The vector of unknowns is thus $x = [y, z]$. Thus, at a single location along the river and for a single observation time:

$$HX^f = H \begin{bmatrix} y \\ z \end{bmatrix}, \quad \text{eq 6.3}$$

where; $H = [1 \ 1]$

6.3 Experimental settings

In this chapter we evaluate potential of assimilating river bathymetry using two different local patch experiments namely; “Zero Patch” and “Empirical Patch” experiment. In Zero patch, we set the local patch size to 1 pixel, which means that only each target pixel itself was included in each local patch where the assimilation was performed only when direct observations are available. Empirical local patches which was derived in Chapter 4 was utilized in Empirical patch experiment. Using the empirical patch, the observation frequency can be increased.

6.3.1 Zero patch experiment

In the Zero patch, we consider only the target pixel for assimilation and therefore the assimilation was only when direct observations are available. A schematic figure showing how the Zero patch assimilation is process is presented in Figure 6.2. In the Figure 6.2 WSE is assimilated (red line) and correct initial condition for next time step (blue line), meantime river bathymetry is also updated (violet line).

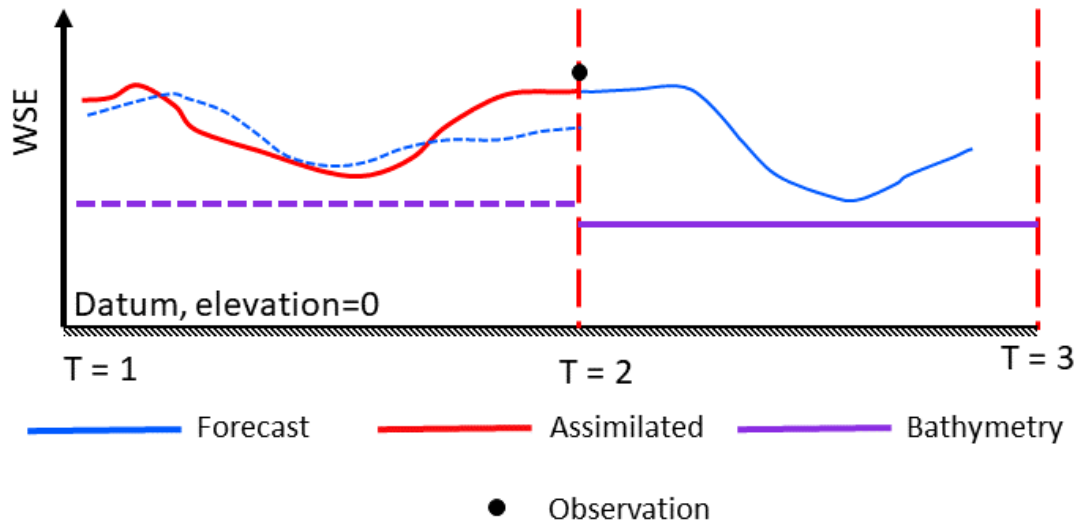


Figure 6.2 : Schematic diagram of assimilation of both WSE and river bathymetry in Zero patch experiment

6.3.2 Empirical patch experiment

In the Empirical patch experiment, we use the empirical local patches developed in the Chapter 4. Therefore, using empirical local patch, the observation frequency can be increased and assimilation can be done frequently than Zero patch experiment. Figure 6.2 presents a schematic diagram of the process of assimilation. WSE and river bathymetry is assimilated at same time but the river bathymetry is updated for next time

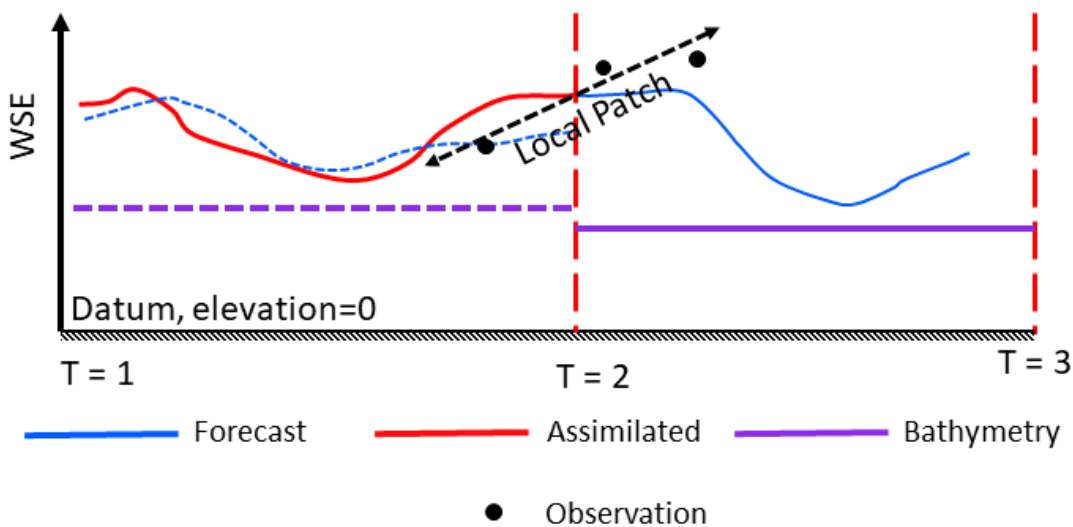


Figure 6.3 : Schematic diagram of assimilation of both WSE and river bathymetry in Empirical patch experiment

step (violet line). In this experiment not necessarily, the direct observation but all the observations inside the local patch (indicate by broken two-way arrow).

6.3.3 Evaluation method

We used the ‘assimilation index’ (AI: Ikeshima et al. 2017), to evaluate the effectiveness of data assimilation in this OSSE. AI is calculated from the ratio of parameter (such as river discharge, river bathymetry) error rates in the assimilated and corrupted simulations using equation (eq 6.4):

$$AI = 1 - \left| \frac{True\ Value - Assimilated\ Value}{True\ Value - Corrupted\ Value} \right|, \quad \text{eq 6.4}$$

The AI describes the similarity between the assimilated and true simulations, compared with corrupted simulation. A high AI (maximum of 1) indicates that the assimilated value is close to the true value, whereas a low AI indicates that the value was not improved from the corrupted value. The AI is a metric representing the relative effectiveness of data assimilation and not a measure of simulation accuracy. Furthermore, RMSE was used to evaluate the assimilation of river bathymetry and percentage bias (pBIAS) of annual mean discharge.

6.4 Result

6.4.1 Zero patch experiment

In this section we present the results of Zero patch experiment. Bathymetry of main stem of Ob and Congo rivers extensively presented for visualize the assimilation of river bathymetry. River discharge was presented for upstream, midstream, and downstream of Ob and Congo rivers. Then the annual mean global AI assimilated discharge and river bathymetry is presented.

6.4.1.1 Assimilated river bathymetry

Figure 6.4 shows the assimilated results of river bathymetry of 2975km of main-stream of Ob river (Figure 6.4a)) and 2684km of main-stream of Congo River (Figure 6.4b)) after 1 year (1991) of the simulation as for an example of our global assimilation. In Figure 6.4, 20 ensembles of assimilated bathymetry (red) indicate a convergence towards true bathymetry (black) from corrupted bathymetry (blue). RMSE is presented

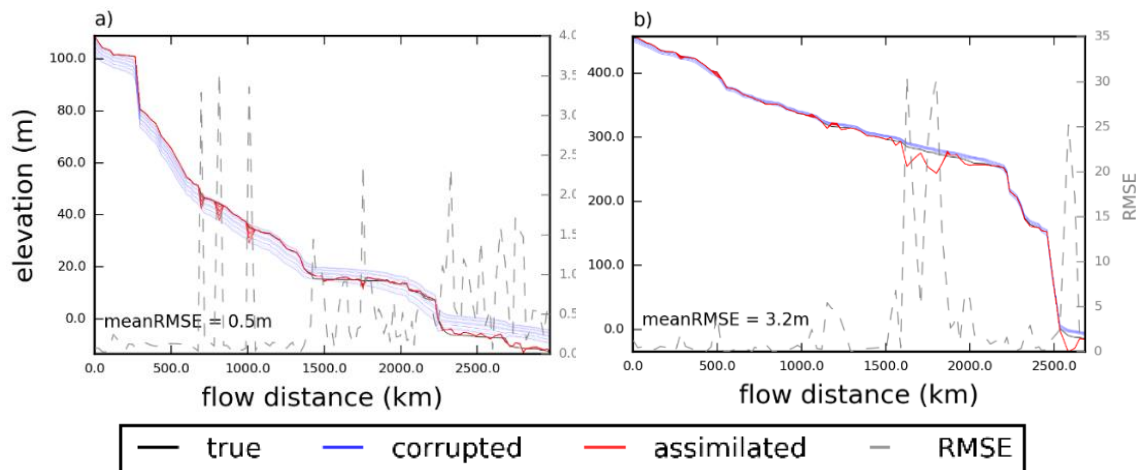


Figure 6.4: Assimilated bathymetry for Zero patch experiment of main-stream of a) Ob River b) Congo River. River bathymetry of true, corrupted, and assimilated simulation are shown in black, red, and blue lines. RMSE is presented in grey dotted lines. The mean RMSE of assimilated bathymetry of the river reach is shown in the left lower corner.

in grey colour and it had a 0.5m and a 3.2m of mean RMSE respectively Ob and Congo rivers for the selected river reaches. In the Ob river, larger errors can be seen at the points where there are no assimilations due to lack of observation. In contrast, there are some errors can be seen in the lower reaches of the Ob main-stream. Major errors in the Congo River main-stream can be seen around 1750km and lower reaches of Congo River.

Furthermore, the average RMSE for the mainstream of major rivers are considerably low values such as Lena: 0.5m; Niger: 2.3m; Indus: 1.5m; Mississippi: 2.0m; and Mekong: 3.7m. As in the Figure 6.4, there is a notable improvement of river bathymetry for 1 year of assimilation using CaMa-Flood and LETKF. Even though the bathymetry of most rivers assimilated well, some places show some sever errors in bathymetry even after assimilation (e.g., RMSE around 1750km of river reach).

The errors in the assimilated bathymetry are due to spatial discontinuities in synthetic SWOT observations spatially. Assimilation was done 1 pixel at a time thus there will be no assimilations done where there is no observation. Therefore, there are discontinuities at the assimilated bathymetry after each day, these discontinuities may cause large (small) water to the next river pixel which may cause artificially higher (lower) WSE. The artificially changed river water height (reflects on WSE) may cause errors in assimilated river bathymetry.

6.4.1.2 Assimilated river discharge

In this study, we recalculated the water storage at each grid after each assimilation using assimilated WSE and bathymetry. From the recalculation, the correction was transferred to the next step of CaMa-Flood simulation. Therefore, the initial condition for the time next step as well as the river bathymetry was updated. Figure 6.5 shows comparison between assimilated discharge (red), true discharge (black), and corrupted discharge (blue) of three different locations of Ob river and Congo river such as a), e) upstream (Ob: [82.0°E, 50.25°N]; Congo: [28.5°E, 9.25°S]); b), f) mid-stream (Ob: [69.0°E, 59.75°N]; Congo:[23.25°E, 1.75°S]); and c), g) downstream (Ob: [68.75°E, 67.0°N]; Congo: [13.0°E, -5.75°S]). It can be seen that AI of the upstream of the Ob and Congo rivers are high compared to AI of the downstream. In the downstream and mid-stream location (Figure 6.5b, c, e, and f) the assimilated discharge converged to true

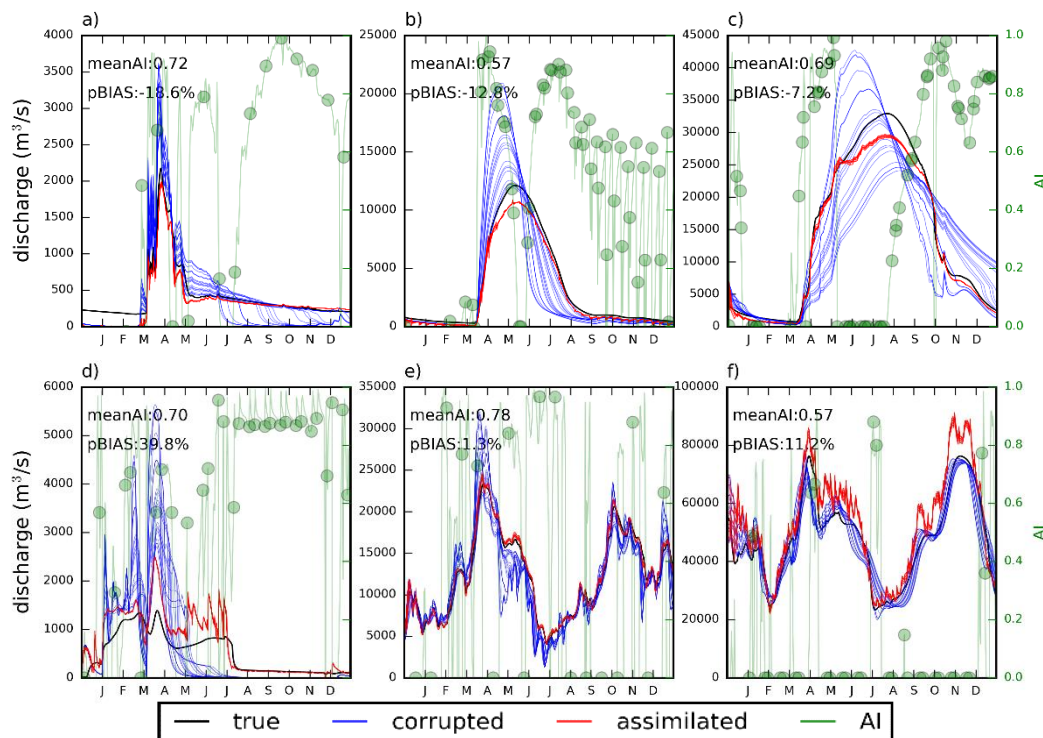


Figure 6.5 : Hydrographs of 1-year assimilation (January to December) for Zero patch experiment a), d) upstream, b), e) mid-stream, and c), f) down-stream of Ob River (a)-c)) and Congo River (d-f)). River discharges of true, corrupted, and assimilated simulation are shown in black, red, and blue lines. The AI is presented in green lines with green dots indicating the times of synthetic SWOT observations. The mean AI and percent bias (pBIAS) of the assimilated simulation are shown in the left upper corner of the hydrographs. Horizontal axis shows months from January to December by J, F, M, A, M, J, J, A, S, O, N, D.

discharge after the first observation (SWOT observations are denoted by green dots on the AI line). But on the upstream location of Ob river (Figure 6.5a) the deviation from the corrupted discharge of assimilation discharge was delayed (around March) because it was the most upstream location of Ob river where no upstream corrections. On the other hand, Congo upstream correction began around January (Figure 6.5d) where high flow occurred from January.

Congo downstream pBIAS is relatively improved than upstream locations. Mean AI of upstream is 0.72 and it remained 0.69 in downstream. Furthermore, pBIAS was improved from -18.6% to -7.2% which indicates assimilated discharge is closer to true discharge. Even though some places had very low AI due to the mean of corrupted discharge was closer to true discharge than assimilated discharge (beginning of June in Figure 6.5b) and mid-June in Figure 6.5c but the assimilated discharge ensemble spread became low. Here, we excluded the days when the corrupted discharge had $< 10\%$ error compared to the true discharge when calculating mean AI because the AI was unreasonably depressed despite the effectiveness of the assimilation (e.g., June and July at the downstream in Figure 6.5a). But it can be observed that on average, assimilated discharge was underestimated in all three locations in the Ob river (pBIAS is negative) but overestimated all three locations in the Congo river (pBIAS is positive). The results suggest that the SWOT data assimilation can improve river discharge estimation in rivers but upstream tributary correction need more time.

Rivers in higher latitude seems to have high AI value along the river. Figure 6.5 indicates that the Ob river which is located between latitudes 40°N - 70°N have a higher AI of 0.69 at downstream than the midstream (0.57). But downstream of the Congo river have a lower AI than both upstream and midstream, note that Congo river is located around equator. Downstream discharge of Ob river was assimilated well compared to the downstream of Congo river without affecting from the high flow situations because Ob river have more observations than Congo river.

6.4.1.3 Global estimation

Figure 6.6 presents comparison of global map of RMSE before and after the assimilation of 1-year. In the Figure 6.6a, there is a global mean RMSE of 4.2m and after the assimilation of 1-year the global RMSE was reduced to 1.4m (Figure 6.6b) which is

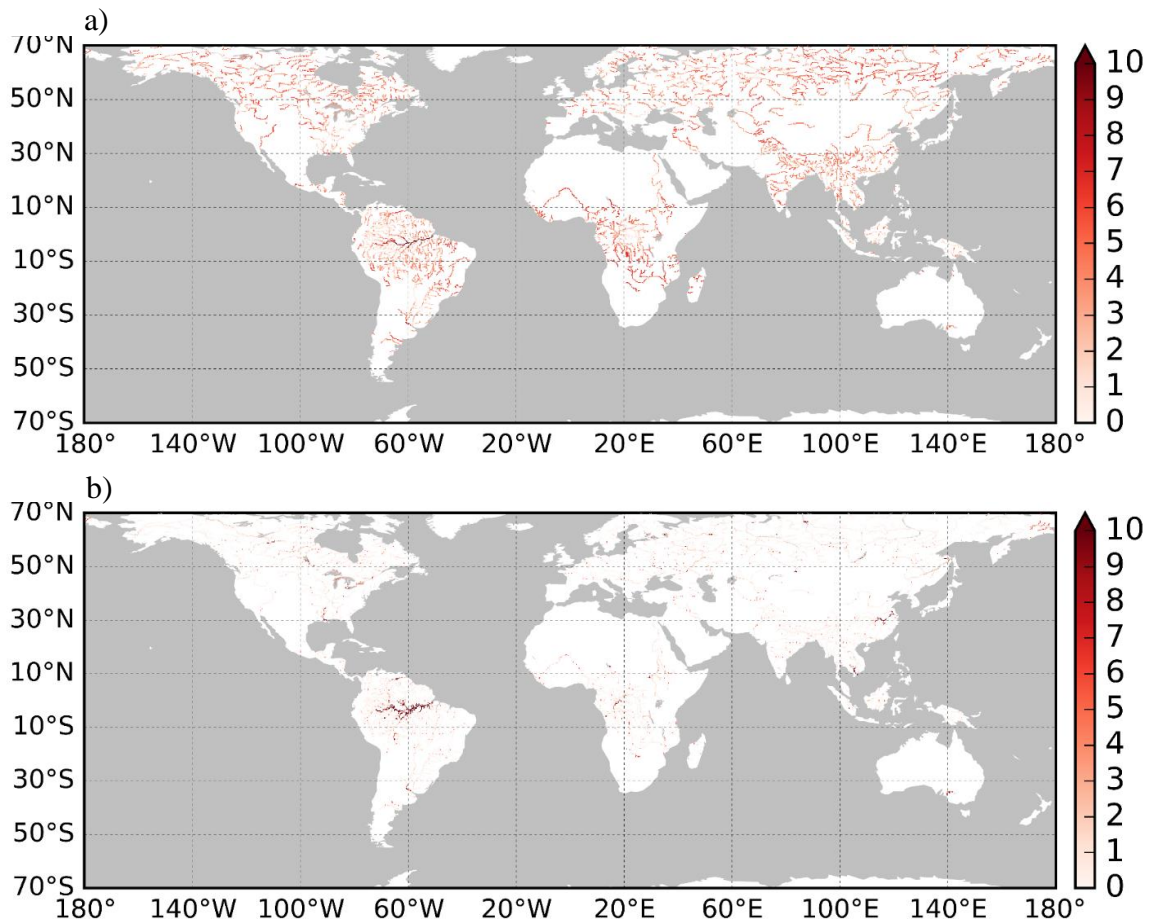


Figure 6.6 : Global map of root mean square error (RMSE) for a) before the assimilation and b) after 1-year assimilation for Zero patch experiment.

68% reduction. Majority of the global river bathymetry were assimilated well with a low RMSE values ($RMSE < 1.0m$) especially higher latitude rivers and upstream areas. However, there are some large errors can be seen at downstream Mississippi, downstream of Amazon, midstream Congo, downstream Yangtze, and downstream Mekong. Those errors are basically in the mild slope reaches where WSE is govern by not only on bathymetry but also on downstream WSE.

The AI map (Figure 6.7) reveals that the assimilation scheme was reasonably successful in estimating river bathymetry and discharge on a global scale. The Figure 6.7a shows the mean AI of river discharge and Figure 6.7b shows the AI of the river bathymetry at end of the assimilation circle. The mean AI of discharge was high at ($AI > 0.8$; indicated by magenta) most of the continental-scale rivers (excluding Amazon mainstream) and rivers located at high latitudes (Figure 6.7a). At downstream locations,

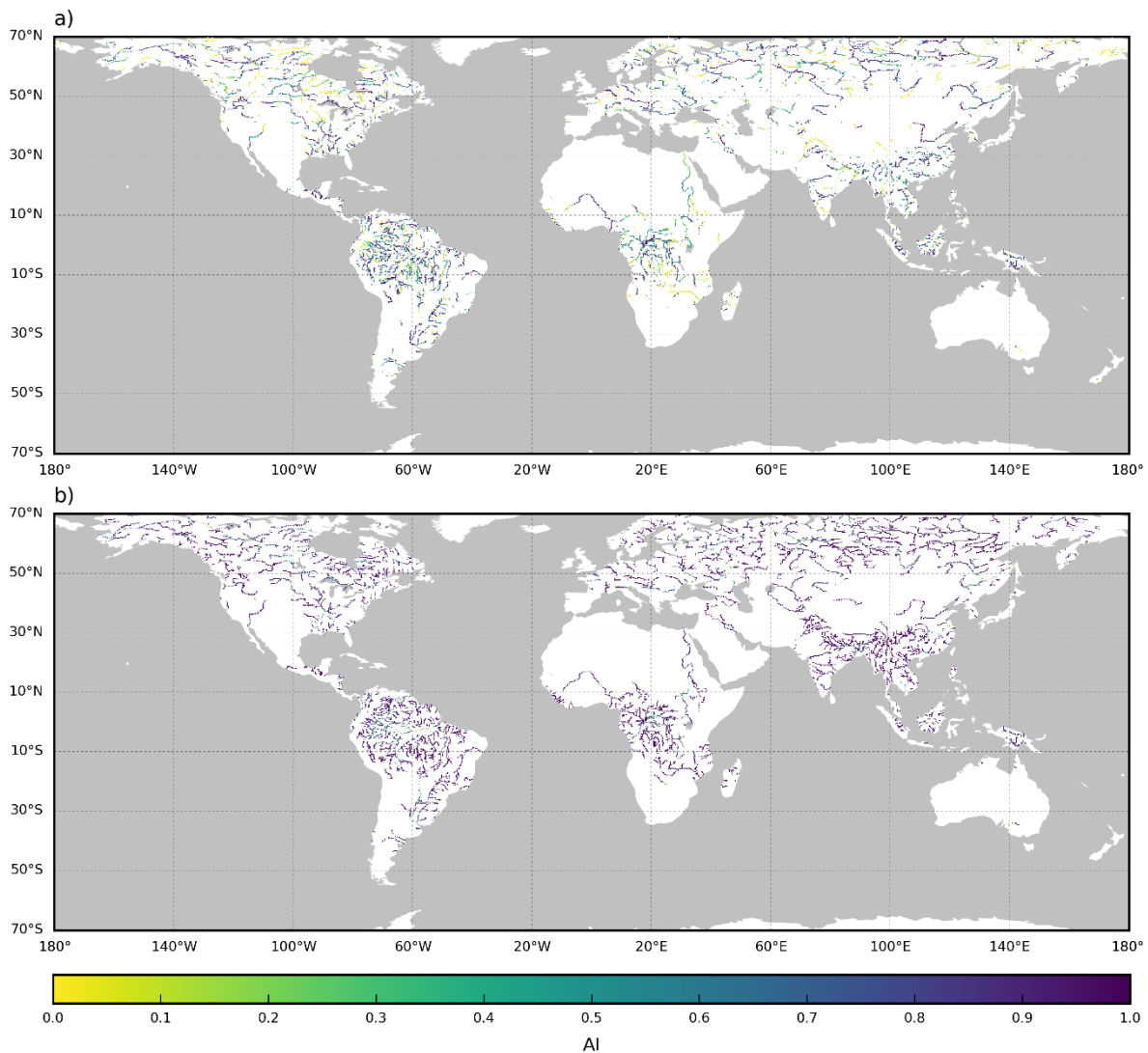


Figure 6.7 : Global map of AI of a) river discharge and b) river bathymetry for Zero patch experiment. Pixels with annual mean discharges $> 500 \text{ m}^3/\text{s}$ are shown for visualization

the upstream inflow correction seems to be effective since the AI increased even on days without local SWOT observations. Rivers located at high latitudes had high AIs even at upstream, due to the high local observation frequency. There were more than four observations available within the 21-day orbital cycle at latitudes $> 50^\circ\text{N}$, whereas lower-latitude regions had only one or two. In the Figure 6.7b AI of bathymetry is presented and most of the rivers have high AI values (AI > 0.8). After 1 year of assimilation, most of the river bathymetry reached closer to 1.0 of AI but some of the river downstream reaches have some errors where river have high flows. The results show the potential of LETKF assimilation scheme for estimating the true river bathymetry form simulated SWOT observation.

6.4.2 Empirical patch experiment

In this section we present the results of Empirical patch experiment. Bathymetry of main stem of Ob and Congo rivers extensively presented for visualize the assimilation of river bathymetry. River discharge was presented for upstream, midstream, and downstream of Ob and Congo rivers. Then the annual mean global AI assimilated discharge and river bathymetry is presented.

6.4.2.1 Assimilated river bathymetry

Figure 6.8 shows the assimilated results of river bathymetry of 2975km of main-stream of Ob river (Figure 6.8a)) and 2684km of main-stream of Congo River (Figure 6.8b)) after 1 year (2008) of the simulation as for an example of our global assimilation. In Figure 6.8, 20 ensembles of assimilated bathymetry (red) indicate a convergence towards true bathymetry (black) from corrupted bathymetry (blue). RMSE is presented in grey colour and it had a 2.0m and a 3.2m of mean RMSE respectively Ob and Congo rivers for the selected river reaches. In the both Ob and Congo rivers, almost all the places have seen by the SWOT satellite therefore assimilations present which is contrasting to the Zero patch experiment. Major errors in the Congo main-stream can be seen around lower reaches of Congo River.

Furthermore, the average RMSE for the mainstream of major rivers are considerably low values such as Lena: 1.1m; Niger: 1.2m; Indus: 0.8m; Mississippi: 4.2m; and Mekong: 0.9m. As in the Figure 6.8, there is a notable improvement of river bathymetry for 1 year of assimilation using CaMa-Flood and LETKF. Even though the bathymetry of most rivers assimilated well, some places show some errors in assimilated bathymetry (e.g., RMSE around 1500km and 2750km of Ob river reach).

The errors in the assimilated bathymetry are due to error covariance due to the limited ensemble size when assimilating distant observation. Assimilation was done using empirical local patch therefore some error covariance can promote. This makes some errors in the bathymetry. Therefore, there are discontinuities at the assimilated bathymetry after each day, these discontinuities may cause large (small) water to the next river pixel which may cause artificially higher (lower) WSE. The artificially changed river water height (reflects on WSE) may cause errors in assimilated river bathymetry.

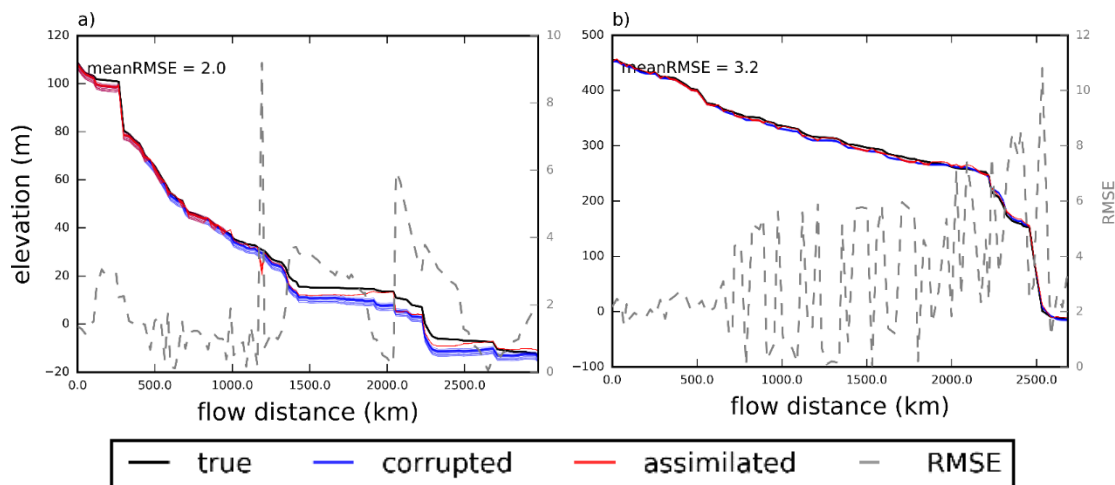


Figure 6.8 : Assimilated bathymetry for Empirical patch experiment of main-stream of a) Ob River b) Congo River. River bathymetry of true, corrupted, and assimilated simulation are shown in black, red, and blue lines. RMSE is presented in grey dotted lines. The mean RMSE of assimilated bathymetry of the river reach is shown in the left lower corner.

6.4.2.2 Assimilated river discharge

In this study, we recalculated the water storage at each grid after each assimilation using assimilated WSE and bathymetry. From the recalculation, the correction was transferred to the next step of CaMa-Flood simulation. Therefore, the initial condition for the time next step as well as the river bathymetry was updated. The update was done regularly than Zero patch experiment as observation frequency is higher in Empirical patch experiment. Figure 6.9 shows comparison between assimilated discharge (red), true discharge (black), and corrupted discharge (blue) of three different locations of Ob river and Congo river such as a), e) upstream (Ob: [82.0°E, 50.25°N]; Congo: [28.5°E, 9.25°S]); b), f) mid-stream (Ob: [69.0°E, 59.75°N]; Congo:[23.25°E, 1.75°S]); and c), g) downstream (Ob: [68.75°E, 67.0°N]; Congo: [13.0°E, -5.75°S]). It can be seen that AI of the upstream of the Ob and Congo rivers are high compared to AI of the downstream. In the downstream and mid-stream location (Figure 6.9b, c, e, and f) the assimilated discharge converged to true discharge after the first observation (direct SWOT observations are denoted by green dots on the AI line). But on the upstream location of Ob river (Figure 6.9a) the deviation from the corrupted discharge of assimilation discharge was delayed (around March) because it was the most upstream location of Ob river where no upstream corrections. On the other hand, Congo upstream correction began around January (Figure 6.9d) where high flow occurred from January.

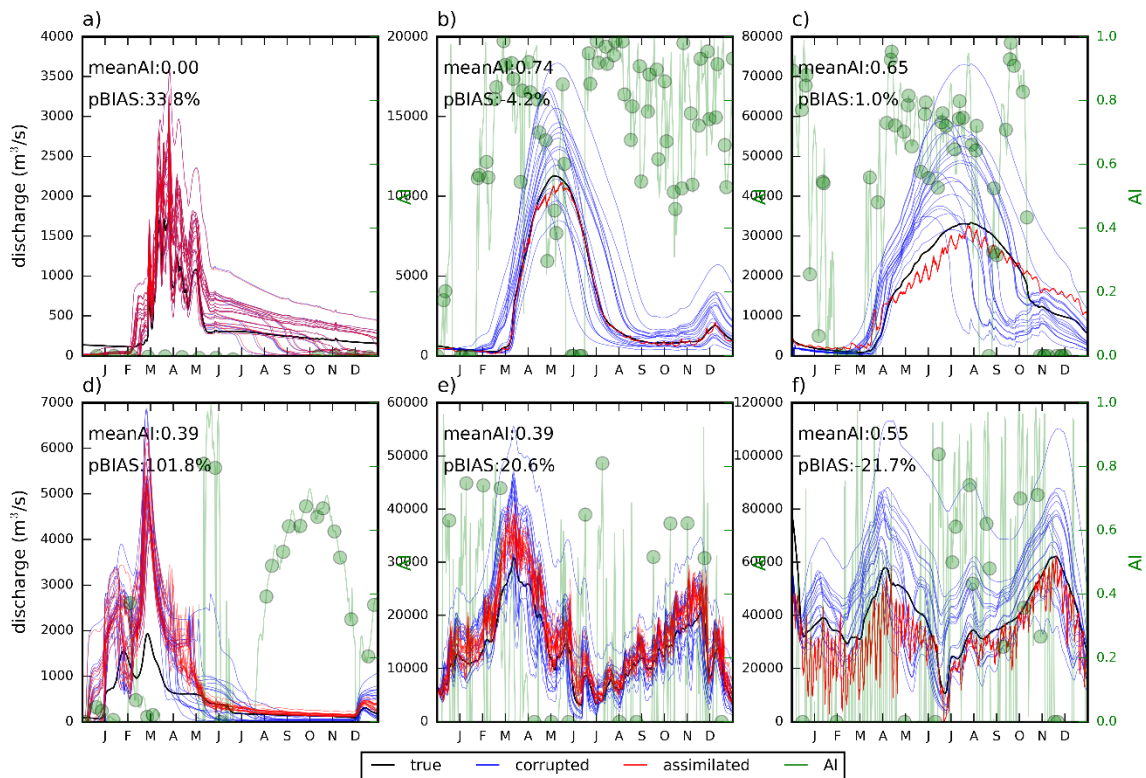


Figure 6.9 : Hydrographs of 1-year assimilation (January to December) for Empirical patch experiment a), d) upstream, b), e) mid-stream, and c), f) down-stream of Ob River (a-c)) and Congo River (d-f)). River discharges of true, corrupted, and assimilated simulation are shown in black, red, and blue lines. The AI is presented in green lines with green dots indicating the times of synthetic SWOT observations. The mean AI and percent bias (pBIAS) of the assimilated simulation are shown in the left upper corner of the hydrographs. Horizontal axis shows months from January to December by J, F, M, A, M, J, J, A, S, O, N, D.

Congo downstream pBIAS is relatively improved than upstream locations. Mean AI of upstream is 0.39 and it improved 0.55 in downstream. Furthermore, pBIAS was improved from 101.8% to -21.7% which indicates assimilated discharge is closer to true discharge. Even though some places had very low AI due to the mean of corrupted discharge was closer to true discharge than assimilated discharge (beginning of June in Figure 6.9b) and mid-June in Figure 6.9c but the assimilated discharge ensemble spread became low. Here, we excluded the days when the corrupted discharge had $< 10\%$ error compared to the true discharge when calculating mean AI because the AI was unreasonably depressed despite the effectiveness of the assimilation (e.g., June and July at the downstream in Figure 6.9a). But it can be observed that on average, assimilated discharge was underestimated in all three locations in the Ob river (pBIAS is negative)

but overestimated all three locations in the Congo river (pBIAS is positive). The results suggest that the SWOT data assimilation can improve river discharge estimation in rivers but upstream tributary correction need more time.

Rivers in higher latitude seems to have high AI value along the river. Figure 6.9a indicates that the Ob river which is located between latitudes 40°N - 70°N have a higher AI of 0.65 at downstream lower than the midstream (0.74). But downstream of the Congo river have a higher AI than both upstream and midstream, note that Congo river is located around equator. Downstream discharge of Ob river was assimilated well compared to the downstream of Congo river without affecting from the high flow situations because Ob river have more observations than Congo river.

6.4.2.3 Global estimation

Figure 6.10 presents comparison of global map of RMSE before and after the assimilation of 1-year. In the Figure 6.10, there is a global mean RMSE of 1.6m and after the assimilation of 1-year the global RMSE was reduced to 1.3m which is 15% reduction. Majority of the global RMSE is very low ($\text{RMSE} < 1.0\text{m}$) especially higher latitude rivers. However, there are some large RMSEs can be seen on downstream Mississippi, midstream Amazon, and downstream Congo. Those error are basically in the mild slope reaches where WSE is govern by not only on bathymetry but also on downstream WSE.

The AI map (Figure 6.11) reveals that the assimilation scheme was reasonably successful in estimating river bathymetry and discharge on a global scale. The Figure 6.11a shows the mean AI of river discharge and Figure 6.11b shows the AI of the river bathymetry at end of the assimilation circle. The mean AI of discharge was high at (indicating by magenta) most of the continental-scale rivers (excluding Amazon mainstream) and rivers located at high latitudes (Figure 6.11a). At downstream locations, the upstream inflow correction seems to be effective since the AI increased even on days without local SWOT observations. Rivers located at high latitudes had high AIs even at upstream, due to the high local observation frequency. There were more than four observations available within the 21-day orbital cycle at latitudes $> 50^{\circ}\text{N}$, whereas lower-latitude regions had only one or two. In the Figure 6.11b AI of bathymetry is presented and most of the rivers have highest AI value at 1.0. Furthermore, after 1 year of assimilation, some of the river bathymetry reached closer to 1.0 of AI but some of the

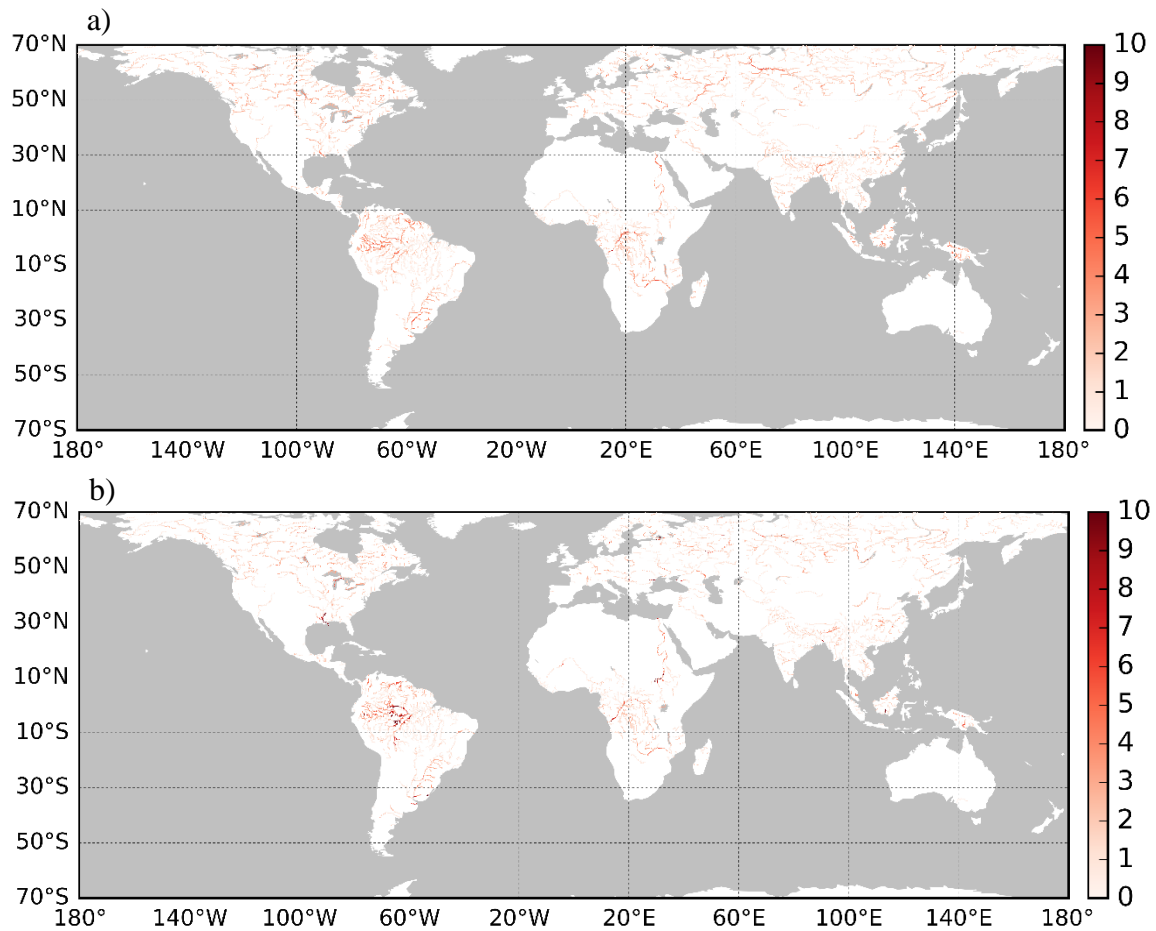


Figure 6.10 : Global map of root mean square error (RMSE) for a) before the assimilation and b) after 1-year assimilation for Empirical patch experiment

river downstream reaches have some errors where river have high flows. The results show the potential of LETKF assimilation scheme for estimating the true river bathymetry from simulated SWOT observation.

6.5 Conclusion

We conduct an OSSE using CaMa-Flood global river model to assimilate WSE and river bathymetry using simulated SWOT observations. The assimilation scheme consists of LETKF in combination with state-parameter estimation scheme. The effectiveness of assimilation was mainly evaluated with AI, which describes how close the assimilated value gets to the true value.

We use two different approaches namely Zero patch and Empirical patch experiments. In the Zero patch experiment the assimilation was done only at the times

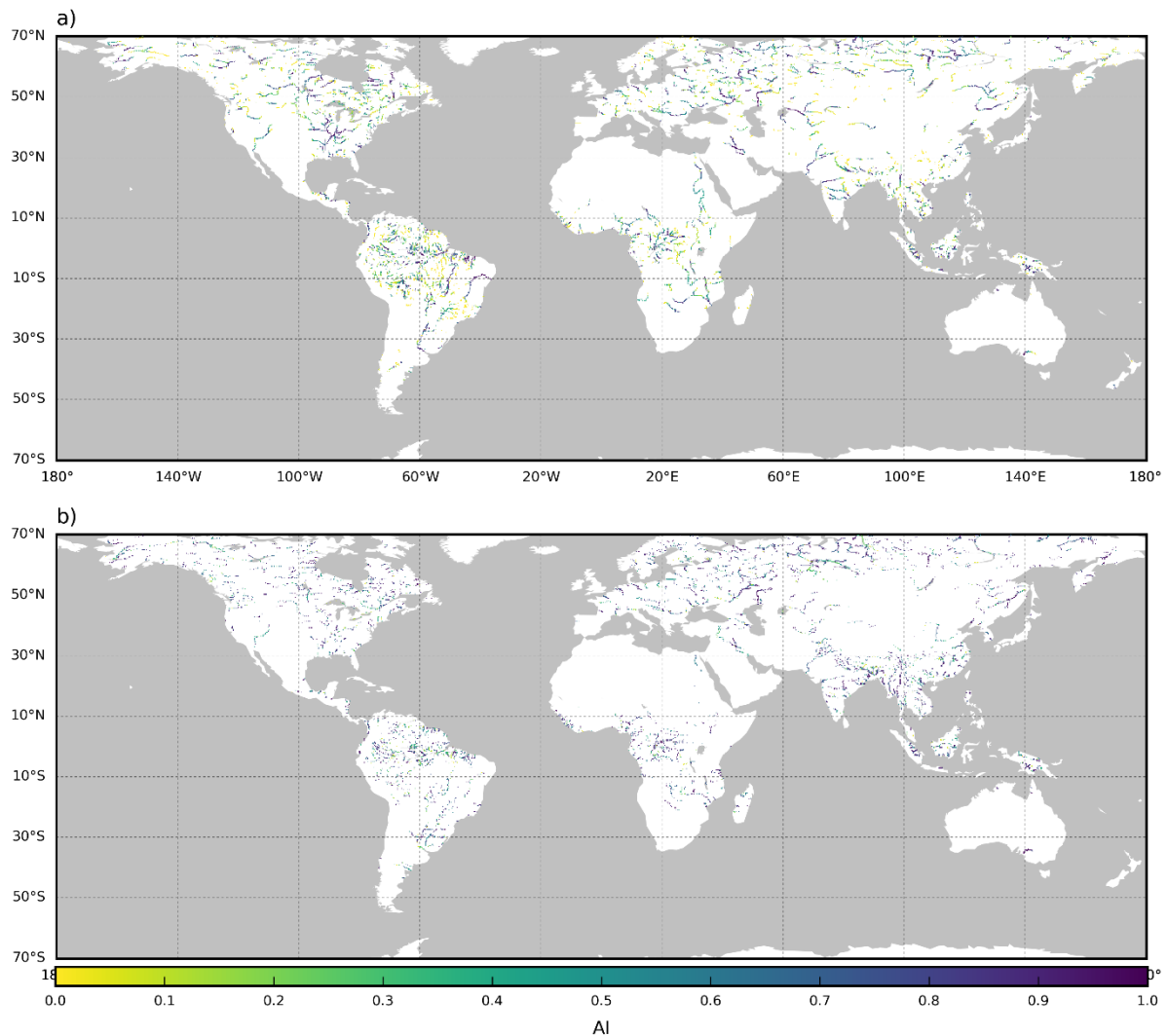


Figure 6.11 : Global map of AI of a) river discharge and b) river bathymetry for Empirical patch experiment. Pixels with annual mean discharges $> 500 \text{ m}^3/\text{s}$ are shown for when the SWOT observations are available. In contrast all the observations inside the empirical patch was used for the assimilation in the Empirical patch experiment.

Our assimilation scheme using Zero patch, showed the potential of estimating the bed elevation and water depths from SWOT observations, resulting in improved estimates of river discharge using SWOT observations. Bed elevation was successfully estimated without any in-situ measurements of river bathymetry from this assimilation framework. At the end 1 year of assimilation using combined state-parameter estimation scheme with LETKF, river bathymetry was rescued reaching AI nearly 1.0 and improved by 68.0% compared to corrupted bathymetry. Rivers located at high latitudes also maintained high AIs of river discharge in most areas, including upstream locations. River hydrographs

suggested that river hydrodynamics, such as annual mean flow or flood peak timing, can be reasonably estimated by assimilating SWOT observations even when realistic bathymetry data are not available.

Empirical local patch suggest that the observation frequency can be improved using the empirical patch, hence the inconsistency of bathymetry assimilation was improved in most downstream areas. The large errors in the mild slope areas were removed using empirical local patch. The RMSE was reduced by 15% after a 1-year assimilation.

The OSSE suggested that SWOT observations have the potential to improve global-scale river discharge estimation by correcting river bathymetry; in addition, empirical local patch can improve the assimilation. However, further studies are required to apply the developed data assimilation framework to real SWOT observations in the future. In this study, we only considered one critical uncertainty: river bathymetry errors but our future work will consider other uncertainties in the hydrodynamic model, such as the Manning's roughness coefficient.

Chapter 7

Conclusions and Recommendations

7.1 Conclusions

The main objective of this study is to improve hydrodynamic model predictions using SWOT satellite observations in continental-scale rivers. We used a physically based data assimilation method with LETKF algorithm to estimate the correct hydrodynamic model states and/or parameters. We use synthetic SWOT observations as actual observation data is still not available.

Our extensive literature review found several gaps in the knowledge of assimilation of SWOT observations into a global hydrodynamic model. Those major limitations are;

1. high computational cost of Ensemble Kalman Filter (EnKF) in continental-scale
2. inefficient localization techniques limit the advantage of assimilating more observations
3. testing more realistic scenarios in data assimilation
4. estimating correct river bathymetry in local-scale (river length ≤ 1500 km).

To address those four major science questions, we designed our study with having objectives such as: 1. development of a physically based data assimilation to address the computational efficiency and the inefficient localization at continental-scale in chapter 4; 2. more realistic scenarios were tested in chapter 5; and 3. global scale river bathymetry assimilation was performed in chapter 6.

7.1.1 A physically based empirical localization method

The empirical local patches were derived adaptively for each river pixel, with consideration of spatial auto-correlation. We were able to use the maximum number of observations for assimilation without promoting error covariance due to the limited sample size by using empirical local patches. Conventional local patches cannot filter based on error covariance of observations, which lead to spurious errors from small tributaries. Using the empirical local patch technique allows use of distant observations, which cannot be effectively used with the conventional local patch method. Therefore, the limitations of conventional patches can be overcome using empirical local patches.

In the future perspectives on satellite derived hydrologic parameters can further developed to improve hydrodynamic modelling by data assimilation techniques in global scale. Due to improvement of computer facilities and efficient algorithms to estimate correct river parameters can facilitate the hydrological forecasts in positive manner. The developed physically based empirical localization method can be used with any observation on river data. It may be needed to fine tune the size of the empirical local patches depending on the number of ensembles and the observation error.

In Chapter 4, we used WSE data simulated by CaMa-Flood hydrodynamic model, so these empirical local patches were based on CaMa-Flood model. Therefore, there may be a bias towards model in the assimilation scheme. If we can utilize global observed data set it will be the ideal scenario for development of this kind of data assimilation scheme. But with the enhancement of computer facilities and data availability we can use WSE data from multiple data inputs and multiple models for developing the empirical local patches.

7.1.2 Estimating river discharge without realistic input runoff forcing

We applied a physically based empirical localization based LETKF algorithm to CaMa-Flood modelled WSE in global scale when realistic input runoff data is unavailable.

In most of the previous studies, a biased runoff conditions were tested (Andreadis et al. 2007; Biancamaria et al. 2011). But in Chapter 5, we extensively tested more realistic scenarios such as blind and different runoff cases where error varies both spatially and temporally.

Global river hydrodynamic model outputs were improved by assimilating satellite altimetry using physically based empirical localization method. Experiment with biased runoff experiment suggest that the assimilation can be used to overcome the relative biases in input data. Peak discharge and low flows can be reasonably estimated in blind runoff experiment. Whereas flood peak timing, low flow timing, and peak discharge can be estimated well in different runoff experiment.

In the Chapter 5, we did not consider spatially correlated errors for either Manning's coefficient or observations error covariance. The errors in Manning's coefficient can be modelled using multivariate normal distribution, but in that case Manning's coefficient spatial covariance should be known. On the other hand, the observation error covariances should be considered, taking into account the error sources of the satellite (Oubanas et al. 2018).

7.1.3 Estimating river bathymetry in continental-scale rivers

We examined two approaches to estimate correct river bathymetry; Zero and Empirical local patch assimilation scheme. In the zero local patch experiment we assimilate the direct observations only on days where direct observations are available. All the observations inside the empirical local patch were used to estimate the river bathymetry.

The river bathymetry was assimilated reasonably well in zero and empirical local patch experiments reducing the global RMSE respectively 68.0% and 15.0%. Even though, assimilation is not effective in the mild slope river reaches most of the river bathymetry was estimated close to the its' true value. Using empirical local patches, the assimilation effectiveness can be improved. In addition, river discharge was also improved by the assimilation and correcting the river bathymetries.

We use a simple method to corrupted the river bathymetry, and used non-correlated ensembles in this experiment in Chapter 6. Multivariate normal ensembles can be used to make ensembles of corrupted river bathymetry. Furthermore assimilation

methods which utilize a smoothing techniques can be utilise to improve river bathymetry estimation (Yoon et al. 2012).

7.2 Future perspectives

Future perspective involves creating realistic ensembles, try to increase number of ensembles, and realistic interpretation of model parameters. We can use multiple forcing scenarios as ensembles of input runoff forcing either multiple data with same land surface model (LSM) or same forcing data with multiple LSMs. If we can enhance the computing facilities increasing the number of ensembles will increase accuracy of the assimilation. On the other hand, the error of the model parameters will be able to model through multivariate normal distribution.

The physically based empirical localization (i.e. local patch and localization weight) data assimilation method can be used with the any other observations data sets (Jason 2, Envisat, ICESat, etc). We can adjust the size of the local patch according to ensemble size and the observation error of the observational data.

7.3 Recommendations

In this study, we evaluate the potential of assimilation synthetic SWOT observations to improve hydrodynamic model variables/parameters in global-scale. It will be worth to test our methodology using an available satellite data (Jason 2, Envisat, ICESat, etc).

On the other hand, before using actual SWOT data, it is necessary to develop a methodology to cope with difference of spatial resolution of SWOT observations and CaMa-Flood. One of the possibilities is to treat each observation as a different observation.

As the assimilations in the upstream provide low assimilation efficiency than the conventional local patches, conventional and empirical localization method can be combined using hybrid assimilation scheme to enhance data assimilation in the upstream areas.

The manning's coefficient is one of the parameters, it may be less possible to observe for while globe. In order to improve the hydrodynamic modelling, it may be necessary to develop methodologies to estimate the other hydraulic parameters (i.e. manning's coefficient).

References

- Akan, A. O., 2006: *Open Channel Hydraulics*. Elsevier Ltd., 359 pp.
- Alsdorf, D., D. Lettenmaier, and C. Vorosmarty, 2003: The need for global, satellite-based observations of terrestrial surface waters. *Eos (Washington, DC)*, **84**, <https://doi.org/10.1029/2003EO290001>.
- , P. Bates, J. Melack, M. Wilson, and T. Dunne, 2007a: Spatial and temporal complexity of the Amazon flood measured from space. *Geophys. Res. Lett.*, **34**, 1–5, <https://doi.org/10.1029/2007GL029447>.
- Alsdorf, D. E., 2003: Tracking Fresh Water from Space. *Science (80-.)*, **301**, 1491–1494, <https://doi.org/10.1126/science.1089802>.
<http://www.sciencemag.org/cgi/doi/10.1126/science.1089802>.
- Alsdorf, D. E., E. Rodríguez, and D. P. Lettenmaier, 2007b: Measuring surface water from space. *Rev. Geophys.*, **45**, RG2002, <https://doi.org/10.1029/2006RG000197>.
<http://www.agu.org/pubs/crossref/2007/2006RG000197.shtml>.
- Anderson, J. L., 2012: Localization and Sampling Error Correction in Ensemble Kalman Filter Data Assimilation. *Mon. Weather Rev.*, **140**, 2359–2371, <https://doi.org/doi/10.1175/MWR-D-11-00013.1>.
<https://rmets.onlinelibrary.wiley.com/doi/abs/10.1002/qj.169>.
- Andreadis, K. M., and G. J. P. Schumann, 2014: Estimating the impact of satellite observations on the predictability of large-scale hydraulic models. *Adv. Water Resour.*, **73**, 44–54, <https://doi.org/10.1016/j.advwatres.2014.06.006>.
- , E. A. Clark, D. P. Lettenmaier, and D. E. Alsdorf, 2007: Prospects for river discharge and depth estimation through assimilation of swath-altimetry into a raster-based hydrodynamics model. *Geophys. Res. Lett.*, **34**, 1–5, <https://doi.org/10.1029/2007GL029721>.
- Baker, V. R., 2008: Greatest Floods and Largest Rivers. *Large Rivers*, A. Gupta, Ed., John Wiley & Sons, Ltd
<https://onlinelibrary.wiley.com/doi/book/10.1002/9780470723722>.
- Barnes, H. H., 1967: *Roughness Characteristics of Natural Channels*. United States Government Printing Office,
https://pubs.usgs.gov/wsp/wsp_1849/pdf/wsp_1849.pdf.
- Bates, P. D., M. S. Horritt, and T. J. Fewtrell, 2010: A simple inertial formulation of the shallow water equations for efficient two-dimensional flood inundation modelling. *J. Hydrol.*, **387**, 33–45, <https://doi.org/10.1016/j.jhydrol.2010.03.027>.
<http://dx.doi.org/10.1016/j.jhydrol.2010.03.027>.
- Biancamaria, S., and Coauthors, 2010: Preliminary Characterization of SWOT Hydrology Error Budget and Global Capabilities. *IEEE J. Sel. Top. Appl. Earth Obs. Remote Sens.*, **3**, 6–19, <https://doi.org/10.1109/jstars.2009.2034614>.
- Biancamaria, S., and Coauthors, 2011: Assimilation of virtual wide swath altimetry to improve Arctic river modeling. *Remote Sens. Environ.*, **115**, 373–381, <https://doi.org/10.1016/j.rse.2010.09.008>.
<http://dx.doi.org/10.1016/j.rse.2010.09.008>.
- Biancamaria, S., D. P. Lettenmaier, and T. M. Pavelsky, 2016: The SWOT Mission and Its Capabilities for Land Hydrology. *Surv. Geophys.*, **37**, 307–337, <https://doi.org/10.1007/s10712-015-9346-y>.

- Bishop, C. H., B. J. Etherton, and S. J. Majumdar, 2002: Adaptive Sampling with the Ensemble Transform Kalman Filter. Part I: Theoretical Aspects. *Mon. Weather Rev.*, **129**, 420–436, [https://doi.org/10.1175/1520-0493\(2001\)129<0420:aswtet>2.0.co;2](https://doi.org/10.1175/1520-0493(2001)129<0420:aswtet>2.0.co;2).
- Bjerklie, D. M., D. Moller, L. C. Smith, and S. L. Dingman, 2005: Estimating discharge in rivers using remotely sensed hydraulic information. *J. Hydrol.*, **309**, 191–209, <https://doi.org/10.1016/j.jhydrol.2004.11.022>.
- Bonnema, M. G., S. Sikder, F. Hossain, M. Durand, C. J. Gleason, and D. M. Bjerklie, 2016: Benchmarking wide swath altimetry-based river discharge estimation algorithms for the Ganges river system. *Water Resour. Res.*, **52**, 2439–2461, <https://doi.org/10.1002/2015WR017296>.
<https://agupubs.onlinelibrary.wiley.com/doi/epdf/10.1002/2015WR017296>.
- Brakenridge, G. R., S. V. Nghiem, E. Anderson, and S. Chien, 2005: Space-based measurement of river runoff. *Eos, Trans. Am. Geophys. Union*, **86**, 185, <https://doi.org/10.1029/2005EO190001>.
- Chen, C., J. P. L. Cal, V. Lead, and R. Morrow, 2018: *SWOT Project SWOT Calibration / Validation Plan Initial Release*. 1–152 pp. <https://pdms.jpl.nasa.gov/>.
- Chiverton, A., J. Hannaford, I. Holman, R. Corstanje, C. Prudhomme, J. Bloomfield, and T. M. Hess, 2015: Which catchment characteristics control the temporal dependence structure of daily river flows? *Hydrol. Process.*, **29**, 1353–1369, <https://doi.org/10.1002/hyp.10252>.
- Chow, V. Te, 1959: *Open Channel Hydraulics*. McGraw-Hill, 680 pp.
- CNES, 2015: SWOT orbit. <https://doi.org/https://www.aviso.altimetry.fr/en/missions/future-missions/swot/orbit.html>. <https://www.aviso.altimetry.fr/en/missions/future-missions/swot/orbit.html> (Accessed January 6, 2018).
- Desjonquères, J. D., G. Carayon, N. Steunou, and J. Lambin, 2010: Poseidon-3 Radar Altimeter: New Modes and In-Flight Performances. *Mar. Geod.*, **33**, 53–79, <https://doi.org/10.1080/01490419.2010.488970>.
<http://www.tandfonline.com/doi/abs/10.1080/01490419.2010.488970>.
- Döll, P., H. Douville, A. Güntner, H. Müller Schmied, and Y. Wada, 2016: Modelling Freshwater Resources at the Global Scale: Challenges and Prospects. *Surv. Geophys.*, **37**, 195–221, <https://doi.org/10.1007/s10712-015-9343-1>.
- Domeneghetti, A., G. J. P. Schumann, R. P. M. Frasson, R. Wei, T. M. Pavelsky, A. Castellarin, A. Brath, and M. T. Durand, 2018: Characterizing water surface elevation under different flow conditions for the upcoming SWOT mission. *J. Hydrol.*, **561**, 848–861, <https://doi.org/10.1016/j.jhydrol.2018.04.046>.
<https://doi.org/10.1016/j.jhydrol.2018.04.046>.
- Durand, M., K. M. Andreadis, D. E. Alsdorf, D. P. Lettenmaier, D. Moller, and M. Wilson, 2008: Estimation of bathymetric depth and slope from data assimilation of swath altimetry into a hydrodynamic model. *Geophys. Res. Lett.*, **35**, 1–5, <https://doi.org/10.1029/2008GL034150>.
- , L. L. Fu, D. P. Lettenmaier, D. E. Alsdorf, E. Rodriguez, and D. Esteban-Fernandez, 2010: The surface water and ocean topography mission: Observing terrestrial surface water and oceanic submesoscale eddies. *Proc. IEEE*, **98**, 766–779, <https://doi.org/10.1109/JPROC.2010.2043031>.
- Durand, M., and Coauthors, 2016: An intercomparison of remote sensing river discharge estimation algorithms from measurements of river height, width, and slope. *Water*

- Resour. Res.*, **52**, 4527–4549, <https://doi.org/10.1002/2015WR018434>.
<http://doi.wiley.com/10.1002/2015WR018434>.
- Evensen, G., 1994: Sequential data assimilation with a nonlinear quasi-geostrophic model using Monte Carlo methods to forecast error statistics. *J. Geophys. Res.*, **99**, 10143, <https://doi.org/10.1029/94JC00572>.
<https://agupubs.onlinelibrary.wiley.com/doi/epdf/10.1029/94JC00572>.
- Evensen, G., 2009: The ensemble Kalman filter for combined state and parameter estimation. *IEEE Control Syst.*, **29**, 83–104, <https://doi.org/10.1109/MCS.2009.932223>.
<http://ieeexplore.ieee.org/ielx5/5488303/4939293/04939313.pdf?tp=&arnumber=4939313&isnumber=4939293>.
- Farr, T. G., and Coauthors, 2007: The Shuttle Radar Topography Mission. *Rev. Geophys.*, **45**, RG2004, <https://doi.org/10.1029/2005RG000183>.
<http://doi.wiley.com/10.1029/2005RG000183>.
- Fjørtoft, R., and Coauthors, 2014: KaRIn on SWOT: Characteristics of near-nadir Ka-band interferometric SAR imagery. *IEEE Trans. Geosci. Remote Sens.*, **52**, 2172–2185, <https://doi.org/10.1109/TGRS.2013.2258402>.
- Fonstad, M. A., and W. A. Marcus, 2005: Remote sensing of stream depths with hydraulically assisted bathymetry (HAB) models. *Geomorphology*, **72**, 320–339, <https://doi.org/10.1016/j.geomorph.2005.06.005>.
- Fu, L.-L., D. Alsdorf, R. Morrow, E. Rodriguez, and N. Mognard, 2012: *SWOT: The Surface Water and Ocean Topography Mission Wide-Swath Altimetric Measurement of Water Elevation on Earth*. 1–228 pp.
<https://ieeexplore.ieee.org/stamp/stamp.jsp?tp=&arnumber=6553583>.
- Garambois, P. A., and J. Monnier, 2015: Inference of effective river properties from remotely sensed observations of water surface. *Adv. Water Resour.*, **79**, 103–120, <https://doi.org/10.1016/j.advwatres.2015.02.007>.
- Giustarini, L., and Coauthors, 2011: Assimilating SAR-derived water level data into a hydraulic model: A case study. *Hydrol. Earth Syst. Sci.*, **15**, 2349–2365, <https://doi.org/10.5194/hess-15-2349-2011>.
- Gleason, C. J., and L. C. Smith, 2014: Toward global mapping of river discharge using satellite images and at-many-stations hydraulic geometry. *Proc. Natl. Acad. Sci.*, **111**, 4788–4791, <https://doi.org/10.1073/pnas.1317606111>.
<https://www.pnas.org/content/pnas/111/13/4788.full.pdf>.
- Hamill, T. M., J. S. Whitaker, and C. Snyder, 2001: Distance-Dependent Filtering of Background Error Covariance Estimates in an Ensemble Kalman Filter. *Mon. Weather Rev.*, **129**, 2776–2790, [https://doi.org/10.1175/1520-0493\(2001\)129<2776:DDFOBE>2.0.CO;2](https://doi.org/10.1175/1520-0493(2001)129<2776:DDFOBE>2.0.CO;2).
<http://journals.ametsoc.org/doi/abs/10.1175/1520-0493%282001%29129%3C2776%3ADDFOBE%3E2.0.CO%3B2>.
- Hanasaki, N., S. Kanae, T. Oki, K. Masuda, K. Motoya, N. Shirakawa, Y. Shen, and K. Tanaka, 2008a: An integrated model for the assessment of global water resources - Part 1: Model description and input meteorological forcing. *Hydrol. Earth Syst. Sci.*, **12**, 1007–1025, <https://doi.org/10.5194/hess-12-1007-2008>. www.hydrol-earth-syst-sci.net/12/1007/2008/.
- , ———, ———, ———, ———, ———, ———, and ———, 2008b: An integrated model for the assessment of global water resources - Part 2: Applications and assessments. *Hydrol.*

- Earth Syst. Sci.*, **12**, 1027–1037, <https://doi.org/10.5194/hess-12-1027-2008>.
www.hydrol-earth-syst-sci.net/12/1027/2008/.
- Houtekamer, P. L., H. L. Mitchell, P. L. Houtekamer, and H. L. Mitchell, 1998: Data Assimilation Using an Ensemble Kalman Filter Technique. *Mon. Weather Rev.*, **126**, 796–811, [https://doi.org/10.1175/1520-0493\(1998\)126<0796:DAUAEK>2.0.CO;2](https://doi.org/10.1175/1520-0493(1998)126<0796:DAUAEK>2.0.CO;2).
<http://journals.ametsoc.org/doi/abs/10.1175/1520-0493%281998%29126%3C0796%3ADAUAEK%3E2.0.CO%3B2>.
- Hunt, B. R., E. J. Kostelich, and I. Szunyogh, 2007: Efficient data assimilation for spatiotemporal chaos: A local ensemble transform Kalman filter. *Phys. D Nonlinear Phenom.*, **230**, 112–126, <https://doi.org/10.1016/j.physd.2006.11.008>.
- Ikeshima, D., D. Yamazaki, and K. Shinjiro, 2017: Application of Data Assimilation for a Global River Model: A Virtual Experiment at the Amazon Basin. *Annu. J. Hydraul. Eng. JSCE*, **73**, I_175-I_180, https://doi.org/https://doi.org/10.2208/jscejhe.73.I_175.
https://www.jstage.jst.go.jp/article/jscejhe/73/4/73_I_175/_article/-char/en.
- Jian, X., R. A. Olea, and Y. S. Yu, 1996: Semivariogram modeling by weighted least squares. *Comput. Geosci.*, **22**, 387–397, [https://doi.org/10.1016/0098-3004\(95\)00095-X](https://doi.org/10.1016/0098-3004(95)00095-X).
- Kalman, R. E., 1960: A New Approach to Linear Filtering and Prediction Problems. *J. Basic Eng.*, **82**, 35, <https://doi.org/10.1115/1.3662552>.
<http://fluidsengineering.asmedigitalcollection.asme.org/article.aspx?articleid=1430402>.
- Kim, H., P. J. F. Yeh, T. Oki, and S. Kanae, 2009: Role of rivers in the seasonal variations of terrestrial water storage over global basins. *Geophys. Res. Lett.*, **36**, 2–6, <https://doi.org/10.1029/2009GL039006>.
- Kouraev, A. V., E. A. Zakharova, O. Samain, N. M. Mognard, and A. Cazenave, 2004: Ob' river discharge from TOPEX/Poseidon satellite altimetry (1992–2002). *Remote Sens. Environ.*, **93**, 238–245, <https://doi.org/10.1016/j.rse.2004.07.007>.
- Lafon, V., J. M. Froidefond, F. Lahet, and P. Castaing, 2002: SPOT shallow water bathymetry of a moderately turbid tidal inlet based on field measurements. *Remote Sens. Environ.*, **81**, 136–148, [https://doi.org/10.1016/S0034-4257\(01\)00340-6](https://doi.org/10.1016/S0034-4257(01)00340-6).
- Lee, H., M. Durand, H. C. Jung, D. Alsdorf, C. K. Shum, and Y. Sheng, 2010: Characterization of surface water storage changes in Arctic lakes using simulated SWOT measurements. *Int. J. Remote Sens.*, **31**, 14–3931, <https://doi.org/10.1080/01431161.2010.483494>.
<http://www.informaworld.com/smpp/title~content=t713722504%5Cnhttp://dx.doi.org/10.1080/01431161.2010.483494%5Cnhttp://www.informaworld.com/>.
- LeFavour, G., and D. Alsdorf, 2005: Water slope and discharge in the Amazon River estimated using the shuttle radar topography mission digital elevation model. *Geophys. Res. Lett.*, **32**, 1–5, <https://doi.org/10.1029/2005GL023836>.
- Marcus, W. A., and M. A. Fonstad, 2010: Remote sensing of rivers: The emergence of a subdiscipline in the river sciences. *Earth Surf. Process. Landforms*, **35**, 1867–1872, <https://doi.org/10.1002/esp.2094>.
- Matgen, P., and Coauthors, 2010: Towards the sequential assimilation of SAR-derived water stages into hydraulic models using the Particle Filter: Proof of concept. *Hydrol. Earth Syst. Sci.*, **14**, 1773–1785, <https://doi.org/10.5194/hess-14-1773-2010>.
- Miyoshi, T., 2011: The Gaussian Approach to Adaptive Covariance Inflation and Its

- Implementation with the Local Ensemble Transform Kalman Filter. *Mon. Weather Rev.*, **139**, 1519–1535, <https://doi.org/10.1109/ICCSCE.2012.6487150>. <http://journals.ametsoc.org/doi/abs/10.1175/2010MWR3570.1>.
- , and S. Yamane, 2007: Local Ensemble Transform Kalman Filtering with an AGCM at a T159/L48 Resolution. *Mon. Wea. Rev.*, **135**, 3841–3861, <https://doi.org/10.1175/2007MWR1873.1>.
- , ———, and T. Enomoto, 2007: Localizing the Error Covariance by Physical Distances within a Local Ensemble Transform Kalman Filter (LETKF). *Sola*, **3**, 89–92, <https://doi.org/10.2151/sola.2007-023>.
- Moller, D., and D. Esteban-Fernandez, 2014: Near-Nadir Ka-band Field Observations of Freshwater Bodies. 143–155 <http://doi.wiley.com/10.1002/9781118872086.ch9>.
- Munier, S., A. Polebistki, C. Brown, G. Belaud, and D. P. Lettenmaier, 2015: SWOT data assimilation for operational reservoir management on the upper Niger River Basin S. *Water Resour. Res.*, **51**, 554–575, <https://doi.org/https://doi.org/10.1002/2014WR016157>. <https://agupubs.onlinelibrary.wiley.com/doi/epdf/10.1002/2014WR016157>.
- Nash, J. E., and J. V Sutcliffe, 1970: River Flow Forecasting Through Conceptual Models Part I-a Discussion of Principles*. *J. Hydrol.*, **10**, 282–290, [https://doi.org/10.1016/0022-1694\(70\)90255-6](https://doi.org/10.1016/0022-1694(70)90255-6).
- Neal, J., G. Schumann, P. Bates, W. Buytaert, P. Matgen, and F. Pappenberger, 2009: A data assimilation approach to discharge estimation from space. *Hydrol. Process.*, **23**, 3641–3649, <https://doi.org/10.1002/hyp.7518>. <http://jamsb.austms.org.au/courses/CSC2408/semester3/resources/ldp/abs-guide.pdf>.
- Oki, T., and S. Kanae, 2006: Global Hydrological Cycles and World Water Resources. *Science (80-.)*, **5790**, 1068–1072, <https://doi.org/10.1126/science.1128845>. <http://science.sciencemag.org/content/313/5790/1068.full.pdf+html>.
- Oubanas, H., I. Gejadze, P. O. Malaterre, M. Durand, R. Wei, R. P. M. Frasson, and A. Domeneghetti, 2018: Discharge Estimation in Ungauged Basins Through Variational Data Assimilation: The Potential of the SWOT Mission. *Water Resour. Res.*, **54**, 2405–2423, <https://doi.org/10.1002/2017WR021735>.
- Pavelsky, T. M., M. T. Durand, K. M. Andreadis, R. E. Beighley, R. C. D. Paiva, G. H. Allen, and Z. F. Miller, 2014: Assessing the potential global extent of SWOT river discharge observations. *J. Hydrol.*, **519**, 1516–1525, <https://doi.org/10.1016/j.jhydrol.2014.08.044>. <http://dx.doi.org/10.1016/j.jhydrol.2014.08.044>.
- Pedinotti, V., A. Boone, S. Ricci, S. Biancamaria, and N. Mognard, 2014: Assimilation of satellite data to optimize large-scale hydrological model parameters: a case study for the SWOT mission. *Hydrol. Earth Syst. Sci.*, **18**, 4485–4507, <https://doi.org/10.5194/hess-18-4485-2014>. <http://doi.wiley.com/10.1002/2014WR015716>.
- Reichle, R. H., 2008: Data assimilation methods in the Earth sciences. *Adv. Water Resour.*, **31**, 1411–1418, <https://doi.org/10.1016/j.advwatres.2008.01.001>. <http://dx.doi.org/10.1016/j.advwatres.2008.01.001>.
- Revel, M., D. Yamazaki, and S. Kanae, 2018: Model Based Observation Localization Weighting Function for Amazon Mainstream. *J. Japan Soc. Civ. Eng. Ser. B1 (Hydraulic Eng.)*, **74**, I_157-I_162.

- Rodriguez, E., D. E. Fernandez, E. Peral, C. W. Chen, J.-W. De Bleser, and B. Williams, 2018: *Surface Water and Ocean Topography Mission (SWOT) Science Requirements Document. Second Release (v1.1)*. https://swot.jpl.nasa.gov/docs/D-61923_SRD_Rev_B_20181113.pdf.
- Skøien, J. O., G. Blöschl, and A. W. Western, 2003: Characteristic space scales and timescales in hydrology. *Water Resour. Res.*, **39**, 1304–1323, <https://doi.org/10.1029/2002WR001736>.
<http://doi.wiley.com/10.1029/2002WR001736>.
- Smith, L. C., and T. M. Pavelsky, 2008: Estimation of river discharge, propagation speed, and hydraulic geometry from space: Lena River, Siberia. *Water Resour. Res.*, **44**, 1–11, <https://doi.org/10.1029/2007WR006133>.
- Szunyogh, I., E. J. Kostelich, G. Gyarmati, D. J. Patil, B. R. Hunt, E. Kalnay, E. Ott, and J. A. Yorke, 2005: Assessing a local ensemble Kalman filter: Perfect model experiments with the National Centers For Environmental Prediction global model. *Tellus, Ser. A Dyn. Meteorol. Oceanogr.*, **57**, 528–545, <https://doi.org/10.1111/j.1600-0870.2005.00136.x>.
- , ———, G. Gyarmati, E. Kalnay, B. R. Hunt, E. Ott, E. Satterfield, and J. A. Yorke, 2008: A local ensemble transform Kalman filter data assimilation system for the NCEP global model. *Tellus, Ser. A Dyn. Meteorol. Oceanogr.*, **60 A**, 113–130, <https://doi.org/10.1111/j.1600-0870.2007.00274.x>.
- Takata, K., S. Emori, and T. Watanabe, 2003: Development of the minimal advanced treatments of surface interaction and runoff. *Glob. Planet. Change*, **38**, 209–222, [https://doi.org/10.1016/S0921-8181\(03\)00030-4](https://doi.org/10.1016/S0921-8181(03)00030-4).
- The UN Office for Disaster Risk, and Centre for Research on the Epidemiology of Disasters, 2015: *The Human Cost of Weather Related Disasters 1995-2015*. 30 pp. https://www.unisdr.org/files/46796_cop21weatherdisastersreport2015.pdf.
- Tippett, M. K., J. L. Anderson, C. H. Bishop, T. M. Hamill, and J. S. Whitaker, 2003: Ensemble Square Root Filters*. *Mon. Weather Rev.*, **131**, 1485–1490, [https://doi.org/10.1175/1520-0493\(2003\)131<1485:ESRF>2.0.CO;2](https://doi.org/10.1175/1520-0493(2003)131<1485:ESRF>2.0.CO;2).
[http://ams.allenpress.com/perlserv/?request=get-abstract&doi=10.1175%2F1520-0493\(2003\)131%3C1485:ESRF%3E2.0.CO%3B2](http://ams.allenpress.com/perlserv/?request=get-abstract&doi=10.1175%2F1520-0493(2003)131%3C1485:ESRF%3E2.0.CO%3B2).
- Whitaker, J. S., and T. M. Hamill, 2002: Ensemble Data Assimilation without Perturbed Observations. *Mon. Weather Rev.*, **130**, 1913–1924, [https://doi.org/10.1175/1520-0493\(2002\)130<1913:EDAWPO>2.0.CO;2](https://doi.org/10.1175/1520-0493(2002)130<1913:EDAWPO>2.0.CO;2).
<http://journals.ametsoc.org/doi/abs/10.1175/1520-0493%282002%29130%3C1913%3AEDAWPO%3E2.0.CO%3B2>.
- Yamazaki, D., S. Kanae, H. Kim, and T. Oki, 2011: A physically based description of floodplain inundation dynamics in a global river routing model. *Water Resour. Res.*, **47**, 1–21, <https://doi.org/10.1029/2010WR009726>.
- , H. Lee, D. E. Alsdorf, E. Dutra, H. Kim, S. Kanae, and T. Oki, 2012: Analysis of the water level dynamics simulated by a global river model: A case study in the Amazon River. *Water Resour. Res.*, **48**, 1–15, <https://doi.org/10.1029/2012WR011869>.
- , G. A. M. De Almeida, and P. D. Bates, 2013: Improving computational efficiency in global river models by implementing the local inertial flow equation and a vector-based river network map. *Water Resour. Res.*, **49**, 7221–7235, <https://doi.org/10.1002/wrcr.20552>.

- Yonathan Bard, 1970: Comparison of Gradient Methods for the Solution of Nonlinear Parameter Estimation Problems. *SIAM J. Numer. Anal.*, **7**, 157–186.
- Yoon, Y., M. Durand, C. J. Merry, E. A. Clark, K. M. Andreadis, and D. E. Alsdorf, 2012: Estimating river bathymetry from data assimilation of synthetic SWOT measurements. *J. Hydrol.*, **464–465**, 363–375, <https://doi.org/10.1016/j.jhydrol.2012.07.028>, <http://dx.doi.org/10.1016/j.jhydrol.2012.07.028>.
- Zhang, Y., J. Gao, and Y. Gu, 2011: A simple method for mapping bathymetry over turbid coastal waters from MODIS data: possibilities and limitations. *Int. J. Remote Sens.*, **32**, 7575–7590, <https://doi.org/10.1080/01431161.2010.524903>.